

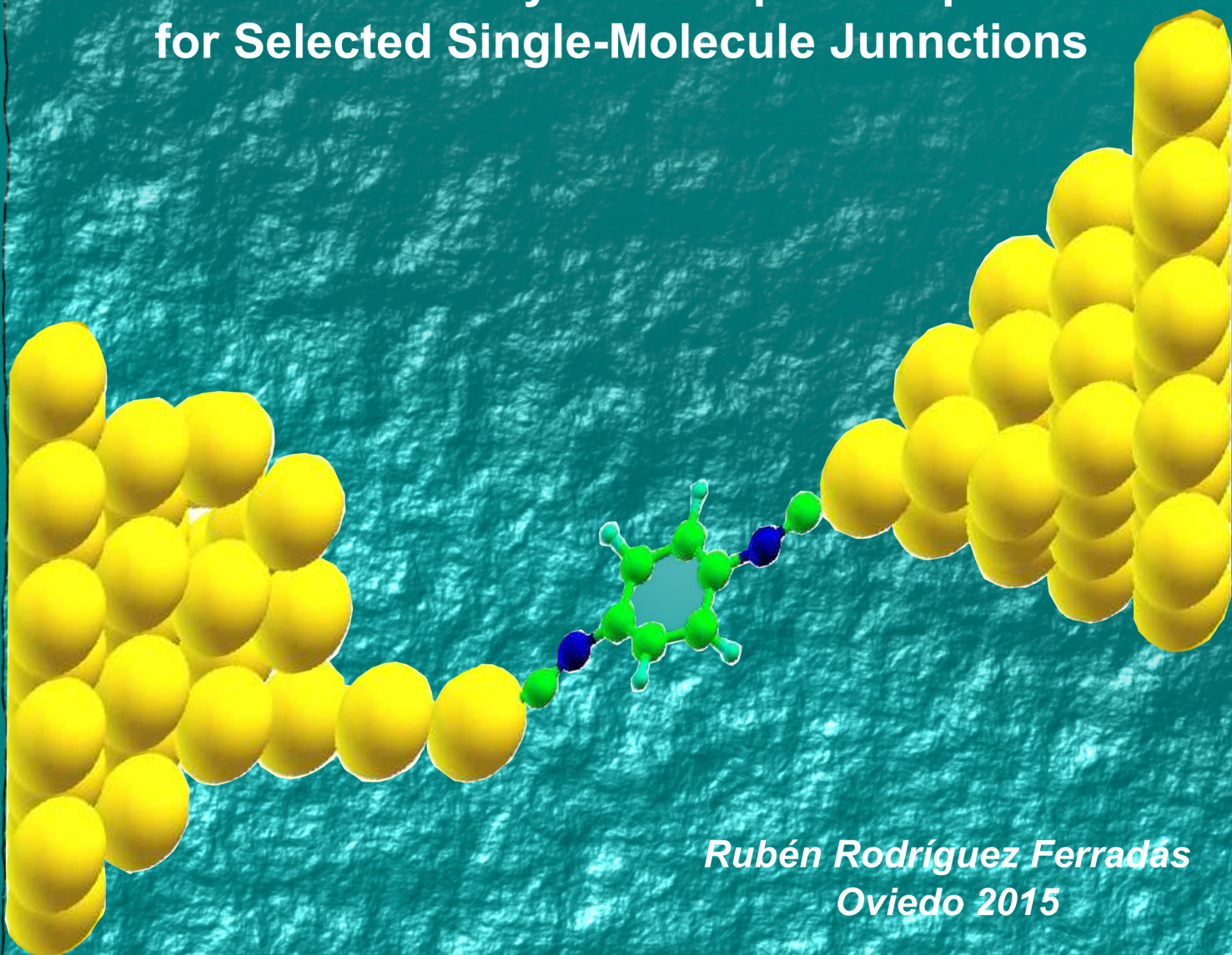


UNIVERSIDAD DE OVIEDO

Departamento de Física

Programa de doctorado: Física de la Materia Condensada

Theoretical Study of Transport Properties for Selected Single-Molecule Junctions



Rubén Rodríguez Ferradás
Oviedo 2015

Theoretical Study of Transport Properties for Selected Single-Molecule Junctions

Author

Rubén R. Ferradás

Advisor

Jaime Ferrer Rodríguez

Co-Advisor

Víctor Manuel García Suárez

For the degree of
Doctor of Philosophy

Departamento de Física
Universidad de Oviedo

Octubre 2015

Acknowledgements

Since I started my PhD until now, when all the work done along these years has culminated in this thesis, many people has helped me in lesser or greater extent in this tough task. It would be unjust not mentioning all of them.

First of all, I would like to thank strongly my thesis advisor Jaime Ferrer for his support and dedication during all these years. He initiated me in the topics presented in this thesis and gave me many insights and advice, which were the seed to develop my work. We spent many hours trying to analyze and understand our theoretical results regarding the experimental results of our collaborators. In addition, he always was willing to hear my problems and try to help to solve them. Many thanks Jaime.

My first steps into the ab-initio simulations and the introduction to the SIESTA and SMEAGOL codes were conducted by my thesis co-advisor Víctor Manuel García Suárez. He also gave me the opportunity to join to interesting projects, and I am grateful for that.

I would like to thank to the Strasbourg group the new approach to relevant problems that I was able to learn with them. Many thanks to Rodolfo Jalabert, Dietmar Weinmann and specially to Guillaume Weick, who provided me guidance and help. He introduced me an interesting problem that while is not part of this thesis, it will be a really stimulating issue to address in the future. Also, I would like to mention the appealing discussions with their students Adam Brandstetter-Kunc and Ousmane Ly, that I enjoyed largely.

I would also like to thank my office mates with whom I shared not only physics discussions, but also my problems and worries. It would have been difficult to spend these years in Oviedo without Lucas Fernández, Diego Carrascal and Ahmad Waseem. I want also to mention the people of the experimental condensed matter physics group headed by José María Alameda, Luis Álvarez and José Ignacio Martín, and his students Rosalía Cid, Aurelio Fernández, Gabriel Rodríguez, Fernando Valdés and Cristina Blanco. We spend many good times together.

I would also to extent to my gratitude to my friends and all people that I met and helped me during these years and apologize for not mentioning explicitly.

Finally, I can not forget my family and my beloved girlfriend. I would like to

thank specially to them for their priceless and constant support and comprehension. A special mention worthy my girlfriend, because is thank to her that I have been able to finish my thesis. She supported me in the worst moments and gave me encouragement when I needed it. This thesis is dedicated to you, Verónica.

Acknowledgements	ii
List of Figures	vii
1 Introduction	1
1.1 Timeline of Molecular Electronics	3
1.2 State of Art	7
1.3 Objectives and Future Challenges	12
1.4 About this work	14
2 Theoretical Background	17
2.1 Outline	17
2.2 The Many Body Problem	18
2.3 DFT Approach to Many Body Problem	21
2.3.1 Exchange and Correlation	23
2.3.2 Local Density Approximation	25
2.3.3 Generalized Gradient Approximation	25
2.3.4 Limitations of LDA and GGA	26
2.3.5 The SIESTA Method	28
2.4 Electronic Transport	33
2.4.1 Equilibrium Formalism: GOLLUM Code	39
2.4.2 Non Equilibrium Green's Function: SMEAGOL Code	42
3 Quantum Interference Effect in MetalloPorphyrins Wires	45
3.1 Introduction and Outline	45
3.2 Computational Method	47
3.3 Electronic Structure	49
3.3.1 Isolated molecules	49

3.3.2	Molecules contacted by gold	50
3.4	Transport Properties	52
3.4.1	Zero-bias	52
3.4.2	Finite-bias	58
3.5	Thermoelectric Properties of CuP	60
3.6	Remarks	62
4	Strategies for Conductance Variability Reduction	65
4.1	Problem variability in single-molecule experiments	65
4.2	Computational Method: theoretical set-up to simulate room temperature measurements and transport calculations	68
4.3	Theoretical Results	71
4.3.1	System's geometry: How the molecules are bonded to gold electrodes?	71
4.3.2	Transport Properties	75
4.4	Remarks	80
5	Single-molecule Diodes with Asymmetric Molecules	83
5.1	General Introduction	83
5.2	Simple Model	85
5.3	Searching for enhancing rectification ratios in single-molecule junctions	92
5.3.1	Computational Details and System geometry	93
5.3.2	Theoretical Results	98
5.4	Remarks	114
6	Exploring New Materials as Electrodes in Molecular Electronics	115
6.1	Introduction: Graphene as a possible electrode	115
6.2	System Under Study and Theoretical Method	117
6.3	Main Transport Results	120
6.4	Remarks	124
7	Final Remarks	127
	Bibliography	129

List of Figures

1.1	IV characteristics for HOPG surface with (bottom panel) and without copper-phthalocyanine reproduced from reference [12]	4
1.2	Negative differential resistance in Au/thiolate/Ti, (a) Schematic view of the measurement process and (b) I(V) characteristics reproduced from reference [14].	6
1.3	molecular switch, (a) Schematic view of the system and (b) I(V) characteristics showing On/Off states, reproduced from reference [17].	7
1.4	(a) schematic view of a molecule covalently bonded to Au electrodes under mechanical stretching; (b-d) conductance versus stretching and force versus stretching; it can be seen, from the inset in (d), that the force fluctuations are correlated with conductance fluctuations; reproduced from reference [32] . . .	8
1.5	(a) waterfall plot of Raman spectrum and positively correlated differential conductance measurements for a p-mercaptoaniline (left) and fluorinated oligophenylene ethynylene (right) reproduced from reference [38]; (b) schematic diagram of fishing-mode in Tip-enhanced Raman spectroscopy using 4bipy, (c) intensity versus Raman shift for different bias voltage (Inset: current versus bias curve obtained with a mechanical break-junction setup) and (d) diagram illustrating why $1,609\text{ cm}^{-1}$ band splitting is proportional to the applied bias voltage; reproduced from reference [40]	9

1.6	(a) typical dI/dV spectra taken on parallel and antiparallel oriented cobalt island and energy dependence of the optimistic TMR ratio calculated from dI/dV spectra, reproduced from reference [50]; (b) three-dimensional extrapolation of a scanning-electron microscope image showing the most favourable structure of the single-molecule-based transistor and (c) dI/dV measurements for a given working point ($V_g = -0.9$ V, $V_{ds} = 0$ V) as function of the magnetic field, reproduced from reference [52]; in (c), the arrows indicate the field-sweep direction, and abrupt jumps in the differential conductance are attributed to the switching of the Tb^{3+} magnetic moment, visible for all traces of B , showing a clear hysteresis in the dI/dV characteristics.	12
1.7	(a) The local π transmission contributions through a <i>meta</i> -substituted phenyl ring at a selection of energies (top) and a plot of the π transmission (dashed line) and total transmission (solid line) across a large energy range (bottom) reproduced from reference [53]. (b) Calculated transmission of <i>para</i> - and <i>meta</i> -OPV3 derivatives in gas phase (top); amplitude and phase of the transmission through the HOMO and LUMO of a <i>para</i> -OPV3 molecule (left bottom panel) and of a <i>meta</i> -OPV3 molecule (right bottom panel), reproduced from reference [58]	13
2.1	Basic setup of the Landauer approach to transport. The leads act as reservoirs and are assumed to be in thermal equilibrium. Image from [94].	35
2.2	Completer.	37
3.1	Schematic view of a Fe-porphyrin molecule between gold leads. Yellow, dark yellow, gray, black, blue and magenta represent gold, sulphur, hydrogen, carbon, nitrogen and iron, respectively	46
3.2	PDOS projected on $-d_{xy}$ (a), d_{yz} (b), d_{z^2} (c), d_{xz} (d) and $d_{x^2-y^2}$ (e) – for an isolated FeP molecule, computed with spin-polarized GGA. The left (1) and right (2) columns correspond to calculations without U and with $U = 4.5$ eV, respectively. Positive and negative values represent spin up and spin down electrons.	51
3.3	Spatial distribution of the density of states projected on d_{yz} (a) and d_{xz} (b) orbitals of the metallic atom computed with GGA. The first case has a clear π character, whereas second case has a more pronounced σ character.	51
3.4	PDOS projected on the Fe d states (a) d_{xy} , (b) d_{yz} , (c) d_{z^2} , (d) d_{xz} and (e) $d_{x^2-y^2}$ of a contacted FeP molecule, computed with spin-polarized GGA. Positive and negative values represent spin up and spin down electrons.	52

3.5	Transmission coefficients of a FeP (a) and a CoP (b) contacted by gold electrodes, computed with spin-polarized GGA. Left (1) and right (2) columns correspond to calculations with $U = 0$ eV and $U = 4.5$ eV. Continuous and dashed lines represent spin up and spin down electrons.	53
3.6	Transmission coefficients of a (a) FeP, (b) CoP, (c) NiP, (d) CuP and (e) ZnP molecules contacted by gold electrodes, computed with spin-polarized GGA and $U = 4.5$ eV. Continuous and dashed lines represent spin up and spin down electrons. The red ellipse circles a sharp Breit-Wigner resonance. The blue ellipse signals a Fano resonance. The green ellipse indicates a masked Fano resonance.	54
3.7	Schematic representation of the simple model. Case (a) corresponds to the d level coupled to the σ state and case (b) to the d level coupled to one of the π levels.	56
3.8	(a) Transmission coefficients calculated for model (a) described in the text and schematically shown in Fig. 3.7 (a). The black solid line corresponds to the full model, whereas the red dashed corresponds to a simplified model where the HOMO (S) and π orbitals have been dropped from the calculation. (b) Transmission coefficients calculated for model (b) described in the text and schematically shown in Fig. 3.7(b). The black solid line corresponds to the full model, whereas the red dashed corresponds to a simplified model where the d and π levels have been dropped from the calculation.	57
3.9	Spin-down transmission coefficients around the Fermi level for CuP (GGA+ U) under different bias voltages and a gate voltage of 0 V (a) and 3 V (b).	59
3.10	Total current (a) and its derivative (b) for ZnP and CuP porphyrins. A gate voltage of 3 V in the central part of the junction is also included in the CuP case.	60
3.11	Thermoelectric coefficients for Cu metalloporphyrins dithiolate between gold electrodes, calculated with GGA and $U = 0$ eV (1) and $U = 4.5$ eV (2). From top to bottom, conductance G (a), Seebeck coefficient S (b), thermal conductance κ and figure of merit ZT	61
3.12	Spin-polarized transmission as a function of energy (a) and Seebeck coefficient (b) and figure of merit (c) as a function of temperature for Cu metalloporphyrins dithiolate between gold electrodes, calculated with GGA, $U = 4.5$ eV and different gate potentials.	62
3.13	Spin-polarized transmission as a function of energy (a) and Seebeck coefficient (b) and figure of merit (c) as a function of temperature for stretched Cu metalloporphyrins dithiolate between gold electrodes (the contact distance between the molecule and the electrodes was increased 0.8 Å on each side from the equilibrium configuration), calculated with GGA, $U = 4.5$ eV and different gate potentials.	63

4.1	Compounds features in this work: the backbone is 1,4-bis(phenylethynyl)benzene, and the terminating groups can be amine (-NH ₂), trimethylsilylethynyl (-C≡CSiMe ₃), triisopropylsilylethynyl (-C≡CSiMePr ₃ ⁱ) or <i>tert</i> -butylethynyl (-C≡CCMe ₃) . . .	67
4.2	the four configurations (Conf) used to start the ab-initio molecular dynamics simulations of each junction for compounds 1 , 2 and 3 (left, middle and right columns, respectively). Blue, green, dark blue, magenta and yellow represents hydrogen, carbon, nitrogen, silicon and gold respectively.	69
4.3	transmission coefficients for a MD step in configuration 2 and TMSE system (Conf2 and right column in figure 4.1) calculated using SZP+DiffuseOrbitals (black line) and DZP (red line) as a basis for gold. Note that at Fermi level, the transmission is very similar	71
4.4	Transmission coefficients for molecules with both anchor groups being (a) -NH ₂ and (b) -C≡CSiMe ₃ , calculated between flat gold surfaces, in bridge (black curve), hollow (red curve) and top (blue curve) configurations at equilibrium distance	72
4.5	A top view of the relative -C≡CSiMe ₃ group-pyramid arrangements. Blue, green, magenta and yellow atoms represent hydrogen, carbon, silicon and gold atoms, respectively. In order to make easier the visualization, only the gold atoms of the pyramid are shown and not the underlying gold terrace	75
4.6	Conductance histograms of (a) compound 1 , (b) compound 2 and (c) compound 3 . Vertical dashed lines correspond to the experimental values (e.g. three conductance groups for 1 , two conductance groups for 2 and one conductance group for 3	77
4.7	Experimental conductance histograms for the three compounds, reproduced from [140]	78
4.8	Transmission as a function of energy for a junction comprising (a) compound 1 , (b) compound 2 and (c) compound 3 on a gold surface with pyramids . . .	79
4.9	Transmission as a function of energy for a junction comprising 3 and 4 (solid black and magenta dashed lines, respectively) on a flat gold surface (without pyramids), calculated at the equilibrium distances (4.0 Å and 5.0 Å from the Si atom to the surface for 3 and 4 respectively).	81
5.1	Schematic structure of an asymmetric tunneling barrier molecular rectifier. . .	86
5.2	the basic principle of rectification by asymmetric tunneling barriers. In (a) ϵ_0 is the energy difference between the LUMO and the Fermi Level. In (b) a negative bias is applied; the current rises when the molecular state aligns with the right Fermi level at V_R . In (c), positive bias is applied, and the current rises when the molecular state aligns with left Fermi level at V_F	86

5.3	schematic view of the gold-sodium system. Yellow and blue represent gold and sodium respectively.	89
5.4	(a) I-V characteristics for the gold-sodium system, which shows an asymmetric behaviour. In the Y-axis, is represented the absolute of the current in amperes, and in the X-axis the bias voltage in volts and (b) RR for the system	89
5.5	projected density of states onto sodium atom (PDOS) -top panel- and transmission coefficients -bottom -panel- for (a) -1.40 and -0.35 volts and (b) 0.35 and 1.40 volts. PDOS and transmission coefficients at zero voltage are shown in both. The zero of the energy is the Fermi level. Broken vertical lines represent the bias window when the voltage is changing.	90
5.6	Energy of the sodium state (LUMO) versus bias voltage. Stars represent the energy extracted from the calculation and blue straight line its linear regresion. Red and dark straight lines represent left and right chemical potentials respectively. Green arrow points out the voltage value where the state enters in the bias window.	91
5.7	The voltage drop for an applied bias of -1.40 V, calculated in a plane going along the chain.	91
5.8	IV characteristics for the <i>Ab-Initio</i> calculation (black solid curve) and for the model of resonant tunneling (red dashed curve).	92
5.9	Schematic structure of the (2,6) member of the MR family.	93
5.10	Molecules under study: MR(2,5) with (a) asymmetric and (b) symmetric anchoring groups. Molecules are shown as they would be in the contact configuration, namely, without final hydrogen atoms. Blue, green, dark blue and yellow represent hydrogen, carbon, nitrogen and sulphur respectively.	94
5.11	Initial positions after geometry optimization for MR(2,5) with (a) asymmetric or (b) symmetric anchoring groups. Blue, green, dark blue, yellow and dark yellow represent hydrogen, carbon, nitrogen, sulphur and gold respectively.	95
5.12	Final positions in the OC for MR(2,5) with (a) asymmetric or (b) symmetric anchoring groups. Blue, green, dark blue, yellow and dark yellow represent hydrogen, carbon, nitrogen, sulphur and gold respectively. It is worth mentioning that the distance in (a) between the sulphur in thiol and the gold surface is 4.8 Å.	96
5.13	(a) Energy versus position in the system with MR(2,5)-symmetric at the end of OC. The zero is the position shown in figure 5.12(b) and (b) position after coordinates relaxation adopted for the calculations. The distance between left sulphur and gold surface is 5.3 Å	97

-
- 5.14 projected density of states onto sulphur in thiol (S_R), both sulphurs in di-thiol (S_L) and carbon atoms in benzene ring ($C_{Benzene}$) and transmission coefficients for a geometry in (a) and (b), and for b geometry (c) and (d); panels represent PDOS and $T(E)$ for -1.2 V (blue) -0.6 (red) and 0.0 V (black); right panels represent 0.0 V (black), 0.6 V (red) and 1.2 V (blue). The zero of the energy is the Fermi level at zero voltage. Broken vertical lines represent the bias window when the voltage is -1.2 or 1.2 volts (blue), -0.6 or 0.6 (red) and at zero voltage (black). 102
- 5.15 (a) evolution of the molecular states energy as a function of applied bias voltage for (a) a geometry. Solid red and black lines represent the electrode chemical potentials, which are symmetrically shifted by the applied voltage $\mu_{R(L)} = E_F - (+)qV/2$. (b) an estimation of Γ_1 and Γ_2 calculated with Breit-Wigner model. The colour code represents: highest energy benzene state in green (named C_{Ben} Right Peak) and lowest energy benzene state in blue (named C_{Ben} Left Peak). (c) local density of states calculated in small range around -0.5 eV at zero voltage. (d) 2D plot of the voltage calculated along the molecule for -1.2 V. Solid contour are separated by 0.1 V. 103
- 5.16 (a) evolution of the molecular states energy as a function of applied bias voltage for (a) b geometry. Solid red and black lines represent the electrode chemical potentials, which are symmetrically shifted by the applied voltage $\mu_{R(L)} = E_F - (+)qV/2$. (b) an estimation of Γ_1 and Γ_2 calculated with Breit-Wigner model. The colour code represents: highest energy benzene state in green (named C_{Ben} Right Peak), middle energy benzene state in violet (named C_{Ben} Mid Peak) and lowest energy benzene state in blue (named C_{Ben} Left Peak). (c) local density of states calculated in small range around -0.25 eV at zero voltage. (d) 2D plot of the voltage calculated along the molecule for -1.2 V. Solid contour are separated by 0.1 V. 105

-
- 5.17 projected density of states onto sulphur in thiol (S_R), both sulphurs in di-thiol (S_L) and carbon atoms in benzene ring ($C_{Benzene}$) and transmission coefficients for c geometry; panels represent PDOS and T(E) for (a) -1.2 V (blue) -0.6 (red) and 0.0 V (black) and (b) 0.0 V (black), 0.6 V (red) and 1.2 V (blue). The zero of the energy is the Fermi level at zero voltage. Broken vertical lines represent the bias window when the voltage is -1.2 or 1.2 volts (blue), -0.6 or 0.6 (red) and at zero voltage (black). (c) local density of states calculated in small range around -0.18 eV at zero voltage. (d) evolution of the molecular states energy as a function of applied bias voltage. Solid red and black lines represent the electrode chemical potentials, which are symmetrically shifted by the applied voltage $\mu_{R(L)} = E_F - (+)qV/2$. The colour code represents: highest energy benzene state in green (named C_{Ben} Right Peak), and the sulphur state in thiol in magenta (named S_R). 106
- 5.18 projected density of states onto sulphur in right (S_R) and left (S_L) thiol and in carbon atoms in benzene ring ($C_{Benzene}$) as well as the transmission coefficients for a geometry in (a) and (b), and for b geometry (c) and (d); panels represent PDOS and T(E) for -1.2 V (blue) -0.6 (red) and 0.0 V (black); right panels represent 0.0 V (black), 0.6 V (red) and 1.2 V (blue). The zero of the energy is the Fermi level at zero voltage. Broken vertical lines represent the bias window when the voltage is -1.2 or 1.2 volts (blue), -0.6 or 0.6 (red) and at zero voltage (black). 111
- 5.19 in left panels, evolution of the molecular states energy as a function of applied bias voltage for (a) a geometry and (c) b geometry. Right panels, an estimation of Γ_1 and Γ_2 calculated with Breit-Wigner model for (b) a geometry and (d) b geometry. In right panels, solid red and black lines represent the electrode chemical potentials, which are symmetrically shifted by the applied voltage $\mu_{R(L)} = E_F - (+)qV/2$. The colour code represents: highest energy benzene state in green (named C_{Ben} Right Peak) and lowest energy benzene state in blue (named C_{Ben} Left Peak). 112
- 5.20 Local density of states calculated around -0.25 eV at zero voltage for system b . 113
- 5.21 projected density of states onto sulphur in right (S_R) and left (S_L) thiol and in carbon atoms in benzene ring ($C_{Benzene}$) as well as the transmission coefficients for c geometry. Left panel represents PDOS and T(E) for -1.2 V (blue) -0.6 (red) and 0.0 V (black); right panel represents 0.0 V (black), 0.6 V (red) and 1.2 V (blue). The zero of the energy is the Fermi level at zero voltage. Broken vertical lines represent the bias window when the voltage is -1.2 or 1.2 volts (blue), -0.6 or 0.6 (red) and at zero voltage (black). 113
-

6.1	Plot of the single-molecule junction studied. Red, black, green, light-blue and blue represent carbon and hydrogen in graphene, and carbon, hydrogen and nitrogen in the molecule respectively.	117
6.2	Energy analysis of the junction as a function of (a) the gap length d and (b) as a function of the lateral displacement d_y for several d (in the chart). In the last figure, the energy curves have been displaced in energy to fit them in the same figure.	119
6.3	Evolution of the Γ -point transmission coefficient $T(E)$ with increasing gap length d , which varies between -11.8 \AA and 10.2 \AA relative to d_0 , in steps of 1.0 \AA . Panels (a)-(d) correspond to curves in the intervals $[-11.8 \text{ \AA}, -6.8 \text{ \AA}]$, $[-5.8 \text{ \AA}, -0.8 \text{ \AA}]$, $[0.2 \text{ \AA}, 5.2 \text{ \AA}]$ and $[6.2 \text{ \AA}, 10.2 \text{ \AA}]$, respectively. The colours of the lines in the order <i>black, red, green, blue, yellow, brown</i> correspond to increasing d	121
6.4	Low-voltage conductance G/G_0 as a function of changes in the junction. (a) G/G_0 as a function of the gap length d ; (b) G/G_0 as a function of the transverse coordinate d_y . G/G_0 is estimated as $T(E_F)$, using only the Γ -point in the k summation.	122
6.5	Plot of the test junction (a) where red, black, green, light-blue and blue represent carbon and hydrogen in graphene, and carbon, hydrogen and nitrogen in the molecule respectively; (b) Evolution of the Γ -point transmission coefficient $T(E)$ when the top graphene sheet is moved across z-direction in steps of 0.2 \AA and (c) Low-voltage conductance G/G_0 as a function of changes parallel coordinate d_z of the top graphene sheet.	124
6.6	$T(E)$ for 1, 4 and 8 k -points for (a) $d = -10.8 \text{ \AA}$ and (b) $d = 7.2 \text{ \AA}$	125

Introduction

In last two decades, molecular electronics has experienced an enormous development driven by the improvement of theoretical and experimental techniques. For example, single-molecule experiments are now more robust and reproducible, and theoretical methods based on Green's functions theory, which have greatly enhanced, are a really good tool to investigate fundamental properties of single molecules out of equilibrium. Behind this progress, we can find two main motivations: on the one hand, an aspect purely concerning to basic science and on the other hand, an aspect worried about the possible technological applications.

Molecular junctions have proved to be ideal systems for investigating and put some light into fundamental issues like charge transport, spin transfer, thermal transport, etc., and this is the reason why a lot of research groups around the world (not only in physics field, but also in chemistry or biology) have put their focus on this area. When we are investigating these systems, we are dealing with the smallest scale possible (a few atoms sometimes) where quantum effects dominate. This opens a fascinating world almost unexplored.

In contrast, the other main motivation pushing this multidisciplinary field, is technological. Nowadays, the scientific community has realized that to think in molecules as candidates for completely substitute the silicon technology is, probably, not feasible in the short run, and a really difficult task even in the long run. Nevertheless, the efforts can be led towards a hybrid technology, where

the molecules play an important role in these hybrid structures like molecule-semiconductor or metal-molecule devices. In this sense, we could benefit from the many advantages that, the molecules have. It could be mentioned, for instance:

- **Size** → The smallest molecules which can be used range from 1 to 10 nm. This might lead to a huge packing density, much larger than packing density currently used in electronic industry.
- **Self-assembly** → One could make the most of intermolecular interactions to form bottom-up structures by self-assembly.
- **Stereochemistry** → A great deal of molecules have several stable geometries (called isomers), which usually have different optical or electronic properties.
- **Large Variability in Molecular Design** → In last decades, synthetic chemistry has reached an increasingly knowledge in designing molecules allowing to build an almost endless assortment of them.
- **Numerous degrees of freedom** → the numerous degrees of freedom inherent in molecular structure could be exploited to give rise new functionalities.
- **Lower cost in fabrication** → making molecules is much cheaper than make crystalline semiconductors.

Despite it has said up to now, today molecular electronics has a series of problems which have to be overcome for going from nanoscience to nanotechnology, even if we are thinking in hybrid structures. Mainly, the trouble comes from the large variability observed in single-molecule junctions, related with device stability. It is mandatory reduce this variability for making molecules suitable in technological applications. In this sense, maybe the first candidates for real-life applications of molecular electronics in near future are devices based on molecular monolayers using Langmuir-Blodgett films or SAM's (*Self Assembled Monolayers*) but still in this case we are far away to molecular nanotechnology for a series of problems: controlled deposition of the second electrode is a tough task, penetration of the metal through the molecular layer could yield metal filaments and short circuits and in a densely packed monolayer there will be problems related with interactions between molecules.

To sum up, molecular electronics has had a long way so far, and most likely, it is going to have a long way until it become a regular nanotechnology, but meanwhile, a lot of unexpected physics will be known, faced and understood.

Many achievements have been obtained, and many challenges have been overcome in the past, but there are still many others to overtake and It is a really exciting journey for a physicist.

1.1 Timeline of Molecular Electronics

An overview of the timeline in molecular electronics will be presented in this section. Doing a timeline of a scientific area or even about whatever knowledge area, is somehow an arbitrary task, because most of times birth of it is diffuse and it is not clear when appeared the very first idea about the issue. This is also the case for molecular electronics. Usually, most of people correlated the birth of molecular electronics with the appearance of the paper "*Molecular Rectifiers*" by Ari Aviram and Mark Ratner in 1974 [1], but admittedly, some important work about the charge transfer in molecules, both theoretical and experimental, had already been done in 1940's by, amongst others, R. Mulliken [2,3], A. Szent-Gyorgyi [4] or D. Eley [5]. Albeit in some cases the molecules were seen as semiconductors -as for example "*Phthalocyanines as Semiconductors*" in [5]-, who pointed out the possibility of incorporating them in real circuits, was Arthur Von Hippel. In 1956, while he was working at the MIT, laid the foundation of a bottom-up approach that he called *molecular engineering*. Their ideas were developed in a book published in 1959 [6]. This was the first time that the concepts *molecules* and *engineering* were related. It is worth mentioning as well the conference given by Richard Feynman in 1959 entitled "*There's plenty of room at the bottom*". In this lecture, Feynman talk about concepts astonishing like the possibility of direct manipulation of individual atoms or to make nanoscale machines using molecules. In a strict sense it was not a scientific lecture, but the ideas shown in the conference inspired many scientists to explore molecular electronics.

Along 1960's different groups started focusing their work in investigating experimentally the electron transport through molecular monolayers. But at this point, we must come back to the A. Aviram and M. Ratner work (mentioned before [1]), because is in this article where appears for first time a proposal for using a single-molecule as an electronic component. In that case, the molecule was proposed to operate like a rectifier. In spite of this revolutionary idea and of the many efforts done by the experimentalists, it was not until the invention of Scanning Tunneling Microscope [7] (STM) and Atomic Force Microscope [8] (AFM) in the early 1980's, both products of IBM laboratories in Zurich, that molecular electronics would receive a really important accolade. Using the STM,

single molecules could be manipulated [9] and the transport properties could be measured [10]. This opened plenty of possibilities, and ideas as the seminal one by Aviram and Ratner could be addressed experimentally. Along 1990's, experimental work done in molecular electronics increased a lot thanks above all to STM and AFM, the improvement in the fabrication of self-assembled monolayers and chemical synthesis and to another important measure technique: the Break Junction (both mechanical and electrochemical), developed at the end of 1980's [11]. So, throughout 1990's, we can find numerous appealing results in the molecular electronics framework. Some of the most exciting results reported in that decade are going to expose in next paragraphs.

One of the initial attempts to investigate the electronic properties of individual molecules was reported in 1992. In that work, M. Pomerantz, A. Aviram *et al.* [12] measured the STM current of copper-phthalocyanines onto highly oriented pyrolytic graphite (HOPG) surfaces, observing rectifier behaviour in the system. The IV characteristics which they found, can be seen in figure 1.1 . Also us-

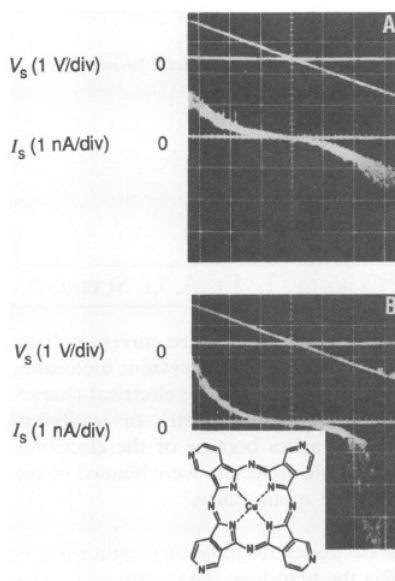


Figure 1.1: IV characteristics for HOPG surface with (bottom panel) and without copper-phthalocyanine reproduced from reference [12]

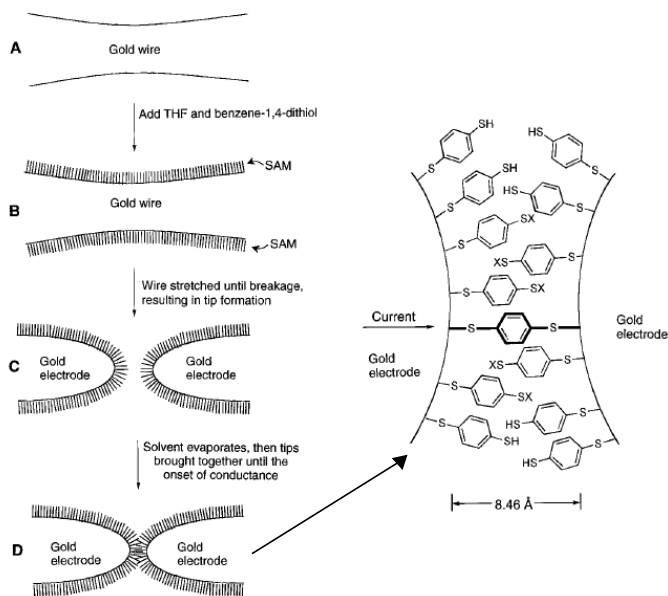
ing a STM, M. Dorogi *et al.* [13] reported Coulomb Blockade in a self-assembled nanostructure, composed by a gold cluster onto a thin alkanethiols film at room temperature. Fitting the measured current to a Coulomb Blockade model, they were able to estimate the resistance of a single molecule.

In 1997, Reed *et al.* applied for first time Mechanically Controllable Break

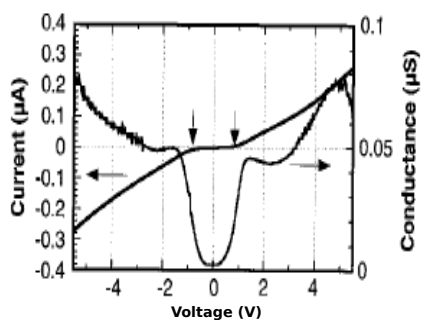
Junction technique to measure electronic transport through a single molecule, in that case *benzene-1,4-dithiol*. They measured the I(V) characteristics and observe *Negative Differential Resistance* (NDR), a typical behaviour in diodes. In Figure 1.2 a schematic view of the measurement process and the current-voltage characteristics are shown. The MCBJ technique is also applied in a work done by C. Kergueris *et al.* [15] where they demonstrated the conduction through *bisthiolterthiophene-2.5''-bis(acetylthio)-5.2'5'.2''-terthienyl*. Another significant work that it is worth noting, is the experimental realization of the ideas postulated by Aviram and Ratner in their seminal paper in 1974. R. Metzger *et al.* obtained the D- σ -A rectification across Langmuir-Blodgett (LB) multilayers and monolayers of *hexadecylquinolinium-tricyanoquinodimethanide* in 1997 [16].

As well as the electrical characterization of conducting molecules, another relevant goal was the search for individual molecules behaving as switches. The first experimental results in this issue appears in the late 1990's. So, C. P. Collier *et al.*, reported in 1999 an irreversible switch using a LB film with Rotaxanes molecules [17]. In figure 1.3 a schematic picture of the system and I(V) characteristics are shown. A little bit later in the same year, J. Chen *et al.* reported a reversible switching device using a redox SAM [18] composed by *2'-amino-4-ethynylphenyl-4'-ethynylphenyl-5'-nitro-1-benzenethiol*.

Finally, I would like to notice another important milestone in the develop of molecular electronics. This is the theoretical methods which nowadays are used, mainly leading by *Non-Equilibrium Green's function techniques* (NEGF). The original approach to mesoscopic transport, was first introduced by Rolf Landauer in 1947, and generalized by Markus Büttiker in 1980's. The so called Landauer-Büttiker method, can be applied to find the current through a *noninteracting* system or through an *effectively noninteracting* system, where *effectively noninteracting* means that the mean-field description is valid and inelastic processes can be neglected. Even though the Landauer-Büttiker formalism (LBF) has been applied successfully in several molecular electronic systems [15], usually in transport through molecular systems we are out-of-equilibrium or the strong interactions (electron-electron and electron-vibron interactions) play a fundamental role, so LBF is not sufficient to describe physics even in a qualitative level. The main approach when we want to treat with these systems is based on NEGF. In this approach, we are able to deal with a wide variety of problems related to quantum transport at the nanoscale. Proposed first time by Caroli *et al.* [19–22] in seventies, who used it for mesoscopic structures, was intensively develop in nineties [23–26]. But it has been at the beginning of 2000's with the implemen-



(a)



(b)

Figure 1.2: Negative differential resistance in Au/thiolate/Ti, (a) Schematic view of the measurement process and (b) $I(V)$ characteristics reproduced from reference [14].

tation of NEGF into many computer packages, with different approach levels, for example combined with density functional theory [27, 28] or based on effective physical models [29, 30], when techniques based on NEGF have become an essential tool for theoretical investigation in molecular electronics systems. The development of the mentioned theoretical techniques has done that agreement between the calculation and experiment, in several systems, is now surprisingly good, allowing a really nice feedback between theory and experiment in order to explore the nano-world.

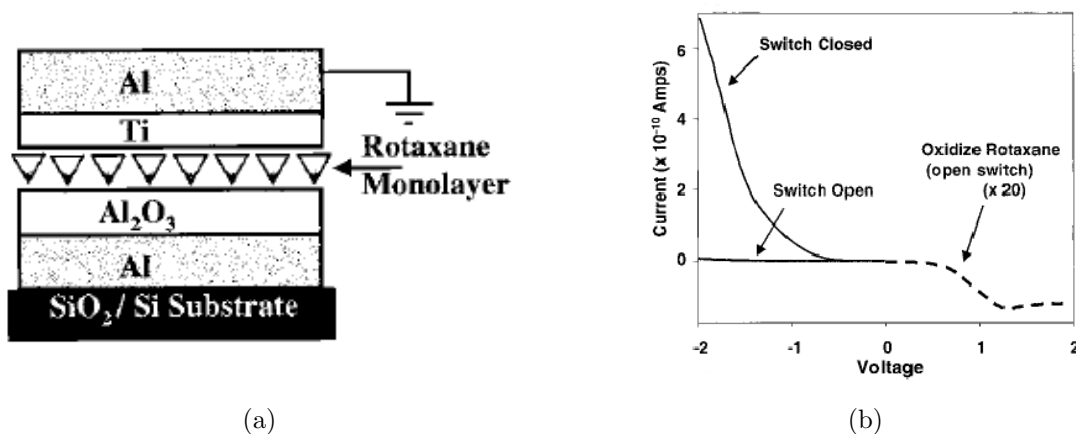


Figure 1.3: molecular switch, (a) Schematic view of the system and (b) I(V) characteristics showing On/Off states, reproduced from reference [17].

1.2 State of Art

In last decade, aside from the simplest studies on conductance, fundamental and applied aspects of optical, mechanical or thermoelectric properties at molecular scales have had an increasing relevance in the framework of molecular electronics. Other important aspects as quantum interference or spin manipulation have also been addressed. The search for new paradigms which can take advantage of quantum properties of molecules, is an area with a lot of interest, where many efforts have been done in recent years. In order to give an idea of the state-of-art in molecular electronics, an overview of the most relevant works reported in the last decade are going to be shown.

Knowing the structural information of a molecular junction when the electronic properties are measured is, in general, not possible. However, simultaneously measurements of force and electronic properties can be done, and correlate them. Already in 1996, G. Rubio *et al.*, demonstrated that force and conductance are unambiguously correlated [31]. In 2003, J. Tao *et al.*, using an AFM, reported a clear correlation between force and conductance on metal-molecule-metal junction [32] (see Figure 1.4) at room temperature. Using dynamic force microscopic techniques, unlike static mode of AFM-based force spectroscopy [33], R. Berndt *et al.* have studied the interaction between electronic transport, binding energy and structure in fullerenes [34]. Using a novel approach for AFM measures, L. Venkataraman *et al.*, have been able to probe the influence of the chemical linker group and the molecular backbone on single-molecule junction rupture force [35, 36]. Besides correlate the structure, force and electronic properties, there has been another helpful use of force measurements techniques, this is, measure the contribution of van der Waals interactions at nanoscale as was

reported by, for example, C. Wagner *et al.* [37]. So, using force measurements in the junctions at nanoscale through AFM techniques, can be a source of important information to investigate the structure and the interactions at that scale.

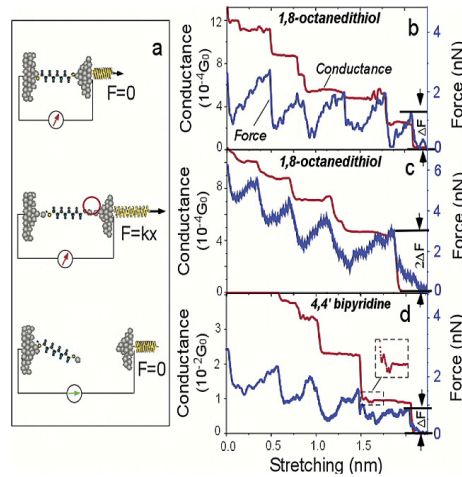


Figure 1.4: (a) schematic view of a molecule covalently bonded to Au electrodes under mechanical stretching; (b-d) conductance versus stretching and force versus stretching; it can be seen, from the inset in (d), that the force fluctuations are correlated with conductance fluctuations; reproduced from reference [32]

Putting aside the force measurements, another important area of researching, is the study of optical properties. In the study of optical properties, It can be included, the study of optical spectroscopies which could give structural information, the study of the interactions between plasmons and molecules or the use of light for controlling the transport properties in molecular systems. In this sense, It can be found a lot of really interesting results reported in recent years. The possibility of doing simultaneous measurements of optical and electrical properties, have been recently demonstrated in a series of works. The first one, was done by D. R. Ward *et al.* [38]. They irradiated molecular junctions with a few molecules, and where the junctions had been made using Au nanogaps formed by electromigration, with a laser operating at a wavelength near to the plasmon resonance and observed a Raman signal due to molecules (see Figure 1.5(a)). Then, they used the same experimental set-up to estimate vibrational and electronic heating in molecular junctions [39]. Using the STM-based break-junction technique, Z. Liu *et al.* realized conductance and Raman measurements simultaneously [40] (see figure 1.5(b)). They coupled a laser to a molecular junction formed by Au(111) surface, 4-4'-bipyridine (4bipy) and Au STM tip. They found that conducting molecular junctions had a Raman signature that was distinct from the broken molecular junctions. In addition, they also found a reversible splitting in the

Raman signature, when changing the voltages ranging from 10 to 800 mV (see figure 1.5(c) and 1.5(d)). As well as these conductance/Raman experiments for addressing the structure and vibrational properties, light can be used for controlling the transport through molecules. So, molecules with two or more stable and optically accessible states can be used. Usual molecules are for example, azobenzene derivatives, which have *cis* or *trans* form with different conductance [41]. Battacharyy *et al.* have proved that porphyrin-C₆₀ could be another candidate. In this case, the light induce an excited-state with a different conductance [42]. It has been shown that the study of optical properties, can be a source of basic physical information and the launch ramp for future molecular-device applications.

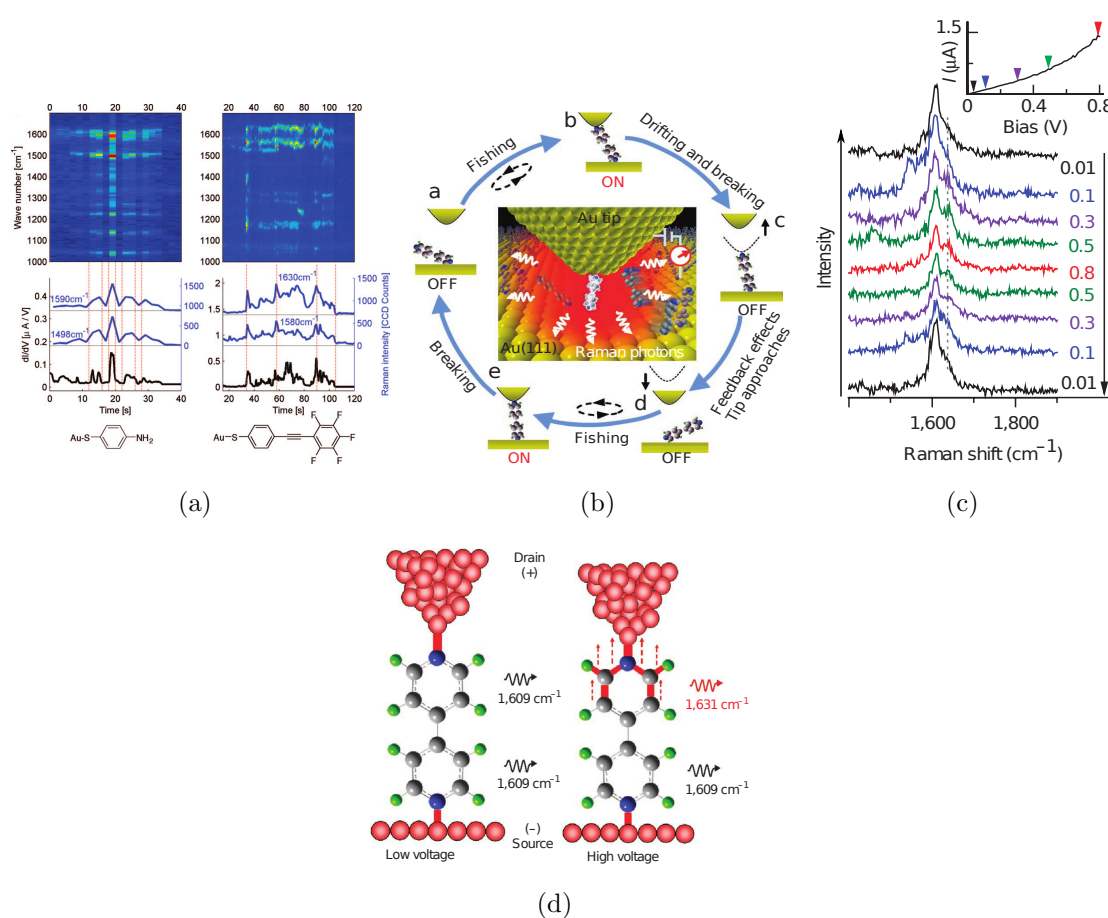


Figure 1.5: (a) waterfall plot of Raman spectrum and positively correlated differential conductance measurements for a p-mercaptoaniline (left) and fluorinated oligophenylene ethynylene (right) reproduced from reference [38]; (b) schematic diagram of fishing-mode in Tip-enhanced Raman spectroscopy using 4bipy, (c) intensity versus Raman shift for different bias voltage (Inset: current versus bias curve obtained with a mechanical break-junction setup) and (d) diagram illustrating why $1,609\text{ cm}^{-1}$ band splitting is proportional to the applied bias voltage; reproduced from reference [40]

Even though thermoelectric properties of materials have been broadly studied in the past, the focus on the electronic response to heating in molecular systems is relatively recent [43]. It has not only a basic scientific interest but also possible applications in the future of molecular electronic devices. The basics ingredients in the thermoelectric characterization are the Thermopower or Seebeck coefficient and the electric and thermal conductivity. So, the efficiency in a thermoelectric system is then given by the Figure of Merit defined as $Z = \frac{\sigma \cdot S}{\kappa}$ where σ is the electric conductivity, S is the Seebeck coefficient and κ is thermal conductivity. In particular the Seebeck coefficient, which is defined as $S = -(\frac{\Delta V}{\Delta T})|_{I=0}$, establish the magnitude of an induced voltage in response to a temperature difference across the junction. In addition, measurement of S can tell us about the nature of the charges in a junction [44]. So, when S has a positive sign the transport is through holes, and when S has a negative sign, is through electrons. The first experimental measurement of S and conductance was reported in 1999 by B. Ludoph and J. M. van Ruitenbeek [45]. The system was formed by Au point contacts at liquid helium temperatures. Using basically the same method, but implemented in STM geometry, P. Reddy *et al.* was able to measure S in a molecular junction for first time [46]. They could only measure S and not the conductance, but they could determine the nature of the transport in the molecule used, namely, thiol-terminated oligophenyls with 1-3-benzene units. They showed that the transport occurred through holes. Since then, a series of experiments have been done to measure S , showing both hole and electron transport. So far, the magnitudes measured in the experiments have been small, but is a future task try to become bigger this magnitude. So, again, the measure of S is a source of fundamental transport information.

One of the fields most promising in the molecular electronics framework is perhaps the Spintronics. This is a really novel field, but with impressive results. Although the earliest experiments were already done in 2002, exploring the spin-dependent transport and Kondo effect in single molecule devices [47,48], nowadays the focus is put in controlling the spin state of a molecule or the electrons flowing through a junction. There may be three different scenarios: non magnetic electrodes with magnetic molecule in between, magnetic electrodes with non-magnetic molecule in between, or both electrodes and molecule magnetic. In a recent experiment, H. van der Zant **et al.** were able to electrically control the spin state of a single molecule, in that case, Mn-terpyridine derivative [49]. They could change between a high-spin ($S = 5/2$) and a low-spin ($S = 1/2$) configuration. For doing this, they used a gate electrode to change the charge state of the ligands, and so, change the spin state in Mn atom. In the latter case, all the elements were

magnetic (electrodes and molecule), but there is another type of experiment, as It has already mentioned, where the only magnetic elements are the electrodes. In a experiment of that type, W. Wulfhekel and co-workers reported a different conductance depending on the relative alignment (parallel or antiparallel) of the electrodes magnetization [50]. The system was formed by a phthalocyanine molecule on a Co island onto a Cu(111) substrate, and the conductance was measured with STM-tip made by Co-coated tungsten (see Figure 1.6(a)). The conductance was found around 60% higher when the magnetization of the electrodes was parallel. In the same type of experiment, J. P. Bucher and co-workers showed that Co-phthalocyanine on Co surface could act as a scatterer or spin filter, depending on the bias voltage applied [51]. Often, the electronic spins of the molecule are strongly coupled to the electrodes, and It becomes these spintronic systems inappropriate for possibles uses. Nevertheless, nuclear spins are weakly coupled and isolated, but It makes them highly difficult to manipulate. Notwithstanding, It have been recently reported a new approach for reading out the nuclear spin of a terbium atom in a bis(phthalocyaninato)terbiumIII [52]. In the figure 1.6(b) and 1.6(c), It is illustrated the most favourable configuration of the system, and the conductance characteristics and electronic read-out procedure. All these work, besides expanding our understanding of magnetic properties in molecules, could be a start point for implementing single-molecule memory or logic circuits.

Finally, it is worth mentioning one of the hottest topics nowadays: *Quantum Interference* (QI) in molecular junctions. The QI is a direct consequence of the wave-like nature of the electrons, which is shown in transport measurements where the device length scale becomes comparable to the electronic phase coherence length. It has been reported that QI effects can change appreciably the conductance of a cross-conjugated (meta-terminated) molecule compared with the linearly conjugated (para-terminated) analogue [53] (see Figure 1.7(a)). The lower conductance is due to destructive interference that becomes in an antiresonance in transmission function of the system. If it was possible tune this antiresonance, an interference molecular switch could be made with a very large on/off ratio [54,55]. Essentially, the appearance of the interference effects is given by the chemical structure of the molecule, so, a different form to change the conductance could be provoke a change in chemical structure [56,57]. In spite of multiple theoretical approaches to molecular quantum interference, probing transport through single molecule junctions that show such effects, is a tough task, due to the small low-bias conductance. However, some results begin appearing in that issue. For example, C. R. Arroyo and co-workers, reported the difference in conductance in using oligo(3)-phenylenevinylene (OPV3) derivatives coupled to either meta- or

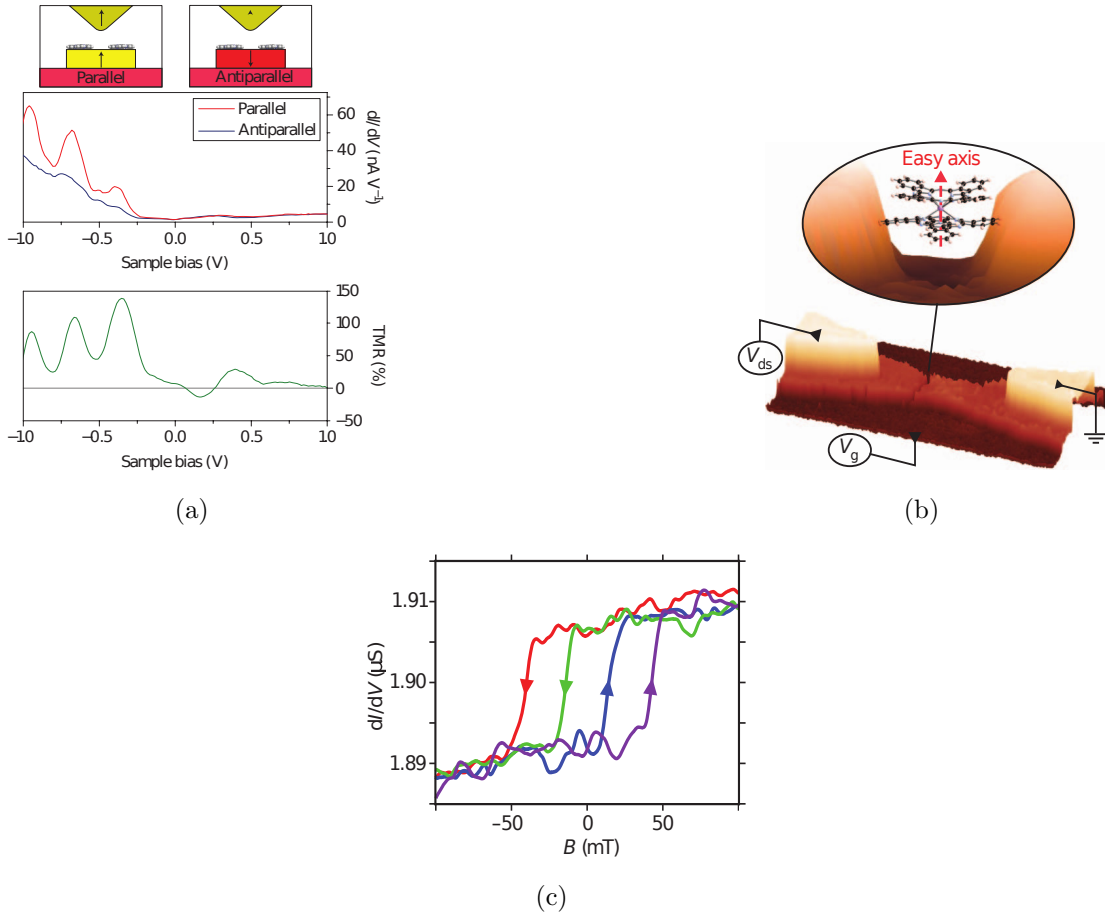


Figure 1.6: (a) typical dI/dV spectra taken on parallel and antiparallel oriented cobalt island and energy dependence of the optimistic TMR ratio calculated from dI/dV spectra, reproduced from reference [50]; (b) three-dimensional extrapolation of a scanning-electron microscope image showing the most favourable structure of the single-molecule-based transistor and (c) dI/dV measurements for a given working point ($V_g = -0.9$ V, $V_{ds} = 0$ V) as function of the magnetic field, reproduced from reference [52]; in (c), the arrows indicate the field-sweep direction, and abrupt jumps in the differential conductance are attributed to the switching of the Tb^{3+} magnetic moment, visible for all traces of B , showing a clear hysteresis in the dI/dV characteristics.

para-positions at room temperature [58] (see Figure 1.7(b)).

1.3 Objectives and Future Challenges

In the latter section, It was presented a lot of interesting and exciting results. It is clear that in last decade a tremendous progress has been made both in the experimental approaches and in theoretical methods and understanding of the molecular junctions. On the one hand, experimentally, a very significant step for reducing the variability and discrepancies in results was made with the introduction of statistical methods, as for example the systematic and repetitive



Figure 1.7: (a) The local π transmission contributions through a *meta*-substituted phenyl ring at a selection of energies (top) and a plot of the π transmission (dashed line) and total transmission (solid line) across a large energy range (bottom) reproduced from reference [53]. (b) Calculated transmission of *para*- and *meta*-OPV3 derivatives in gas phase (top); amplitude and phase of the transmission through the HOMO and LUMO of a *para*-OPV3 molecule (left bottom panel) and of a *meta*-OPV3 molecule (right bottom panel), reproduced from reference [58]

break junction method capable to produce thousand of measurements which generated a histogram of the conductivity. Furthermore, the appearance of the new techniques to measure other transport properties as thermopower or the relation force/conductance, has provide plenty of useful information not accessible by the traditional transport methods. Theoretically, the combination of NEGF and electronic structure methods (above all DFT) has become possible a reliable study of mechanical and transport properties, which results are not only in good agreement with experiments, but also are capable to predict trends and behaviours. All this stuff invite us to be optimistic in a middle-long run about the develop of this field.

However, as It was already pointed out, there are still some troubles which have to be overtaken. Albeit the statistical methods have yielded very profitable fundamental information, we need to go toward narrower experimental variations in the measurements. It has been demonstrated that the details of contact geometry and conformation are critical to the electronic behaviour of the junction. So, the search for new paradigms on how to couple molecules to electrodes should be one of the objectives. The electronic coupling between electrodes and molecules must be understood or at least controlled reproducibly. This may provide a systematic method to fabricate single molecules in a locked-in configuration which would ensure conductance stability over a long length of time.

Besides the experimental problems, we can find theoretical problems. The combination of DFT-NEGF, maybe the theoretical approach mostly used in molecular electronics, has proven to be a nice tool for addressing molecular junctions.

Nonetheless, there exists discrepancies between different DFT-based methods, and understand where is the origin of this divergences should be another objective [59].

Lastly, It should be noted another important touchstone which can help to circumvent the problems in molecular electronics: the use of graphene [60]. The use of graphene for making electrodes in molecular junctions instead of the traditional gold or platinum electrodes, could help to give stability to molecular systems. Graphene has proven to be a really good conductor mechanically very stable and It might be the future material for that purpose [61, 62]. Furthermore, graphene can also be used in self-assembled monolayers [63, 64].

1.4 About this work

Motivation and Goals

Even though the molecular electronics has evolved considerably since its birth in seventies, many fundamental issues remains elusive and in others, a deeper knowledge is mandatory in order to be able to build a profitable technology using molecules. In this sense, problems as the search for molecules with a suitable electronic properties, the study of the contacts between molecules and electrodes or the study of new materials for making electrodes, are in the heart of this thesis. So, the aim of this thesis is, from a theoretical point of view, to make a contribution in order to solve these essential molecular electronics troubles.

Outline

In Chapter 2 a review of the theoretical background will be shown. So, firstly the DFT method will be described, giving briefly an introduction and focusing in the DFT-scheme which is used throughout this thesis. Then, a review in quantum transport will be displayed. Basically, the Landauer-Büttiker formalism, as implemented in GOLLUM, will be discussed as well as the non-equilibrium Green's functions approach, as implemented in SMEAGOL. Finally, it will be presented an overview about thermoelectric properties in nano systems.

In subsequent chapters, the studies made in different molecular electronics systems will be reported. In chapter 3, the electronic structure of porphyrins-based molecules is addressed. As well, the transport and thermoelectrics properties, using gold electrodes, are studied. The porphyrins-based molecules, are conjugated molecules, which are promising candidates for several reasons as their ubiquity in nature or the fundamental role played in many nature processes as the photosyn-

thesis. In chapter 4, the problem of stability and variability in molecule junctions is addressed. In such case, the systems under study are made by gold electrodes being the molecules OPE-compounds with different ending groups (amine-amine, trimethylsilylethynyl-amine or trimethylsilylethynyl-trimethylsilylethynyl). In this case, the use of trimethylsilylethynyl- trimethylsilylethynyl endings, show a considerably reduction on the variability in conductance traces. Chapter 5 is devoted to the study of a diode-like features in molecule-gold electrodes systems. The molecules are alkyl derivatives with different anchors groups. The results show a high rectification in some cases at low voltages.

Leaving aside the study with traditional gold electrodes, chapter 6 is focused on the study of a new material for electrodes: graphene. In that chapter, the electronic properties of a series of large phthalocyanine-based molecules on graphene, are studied. The results show an universal behaviour in the transmission functions of the systems under study.

Finally, the thesis will finish in chapter 7 with the conclusions of the results obtained together with future perspectives.

Theoretical Background

2.1 Outline

The purpose of this chapter is to introduce the theoretical methods which are used throughout this thesis. The main theoretical tool, that is the base of the whole electronic structure calculations in this work, is the Density Functional Theory (DFT). So, after giving an overview about the many body problem in section 2.2, the foundations of DFT will be discussed in section 2.3. All the electronic structure calculations presented in this work were performed using the DFT code SIESTA. The main features of this code will be presented in the subsection 2.3.5.

In section 2.4, the problem of the electronic transport will be depicted. For that, first will be provided an overview about the formalism which is on the basis of the more involved transport calculations presented in the thesis: the Landauer-Bütikker formalism, as well as Green's function formalism. All the transport calculations which are presented in the thesis, have been done either with GOLLUM code or with SMEAGOL code. In consequence, the last two sections are devoted to present the main characteristics of such codes.

2.2 The Many Body Problem

At the Universe, the whole matter is made by the same basic ingredients: electrons and nuclei. Therefore, the interplay of these two fundamental type of particles provide all the objects which are present in the everyday world as atoms, molecules, condensed matter, and of course, man-made structures. Of these ingredients, electrons accomplishes two functions: on the one hand, they form the "glue" that hold together the nuclei in condensed matter; on the other hand, electron excitations play a fundamental role in the huge number of electrical, optical or magnetic properties of molecules or solids [65].

Due to the quantum nature of electrons and nuclei, their study has to be addressed in the framework of quantum mechanics. This means that they obey the Schrödinger equation. However, since the discover of such fundamental equation, It was evident that only small systems could be solved by facing with the entire system. So, It is well known that is relatively simple solve systems as for example hydrogen-like atoms, either in analytical way if the system is small or numerical if the system is bigger, but It is impossible to handle systems comprised by many particles, as molecules or solids. So, very often, some approximations must be introduced as well as using efficient numerical methods to obtain the properties of the systems under study.

In case of non-relativistic and stationary systems, one must solve and eigenvalue problem in the form:

$$\hat{H}\Psi = E\Psi \quad (2.1)$$

where the Hamiltonian \hat{H} is:

$$\begin{aligned} \hat{H} = & \sum_i^{N_e} \frac{-\hbar^2}{2m_e} \nabla_{\vec{r}_i}^2 + \sum_I^{N_N} \frac{-\hbar^2}{2M_I} \nabla_{\vec{R}_I}^2 + \\ & + \frac{1}{2} \sum_{I \neq J}^{N_N} \frac{e^2 Z_I Z_J}{|\vec{\mathbf{R}}_I - \vec{\mathbf{R}}_J|} - \frac{1}{2} \sum_{i,I}^{N_e, N_N} \frac{e^2 Z_I}{|\vec{\mathbf{r}}_i - \vec{\mathbf{R}}_I|} + \frac{1}{2} \sum_{i \neq j}^{N_e} \frac{e^2}{|\vec{\mathbf{r}}_i - \vec{\mathbf{r}}_j|} \end{aligned} \quad (2.2)$$

being $\vec{\mathbf{r}}_i$ and $\vec{\mathbf{R}}_I$ the position operator for the i -th electron and for I -th nucleus respectively. In the latest equation, first and second terms represent the kinetic energy of the electron and nuclei respectively. The remaining terms correspond to the Coulomb interaction between nuclei, between nuclei and electrons and finally, between electrons. So, it can be written down in a more compact form as:

$$\hat{H} = \hat{T}_e + \hat{T}_N + V^{NN}(\{\vec{R}\}) + V^{Ne}(\{\vec{R}\}, \{\vec{r}\}) + V^{ee}(\{\vec{r}\}) \quad (2.3)$$

When one treats with molecules or solids, N_e and N_N goes from 10^2 in the smallest molecules to 10^{26} in a bulk solid, so the wave function in equation (2.1) can be a very intractable object due to the huge number of variables even for the smallest molecule:

$$\Psi = \Psi(\vec{x}_1, \vec{x}_2, \dots, \vec{x}_i, \dots, \vec{x}_{N_e}; \vec{X}_1, \vec{X}_2, \dots, \vec{X}_i, \dots, \vec{X}_{N_N}) \quad (2.4)$$

where it has been assumed that \vec{x}_i and \vec{X}_i comprise both the position as well as the spin coordinates. The main complications to tackle the wave function, are because of two basic reasons: on the one hand, the number of parameters to approximate the wave function rises exponentially with the number of particles and the number of grid points which are necessary to store the wave function, also grows exponentially.

The first approximation which can be done, in order to try to solve this problem, is the so called *Bohr-Oppenheimer* approximation [66]. This approximation consists in the recognition of the different time scales between the electronic and nuclear motion, inasmuch as the electrons are lighter and faster than the nuclei by almost three orders of magnitude. This assumption makes possible to decouple the electronic and nuclear degrees of freedom, and so, the wave function can be written as:

$$\Psi(\{\vec{X}\}, \{\vec{x}\}) = \Psi^e(\{\vec{X}\}, \{\vec{x}\})\Psi^N(\{\vec{X}\}) \quad (2.5)$$

where $\Psi^N(\{\vec{X}\})$ is a nuclear wave function and $\Psi^e(\{\vec{X}\}, \{\vec{x}\})$ is an electronic wave function which depends parametrically on the nuclear position. With the above assumption, it can be written:

$$\begin{aligned} \hat{T}_N \Psi^e(\{\vec{X}\}, \{\vec{x}\})\Psi^N(\{\vec{X}\}) &= \sum_I^{N_N} \frac{-\hbar^2}{2M_I} [\Psi^e(\{\vec{X}\}, \{\vec{x}\})\nabla_{\vec{R}_I}^2 \Psi^N(\{\vec{X}\}) + \\ &+ \Psi^N(\{\vec{X}\})\nabla_{\vec{R}_I}^2 \Psi^e(\{\vec{X}\}, \{\vec{x}\}) + 2\nabla_{\vec{R}_I} \Psi^e(\{\vec{X}\}, \{\vec{x}\})\nabla_{\vec{R}_I} \Psi^N(\{\vec{X}\})] \end{aligned} \quad (2.6)$$

So, due to the fact that the nuclear wave function $\Psi^N(\{\vec{X}\})$ is much more localized than the electronic wave function, is expected that $\nabla_{\vec{R}_I} \Psi^N(\{\vec{X}\}) \gg$

$\nabla_{\vec{R}_I} \Psi^e(\{\vec{X}\}, \{\vec{x}\})$. Substitution of equation (2.5) with the above approximation into equation (2.3) gives, after some algebraic manipulations:

$$[\widehat{T}_e + V^{ee}(\{\vec{r}\}) + V^{Ne}(\{\vec{R}\}, \{\vec{r}\})] \Psi^e(\{\vec{X}\}, \{\vec{x}\}) = \varepsilon(\{\vec{R}\}) \Psi^e(\{\vec{X}\}, \{\vec{x}\}) \quad (2.7a)$$

$$[\widehat{T}_N + V^{NN}(\{\vec{R}\}) + \varepsilon(\{\vec{R}\})] \Psi^N(\{\vec{X}\}) = E \Psi^N(\{\vec{X}\}) \quad (2.7b)$$

Equation (2.7a) is an electronic eigenvalue equation for an electronic Hamiltonian, $H_e(\{\vec{R}\}) = \widehat{T}_e + V^{ee}(\{\vec{r}\}) + V^{Ne}(\{\vec{R}\}, \{\vec{r}\})$ which will bear to a set of eigenfunctions $\psi_n(\{\vec{X}\}, \{\vec{x}\})$ and eigenvalues $\varepsilon_n(\{\vec{R}\})$, that depend parametrically on the nuclear positions \vec{R} . The problem has been divided in two separate Schrödinger equations. Hence, for each nuclear arrangement, equation 2.7a is solved and then for each solution, equation (2.7b) can be solved. In most cases, the latest equation is solved calculating the atomic forces and relaxing the atomic coordinates using a classical equation of motion.

In spite of the Born-Oppenheimer approximation, finding the solution of equation (2.7a) is still a hard task. The more problematic term in this equation is $V^{ee}(\{\vec{r}\})$. Because of this term, the many-electron wave function cannot be written as a product of single-particle wave functions, which means that it is not possible to separate the coordinates for each electron. However, one possibility towards the solution of the equation, and since electrons are fermions, is to use an anti-symmetric product of single particle wave functions $\varphi_i(\{\vec{x}\})$:

$$\Psi^e(\{\vec{x}\}) = \frac{1}{N!} \begin{vmatrix} \varphi_1(\vec{x}_1) & \varphi_2(\vec{x}_1) & \dots & \varphi_{N_e}(\vec{x}_1) \\ \varphi_1(\vec{x}_2) & \varphi_2(\vec{x}_2) & \dots & \varphi_{N_e}(\vec{x}_2) \\ \vdots & \vdots & & \vdots \\ \varphi_1(\vec{x}_{N_e}) & \varphi_2(\vec{x}_{N_e}) & \dots & \varphi_{N_e}(\vec{x}_{N_e}) \end{vmatrix} = \frac{1}{N!} \det[\varphi_i(\vec{x}_j)] \quad (2.8)$$

The method which uses the single Slater determinant of the form shown in (2.8) as an approximation of the wave function is known as the Hartree-Fock method [67]. Usually, the basis functions $\varphi_i(\{\vec{x}\})$ are linear combinations of Gaussian-type orbitals or of one-electron wave functions. Even though this method is the basis of many quantum mechanical calculations, it removes all the electronic correlations (except exchange correlations) and hence it can be too crude in order to obtain accurate results in some systems. One way to improve the Hartree-Fock method is known as Configuration Interaction (CI) [68], where a linear combination of Slater determinants, where is included a number of orbitals describing excited states, is used to build the wave function. However, this kind of wave

functions base methods becomes prohibitively expensive when the system under study is relatively large, due to huge computational resources necessary to carry out calculations.

2.3 DFT Approach to Many Body Problem

An alternative and powerful approach to the electronic problem is given by the Density Functional Theory (DFT) [69, 70]. The foundations of DFT were laid in 1964 when P. Hohenberg and W. Kohn proved two theorems which can be stated as follows:

- **Theorem I:** *For any system of interacting particles in an external potential $V_{ext}(\vec{r})$, the potential $V_{ext}(\vec{r})$ is determined uniquely, except for a constant, by the ground state particle density $n_0(\vec{r})$. It follows that all properties of the system are completely determined given only the ground state density $n_0(\vec{r})$*
- **Theorem II:** *A universal functional for the energy $E[n]$ in terms of the density $n(\vec{r})$ can be defined, valid for any external potential $V_{ext}(\vec{r})$. For any particular $V_{ext}(\vec{r})$, the exact ground state energy of the system is the global minimum value of this functional, and the density $n(\vec{r})$ that minimizes the functional is the exact ground state density $n_0(\vec{r})$.*

In agreement with the first theorem, the density can be seen as a basic variable which determines the Hamiltonian, which in turn determines the wave function. Hence, all the ground state quantities are a functional of the density:

$$n(\vec{r}) = \sum_{\sigma} \int d\vec{r}_2 \dots d\vec{r}_{N_e} |\Psi(\vec{r}_1\sigma_1, \vec{r}_2\sigma_2, \dots, \vec{r}_{N_e}\sigma_{N_e})|^2 \quad (2.9)$$

$$n(\vec{r}) \rightarrow V_{Ext}(\vec{r}) \rightarrow \hat{H} \rightarrow \Psi = \Psi[n(\vec{r})] \rightarrow \langle \Psi | \Theta | \Psi \rangle = \langle \Theta | [n(\vec{r})] \quad (2.10)$$

The second theorem states that the energy of the system is a functional of the density, then by minimizing the total energy, with respect to variations in the density, the exact ground state energy can be found (variational principle):

$$E[n] = \min_{\Psi} \langle \Psi | \hat{H} | \Psi \rangle = \min_{n(\vec{r})} \left\{ F[n(\vec{r})] + \int n(\vec{r}) V_{Ext}(\vec{r}) d\vec{r} \right\} \quad (2.11)$$

where $F[n(\vec{r})] = \min_{\Psi \rightarrow n(\vec{r})} \langle \Psi | \hat{T} + V_{ee} | \Psi \rangle$. In principle, if the density functional is known, it will be possible to solve the variational problem for the electron density

and hence obtain all the ground state properties of the system.

Despite of the fact that Hohenberg-Kohn theorems laid that a universal functional for the energy in terms of the density can be defined for each system, they do not say anything about how to solve the system. In this sense, Kohn and Sham proposed in 1965 an approach which assumed that the ground state density of the original interacting system could be mapped onto a chosen non-interacting system, and hence it could be replaced the many body problem by an auxiliary independent particle problem [70]. In such a scheme the energy functional could be written as:

$$E_{KS}[n] = T_s[n] + \int V_{ext}(\vec{r})n(\vec{r})d\vec{r} + E_{Hartree}[n] + E_{xc}[n] \quad (2.12)$$

where $T_s[n]$ is the functional of the kinetic energy of non-interacting electrons, $E_{Hartree}[n]$ is the Hartree term which is the classical electrostatic energy of a system of charged particles (using atomic units $\hbar = m_e = e = 4\pi/\varepsilon_0 = 1$):

$$E_{Hartree}[n] = \frac{1}{2} \int \int \frac{n(\vec{r})n(\vec{r}')}{|\vec{r} - \vec{r}'|} d\vec{r}d\vec{r}' \quad (2.13)$$

and $E_{xc}[n]$ is the exchange-correlation energy term which is given by:

$$E_{xc}[n] = \int n(\vec{r})\varepsilon_{xc}(\vec{r})d\vec{r} \quad (2.14)$$

The electron-electron interaction has been divided into the Hartree term and the exchange-correlation term, which contains information about exchange and correlation and also the difference between the exact and the non-interacting kinetic energy. Furthermore, the wave function of the system can be chosen as the wave function of the non-interacting system, which is given by a single Slater determinant:

$$\Psi_{KS}(\vec{r}_1, \dots, \vec{r}_{N_e}) = \sum_i^{N_e} (-1)^i \varphi_1(\vec{r}_{i_1}) \times \dots \times \varphi_1(\vec{r}_{i_{N_e}}) \quad (2.15)$$

where φ_i are single particle orbitals. In such a way, the density is represented by:

$$n(\vec{r}) = \sum_i^{N_e} |\varphi_i(\vec{r})|^2 \quad (2.16)$$

and the non-interacting kinetic energy as:

$$T_s[n] = -\frac{1}{2} \sum_i^{N_e} \langle \varphi_i | \nabla^2 | \varphi_i \rangle \quad (2.17)$$

The ground state of the electronic system must be found by minimizing the energy functional given in 2.12 with respect to the density. Since $T_s[n]$ has been explicitly expressed as a functional of the orbitals but the remaining terms are considered functionals of the density, the chain rule can be used to derive the following variational equation:

$$\frac{\delta E_{KS}}{\delta \varphi_i^*(\vec{r})} = \frac{\delta T_s}{\delta \varphi_i^*(\vec{r})} + \left[\frac{E_{ext}}{\delta n(\vec{r})} + \frac{E_{Hartree}}{\delta n(\vec{r})} + \frac{E_{xc}}{\delta n(\vec{r})} \right] \frac{\delta n(\vec{r})}{\delta \varphi_i^*(\vec{r})} = 0 \quad (2.18)$$

subject to the orthonormalization constraints $\langle \varphi_i | \varphi_j \rangle = \delta_{ij}$. Using the expressions for the density and the non-interacting kinetic energy given in 2.16 and 2.17, and the Lagrange multiplier method to handle the constraints, it is arrived to the Kohn-Sham Schrödinger-like equations:

$$\left[-\frac{1}{2} \nabla^2 + v_{eff}(\vec{r}) \right] \varphi_i(\vec{r}) = \varepsilon_i \varphi_i(\vec{r}) \quad (2.19)$$

where

$$v_{eff}(\vec{r}) = V_{ext}(\vec{r}) + V_{Hartree}(\vec{r}) + V_{xc}(\vec{r}) \quad (2.20)$$

The equation 2.19 along with 2.16, constitute the *Kohn-Sham equations*. The problem has been reduced to a simple single-particle problem, which has to be solved *self-consistently*. It is worth to realize that so far, no approximations has been made. It means that if the functional form of the $E_{xc}[n(\vec{r})]$ were known, the Kohn-Sham equations would lead to the exact ground state density and energy for the interacting system.

Self-Consistent cycle to solve Kohn-Sham equations:

$$n_{initial} \rightarrow \hat{H} \rightarrow \Psi \rightarrow n' \rightarrow \hat{H}' \rightarrow \Psi' \rightarrow n'' \rightarrow \dots \quad (2.21)$$

2.3.1 Exchange and Correlation

It has been pointed out that all the many-body effects are taken into account in the exchange-correlation energy. But, how can be the many-body contributions separated? Insights on this issue can be achieved by the coupling-constant integration which is going to be derived [71]. Let Ψ_λ be a normalized antisymmetric wave function which yields density n and minimizes the expectation value of $\hat{T} + \lambda \hat{V}_{ee}$ where it has been introduced a non-negative coupling constant λ . If $\lambda = 1$, Ψ_λ is the interacting ground state wave function for density n . In contrast, if $\lambda = 0$, Ψ_λ is the non-interacting wave function Ψ_{KS} which was defined in 2.15. Then, using

the functional dependence of the interacting system with the coupling constant, it can be written:

$$\begin{aligned} E_{xc}[n] &= \langle \Psi_\lambda | \hat{T} + \lambda \hat{V}_{ee} | \Psi_\lambda \rangle_{\lambda=1} - \langle \Psi_\lambda | \hat{T} + \lambda \hat{V}_{ee} | \Psi_\lambda \rangle_{\lambda=0} - E_{Hartree}[n] = \\ &= \int_0^1 \frac{d}{d\lambda} \langle \Psi_\lambda | \hat{T} + \lambda \hat{V}_{ee} | \Psi_\lambda \rangle d\lambda - E_{Hartree}[n] \end{aligned} \quad (2.22)$$

Utilizing the Hellmann-Feynman theorem, this expression can be simplified and written as:

$$E_{xc}[n] = \int_0^1 \langle \Psi_\lambda | \hat{V}_{ee} | \Psi_\lambda \rangle d\lambda - E_{Hartree}[n] \quad (2.23)$$

To go further, it is necessary to know how to evaluate the N-electron expectation value of the two-body operator \hat{V}_{ee} . To do this, the two-electron reduced density matrix is introduced as:

$$\rho_2(\vec{r}', \vec{r}) = N_e(N_e - 1) \int d\vec{r}_3 \dots \int d\vec{r}_{N_e} |\Psi(\vec{r}', \vec{r}, \vec{r}_3, \dots, \vec{r}_{N_e})|^2 \quad (2.24)$$

Then, \hat{V}_{ee} can be written as:

$$\langle \hat{V}_{ee} \rangle = \frac{1}{2} \int d\vec{r} \int d\vec{r}' \frac{\rho_2(\vec{r}', \vec{r})}{|\vec{r} - \vec{r}'|} \quad (2.25)$$

The two-electron reduced density matrix tells the probability of finding an electron at \vec{r} and other at \vec{r}' simultaneously. Due to the electrons are not independent particles, this probability is the product of the probability of finding an electron at \vec{r} and the conditional probability of finding an electron at \vec{r}' given that there is one at \vec{r} :

$$\rho_2(\vec{r}', \vec{r}) = n(\vec{r})n_2(\vec{r}, \vec{r}') = n(\vec{r})[n(\vec{r}') + n_{xc}^\lambda(\vec{r}, \vec{r}')] \quad (2.26)$$

where $n_{xc}^\lambda(\vec{r}, \vec{r}')$ is the density at \vec{r}' of the exchange-correlation hole about an electron at \vec{r} , given taking into account the wave function Ψ_λ . It follows that:

$$\int n_{xc}^\lambda(\vec{r}, \vec{r}') d\vec{r}' = -1 \quad (2.27)$$

which means that, if there is an electron at \vec{r} , it is missing from the rest of the system. Now, from the equations 2.25 and 2.26, $E_{xc}[n]$ can be written down as:

$$E_{xc}[n] = \frac{1}{2} \int d\vec{r} \int d\vec{r}' \frac{n(\vec{r})\bar{n}_{xc}(\vec{r}, \vec{r}')}{|\vec{r} - \vec{r}'|} = \int n(\vec{r})\varepsilon_{xc}([n(\vec{r})], \vec{r}) d\vec{r} \quad (2.28)$$

where $\bar{n}_{xc}(\vec{r}, \vec{r}')$ is the coupling-constant average hole density and $\varepsilon_{xc}([n(\vec{r})], \vec{r})$ is the exchange-correlation energy per electron:

$$\bar{n}_{xc}(\vec{r}, \vec{r}') = \int_0^1 n_{xc}^\lambda(\vec{r}, \vec{r}') d\lambda \quad (2.29a)$$

$$\varepsilon_{xc}([n(\vec{r})], \vec{r}) = \frac{1}{2} \int d\vec{r}' \frac{\bar{n}_{xc}(\vec{r}, \vec{r}')}{|\vec{r} - \vec{r}'|} \quad (2.29b)$$

It can be said that the hole is created by three effects: (1) self-interaction correction, which tells that an electron cannot interact with itself, (2) the Pauli exclusion principle, which tends to keep two electrons with parallel spins separated, and (3) the Coulomb repulsion. Effects (1) and (2) are responsible for the exchange energy, which is present even at $\lambda = 0$, and effect (3) is responsible for the correlation energy and arises only for $\lambda \neq 0$. As it was mentioned before, the many body effects are all included in the exchange-correlation energy. Therefore, knowing the exact form of the hole, the correct ground state density and energy would be known. However, the exact density dependence is not known (except for the uniform gas) and many approximations must be used.

2.3.2 Local Density Approximation

Maybe the most popular approximation to the exchange-correlation hole is based on the uniform electron gas, where is assumed that the hole depends only on the local density at each point \vec{r}

$$E_{xc}[n] = \frac{1}{2} \int n(\vec{r}) \varepsilon_{xc}[n(\vec{r})] d\vec{r} \quad (2.30)$$

This is the basis of Local Density Approximation (LDA). It was already introduced in the original paper by Kohn and Sham [70], and it has become popular due to its simplicity and the good results that it produces [72, 73]. It works reasonably well for system where the density varies smoothly like noble metals or light elements.

2.3.3 Generalized Gradient Approximation

Since the LDA fails when the density varies brusquely, a step beyond is including the magnitude of the gradient of the density in the functional:

$$E_{xc}[n] = \frac{1}{2} \int n(\vec{r}) \varepsilon_{xc}[n(\vec{r}), |\nabla n(\vec{r})|] d\vec{r} \quad (2.31)$$

This is the so called Generalized Gradient Approximation (GGA), which denotes a variety of ways to include the gradient in the expansion. Notwithstanding, in many cases GGA produce unphysical results, as for example positive exchange

holes. Hence, in order to correct these spurious contributions, the GGA truncates the hole and forces it to integrate to -1.

There are several strategies to improve LDA and GGA. Among them, it can be found methods based on hybrid functionals [74] or the method called Jacob's Ladder [75].

2.3.4 Limitations of LDA and GGA

Throughout the years, density functional theory has had a great success in studying many different systems composed by a variety of elements, obtaining a reasonably accuracy either using LDA or GGA, depending on the system under study. But in spite of this achievements, there are a number of problems where these approximations fail. In some systems, the discrepancies between the properties obtained in experiments and in a DFT calculation are so large, that they hinder even a qualitatively analysis of the results. There has not been developed a systematic way for improving the exchange-correlation functional. Due to the construction of the LDA and GGA approximations, the most severe problems are in materials in which the electrons are heavily localized and with strong interactions among them, such as transition metal oxides and rare earth elements and compounds. A paradigmatic example could be FeO. In such case, DFT predicts a metallic behaviour, but instead of this, FeO is an insulator.

In order to try to correct this misbehaviour, several methods have been developed to extend the functional approach and incorporate the effects which are understood to be important in the description of such materials. One of the most popular approach is the so called DFT+ U which stands methods that involve both LDA- and GGA-type calculations coupled with an additional orbital dependent interaction. It was first proposed by Anisimov *et al* [76–78]. The DFT+ U method assumes that electrons can be split into two subsystems: delocalized electrons, that can be treated with traditional DFT, and localized electrons, such as 3d or 4f in transition metals or rare earth elements respectively, which must be handled using a generalized Hubbard model Hamiltonian with orbital-dependent local electron-electron interactions. The DFT+ U functional is defined then as:

$$E_{DFT+U}[n(\vec{r}), \{n^\sigma\}] = E_{DFT}[n(\vec{r})] + E_{Hub}[\{n^\sigma\}] - E_{DC}[\{n^\sigma\}] \quad (2.32)$$

where E_{DFT} is the DFT functional; $n(\vec{r})$ is the density; E_{Hub} is the on-site Coulomb correction; E_{DC} is the double counting correction, which is necessary to avoid

including twice the average electron-electron interaction that appears also in E_{DFT} and $\{n^\sigma\}$ are the atomic orbital occupations corresponding to the orbitals that need to be corrected. The generalized Hubbard Hamiltonian is written as:

$$\hat{H}_{int} = \frac{U}{2} \sum_{m,m',\sigma} \hat{n}_{m,\sigma} \hat{n}_{m',-\sigma} + \frac{U-J}{2} \sum_{m \neq m',\sigma} \hat{n}_{m,\sigma} \hat{n}_{m',\sigma} \quad (2.33)$$

Taking the atomic limit of the above Hamiltonian where the number of strongly correlated electrons $N_\sigma = \sum_m n_{m,\sigma}$ is an integer it is possible to write:

$$\begin{aligned} E_{DC} &= \langle integer N_\sigma | \hat{H}_{int} | integer N_\sigma \rangle = \\ &= \frac{U}{2} \sum_\sigma N_\sigma N_{-\sigma} + \frac{U-J}{2} \sum_\sigma N_\sigma (N_\sigma - 1) \end{aligned} \quad (2.34)$$

In contrast, for a non integer occupation number, corresponding to an ion embedded in a larger system:

$$\begin{aligned} E_{Hub} &= \langle noninteger N_\sigma | \hat{H}_{int} | noninteger N_\sigma \rangle = \\ &= \frac{U}{2} \sum_{m,m',\sigma} n_{m,\sigma} n_{m',-\sigma} + \frac{U-J}{2} \sum_{m \neq m',\sigma} n_{m,\sigma} n_{m',\sigma} \end{aligned} \quad (2.35)$$

The above two equations can be merged and, after some algebra, the DFT+ U functional can be written as:

$$E_{DFT+U} = E_{DFT} + \frac{U_{eff}}{2} \sum_{m,\sigma} n_{m,\sigma} (1 - n_{m,\sigma}) \quad (2.36)$$

where $U_{eff} = U - J$.

It has to be noted that the correction term depends on the occupation number matrix. This matrix, which is a centerpiece of the DFT+ U approach, is not well defined, because the total density charge cannot be broken down into simple atomic contributions. Since the appearance of the DFT+ U approach, there have been many different definitions of the occupation number matrix. One interesting approach, is to evaluate it by introducing projection operators in the following way [80]:

$$n_{mm'}^{(\sigma)} = \sum_j q_j^{(\sigma)} \langle \varphi_j^{(\sigma)} | \hat{P}_{mm'}^{(\sigma)} | \varphi_j^{(\sigma)} \rangle \quad (2.37)$$

where $\varphi_j^{(\sigma)}$ are the Kohn-Sham eigenvectors for the j state with spin index σ and $q_j^{(\sigma)}$ are their occupations. The choice of the projection operators $\hat{P}_{mm'}^{(\sigma)}$ is crucial, because due to the non-orthogonal basis set different projection operators give different occupation number matrices. Here, the choice which will be taken corresponds to so-called *full* representation. Hence, the selected operator is:

$$\hat{P}_{mm'}^{(\sigma)} = |\chi_m\rangle\langle\chi_{m'}| \quad (2.38)$$

where $|\chi_m\rangle$ and $\langle\chi_{m'}|$ are the atomic orbitals of the strongly correlated electrons. Introducing this projector in 2.37 it is obtained:

$$\mathbf{n}_\sigma^{full} = \mathbf{S}\mathbf{D}_\sigma\mathbf{S} \quad (2.39)$$

where \mathbf{S} is the overlap matrix and \mathbf{D}_σ is the density matrix of the system.

2.3.5 The SIESTA Method

Spanish Initiative for Electronic Simulations with Thousand of Atoms (SIESTA) is not only a DFT code, but also a method to perform electronic structure calculations and *ab-initio* molecular dynamics simulations of molecules and solids [81]. Among the characteristic of SIESTA it is noteworthy the use of norm-conserving pseudopotentials as well as a linear combination of atomic orbitals (LCAO). This allows the simulations to scale linearly with the number of atoms (order-N method). In next sub-sections, these and other important characteristics of SIESTA are going to be explained.

Norm-Conserving pseudopotentials

Most of the physical and chemical properties in molecules or solids, can be determined taking into account solely a few electrons, the outermost. As consequence, the electrons can be classified in two types: core electrons which are localized very close to the nucleus, and valence electrons which belong to the external shells and are responsible of the most properties. Core electrons can be considered almost inert and so, its electronic density is nearly the same when the atom is isolated or is part of a bigger system. Hence, valence electrons feel core electron as an effective potential, the pseudopotential. This pseudopotential reproduces the same valence states. SIESTA utilizes the so-called norm-conserving pseudopotentials, where the functions generated with the pseudopotential have to verify the following characteristics [82]:

- The all-electron eigenvalue and the eigenvalue for pseudovalence orbital has to be the same for a given atomic configuration:

$$\varepsilon_{nl}^{ae} = \varepsilon_{nl}^{ps} \quad (2.40)$$

- Pseudovalence orbitals have to match the all-electron orbital beyond the cutoff radius:

$$R_{nl}^{ae}(r > r_l^c) = R_{nl}^{ps}(r > r_l^c) \quad (2.41)$$

- Charge density inside the core region for pseudovalence orbitals must be equal to that of all-electron orbitals:

$$\int_0^{r_l^c} |R_{nl}^{ae}(r)|^2 r^2 dr = \int_0^{r_l^c} |R_{nl}^{ps}(r)|^2 r^2 dr \quad (2.42)$$

- The radial part of the pseudovalence orbitals has to be smooth and nodeless inside the core region. As a consequence, different pseudopotentials have to be generated for each set of quantum numbers (n,l) of the valence orbitals.

From the pseudoorbital, the screened pseudopotential for a given set of quantum numbers is calculated by inverting the radial Schrödinger equation:

$$V_{nl,s}^{ps}(r) = \varepsilon_{nl} - \frac{l(l+1)}{2r^2} + \frac{1}{2rR_{nl}^{ps}(r)} \frac{d^2}{dr^2} [rR_{nl}^{ps}] \quad (2.43)$$

In order to obtain the right pseudopotential, the screening of the valence electrons calculated with the pseudoorbitals must be removed:

$$V_{nl}(r) = V_{nl,s}(r) - V_H[n^{ps}(r)] - V_{xc}[n^{ps}(r)] \quad (2.44)$$

In general, all valence shells have different quantum number l but can have the same or different quantum number n , so the dependence on the principal quantum number usually is not explicitly written. Hence, the total operator is expressed in the angular momentum basis as:

$$\hat{V}(r) = \sum_{l=0}^{l_{max}} \sum_{m=-l}^l \sum_{p=1}^{P_l} |Y_{lmp}\rangle V_{lp}(r) \langle Y_{lmp}| \quad (2.45)$$

It is possible to split a local part in the above expression to give:

$$\hat{V}(r) = V_{loc}(r) + \sum_{l=0}^{l_{max}} \sum_{m=-l}^l \sum_{p=1}^{P_l} |Y_{lmp}\rangle \delta V_{lp}(r) \langle Y_{lmp}| \quad (2.46)$$

The local part $V_{loc}(r)$ is optimized for smoothness, making it equal to the potential created by a certain positive charge. Finally, the semilocal part is transformed into the fully nonlocal form proposed by Kleinman and Bylander [83]. The

pseudopotentials can also have relativistic corrections (scalar corrections and spin orbit coupling) [84,85]. In addition, in case of atoms with strong overlaps between core and valence (for example, transition metals) it must be included non-linear corrections [86].

Basis Set

The linear dependence in Order-N methods is achieved if the Hamiltonian and overlap matrices are very sparse. Such sparsity can be obtained utilizing basis sets made of localized atomic orbitals which extend not beyond to a certain cutoff radii [87]. This definition of the Hilbert space, is the base of the *linear combination of atomic orbitals* (LCAO) method. The minimal LCAO basis set (called single- ζ , single-zeta or SZ), uses only one orbital per quantum channel, which means one orbital for a given set of n , l and m quantum numbers in the valence shell. These orbitals, known as pseudo atomic orbital (PAO), are eigenfunctions of the atomic pseudo-Hamiltonian in a spherical box [87,88]. The potential is defined as the sum of the screened l -dependent pseudoatomic potential and a certain confinement potential which makes the wave function approach zero smoothly at the cutoff radius r_l^c [89]:

$$\left[-\frac{1}{2r} \frac{d^2}{dr^2} r + \frac{l(l+1)}{2r^2} + V_l(r) + V_l^c(r - r_l^c) \right] R_l(r) = (\varepsilon + \delta\varepsilon_l) R_l(r) \quad (2.47)$$

being the determination of the radii (or, alternatively, the energy shift $\delta\varepsilon_l$) variational, which means that the energy of the system has to be minimized for each of them.

In order to obtain a better description of the systems, it can be added more ζ 's to each atomic shell. The second and subsequent ζ , $R_l^{i\zeta}(r)$, are calculated using the 'split-valence' method [90,91]: they have the same norm as the previous ζ between their corresponding cutoff radii r_l^i and r_l^{i-1} ($r_l^i \geq r_l^{i-1}$) and the polynomial form inside r_l^i :

$$R_l^{i\zeta}(r) = \begin{cases} r^l(a_l - b_l r^2) & r < r_l^i \\ R_l^{(i-1)\zeta}(r) & r_l^i \leq r < r_l^{i-1} \end{cases} \quad (2.48)$$

where a_l and b_l are chosen so that the wave function and its derivative are continuous at r_l^i . Finally, instead of $R_l^{i\zeta}$ SIESTA uses $R_l^{(i-1)\zeta} - R_l^{i\zeta}$ which produces the same description of the Hilbert space but gives functions which are more localized.

In order to give more freedom to the electrons and take into account the deformation induced by the chemical bonding, SIESTA can also include orbitals of different angular momenta which are unoccupied in the isolated atom and orbitals

with higher angular momenta which are built polarizing the existing orbitals with an electric field:

$$\left[-\frac{1}{2r} \frac{d^2}{dr^2} r + \frac{(l+1)(l+2)}{2r^2} + V_l(r) - E_l \right] R_{l+1}(r) = -r R_l(r) \quad (2.49)$$

where $R_l(r)$ is the radial part of the orbital that is going to be polarized, $\phi_{lm}(\vec{r}) = R_l(r)Y_{lm}(\hat{r})$. the new polarized orbitals are then $\varphi_{(l+1)m}(\vec{r}) = C R_{l+1}(r)Y_{(l+1)m}(\hat{r})$.

SIESTA Wave Function

According to the above explanation, the wave function in SIESTA is a linear combination of atomic orbitals, which in the general case of periodic and non-collinear system, can be written as:

$$\hat{\Psi}_{n\vec{k}}(\vec{r}) = \frac{1}{\sqrt{N_u}} \sum_{\vec{R}, \mu} e^{-i\vec{k}\vec{R}_\mu} \hat{c}_{n\vec{k}\mu} \phi_{\vec{R}\mu}(\vec{r} - \vec{R}_\mu) \quad (2.50)$$

where n is the band index, \vec{k} is the k point, N_μ is the number of unit cells in the system, $\vec{R}_\mu = \vec{R} - \vec{d}_\mu$ (\vec{d}_μ is the position of the orbital $\mu = (I, n, l, m)$ localized on atom I within the unit cell and \vec{R} is the vector between unit cells) and $\hat{\Psi}$ and \hat{c} are spinors:

$$\hat{\Psi} = \begin{pmatrix} \Psi^\uparrow \\ \Psi^\downarrow \end{pmatrix} = \sum_{\sigma=\uparrow, \downarrow} \Psi^\sigma \hat{\chi}^\sigma \quad (2.51)$$

$$\hat{c} = \begin{pmatrix} c^\uparrow \\ c^\downarrow \end{pmatrix} = \sum_{\sigma=\uparrow, \downarrow} c^\sigma \hat{\chi}^\sigma \quad (2.52)$$

where

$$\hat{\chi}_\uparrow = \begin{pmatrix} 1 \\ 0 \end{pmatrix} \quad \hat{\chi}_\downarrow = \begin{pmatrix} 0 \\ 1 \end{pmatrix} \quad (2.53)$$

Hamiltonian and Schrödinger Equation

According to the Kohn-Sham formulation, the Hamiltonian can be written as :

$$\hat{H} = \hat{T} + \sum_I V_I^{loc}(|\vec{r} - \vec{R}_I|) + \sum_I \hat{V}_I^{KB} + V^H(\vec{r}) + \hat{V}^{xc}(\vec{r}) + V^{ext}(\vec{r}) \quad (2.54)$$

where $\hat{T} = -\frac{1}{2}\nabla^2$ is the kinetic energy operator, V_I^{loc} and V_I^{KB} are the local and nonlocal parts of the pseudopotential of atom I and V^H and \hat{V}^{xc} (the only terms that depend on the self-consistent density) are the Hartree and exchange-correlation potentials respectively. If the system is spin-polarized, the exchange-correlation potential is different for spin up and down, while in the general situation of non-collinear spin systems it is a 2×2 matrix. Taking into account that the potential of the neutral atom can be written as:

$$V_I^{na}(|\vec{r} - \vec{R}_I|) = V_I^{loc}(|\vec{r} - \vec{R}_I|) + e^2 \int \frac{n_I^{atom}(|\vec{r} - \vec{R}_I|)}{|\vec{r} - \vec{r}'|} d\vec{r}' \quad (2.55)$$

and defining $\delta n(\vec{r}) = n(\vec{r}) - \sum_I n_I^{atom}(|\vec{r} - \vec{R}_I|)$, the Hamiltonian can be rewritten as:

$$\hat{H} = \hat{T} + \sum_I V_I^{na}(|\vec{r} - \vec{R}_I|) + \sum_I \hat{V}_I^{KB} + \delta V^H(\vec{r}) + \hat{V}^{xc}(\vec{r}) + V^{ext}(\vec{r}) \quad (2.56)$$

With the above Hamiltonian and the wave function previously defined, the Schrödinger equation is expressed as:

$$\langle \hat{\Psi}_{n\vec{k}} | \hat{H} | \hat{\Psi}_{n\vec{k}} \rangle = \varepsilon_{n\vec{k}} \langle \hat{\Psi}_{n\vec{k}} | \hat{\Psi}_{n\vec{k}} \rangle \quad (2.57)$$

where the Hamiltonian is a 2×2 matrix if the system is non-collinear. After some algebra, the final matrix equation is then:

$$\sum_{\nu, \sigma'} \left(H_{\mu\nu}^{\sigma\sigma'} - \varepsilon_{n\vec{k}} S_{\mu\nu} \delta^{\sigma\sigma'} \right) c_{n\vec{k}\nu}^{\sigma'} = 0 \quad (2.58)$$

where all matrices are expressed in terms of the basis orbitals of the unit cell and μ runs over the atoms in the unit cell and ν over the atoms in neighbor cells.

Density Matrix and Energy

The density is calculated as the sum of the product of the eigenvectors multiplied by the occupation, and so:

$$n^{\sigma\sigma'}(\vec{r}) = \sum_{\mu, \vec{R}_\nu} \rho_{\mu\vec{R}_\nu}^{\sigma\sigma'} \phi_\mu(\vec{r} - \vec{d}_\mu) \phi_{\vec{R}_\nu}(\vec{r} - \vec{R}_\nu) \quad (2.59)$$

where

$$\rho_{\mu\vec{R}_\nu}^{\sigma\sigma'} = \frac{1}{N_k} \sum_{n, \vec{k}} f_{n\vec{k}} e^{i\vec{k}(\vec{d}_\mu - \vec{R}_\nu)} c_{n\vec{k}\mu}^\sigma c_{n\vec{k}\nu}^{\sigma'*} \quad (2.60)$$

is the density matrix.

The energy obtained as the expectation value of the Hamiltonian is the band-structure energy [81]. In order to obtain the total or Kohn-Sham energy of the system, it is necessary to subtract the double counting terms. Hence, after some algebraic manipulations, the energy can be written as:

$$\begin{aligned}
E^{KS} = & \sum_{\sigma\sigma'} \sum_{\mu, \vec{R}_\nu} \rho_{\mu\vec{R}_\nu}^{\sigma\sigma'} (T_{\vec{R}_\nu\mu} + V_{\vec{R}_\nu\mu}^{KB}) \delta^{\sigma\sigma'} + \sum_{I<J} E_{IJ}^{na}(R_{IJ}) + \sum_{I<J} \delta E_{IJ}^{loc}(R_{IJ}) + \\
& + \sum_I E_I^{atom} + \sum_I \int \delta n(\vec{r}) V_I^{na}(|\vec{r} - \vec{R}_I|) d\vec{r} + \frac{1}{2} \int \delta n(\vec{r}) \delta V^H(\vec{r}) d\vec{r} + \\
& + \int n(\vec{r}) \epsilon^{xc}(\vec{r}) d\vec{r} + \int n(\vec{r}) V^{ext}(\vec{r}) d\vec{r}
\end{aligned} \tag{2.61}$$

where

$$E_{IJ}^{na}(R_{IJ}) = \int V_I^{na}(|\vec{r} - \vec{R}_I|) n_J^{na}(|\vec{r} - \vec{R}_J|) d\vec{r} \tag{2.62}$$

$$\delta E_{IJ}^{loc}(R_{IJ}) = \frac{Z_I Z_J}{R} - E_{IJ}^{loc}(R_{IJ}) \tag{2.63}$$

$$E_{IJ}^{loc}(R) = \int V_I^{loc}(|\vec{r} - \vec{R}_I|) n_J^{loc}(|\vec{r} - \vec{R}_J|) d\vec{r} \tag{2.64}$$

and

$$E_I^{atom} = \int_0^\infty \left(V_I^{loc}(|\vec{r} - \vec{R}_I|) + \frac{1}{2} V_I^{atom}(|\vec{r} - \vec{R}_I|) \right) n_I^{atom}(|\vec{r} - \vec{R}_I|) 4\pi r^2 dr \tag{2.65}$$

Once the SCF procedure finishes, which means that the differences between input and output density matrices are small enough, the main physical properties can be obtained or calculate the forces on some atoms and relax them to a new configuration.

2.4 Electronic Transport

The problem of the electronic current flowing through a system under a bias voltage, is one of the most challenging issues in theoretical solid state physics. Various levels of approximations have been applied in order to grasp the different aspects of the underlying physics in such problem. The approximations run from the most basic as it is the Boltzmann formalism, until the modern and well developed *Non Equilibrium Green's Functions method* (NEGF). But before addressing a particular transport problem, one need to know what is the transport regime involved.

This can be known taking into account two parameters of the system: the momentum relaxation length (or electron mean free path), L_m , and the phase relaxation length, L_ϕ [92]. The momentum relaxation length is the average distance which an electron can travel before it loses its momentum, while the phase relaxation length is the average distance which an electron can travel until its original phase is destroyed. When the relevant distance L in a system is much larger than L_m and L_ϕ , the conductance depends on the length and it obeys the Ohm's law, so it is in the ohmic or diffusive regime. However, when the length of the device is shrunk and reaches mesoscale or even a smaller scale, as for example at single-molecule devices which are in the nanoscale, the system is no longer in the ohmic regime and the quantum character of the electrons needs to be considered. According to the two characteristic lengths, the electron transport in the smallest scales can be splitted into three regimes:

(i) Ballistic transport regime, $L \ll L_m, L_\phi$

Electrons can propagate freely from one lead to the other, without suffering any scattering. As consequence, their momentum and phase are roughly the same once the electron has passed through the device. The resistance is localized on the contacts and the conductance is independent of the scattering region length.

(ii) Coherent transport regime, $L < L_\phi$

Electrons travel along the device without suffering a change on their phase. The energy of the electrons is conserved, which means that they suffer elastic collisions with the scattering centers.

(iii) Incoherent transport regime, $L > L_\phi$

In this regime, the electrons can interact with other electrons, with phonons, etc., which produces a phase-breaking, which means inelastic scattering processes. There is a change in both the phase and momentum of the electron.

Even when the transport process is actually a tricky many-body problem of a system out of equilibrium where the electron may interact with structural impurities, phonons, magnons or other temperature dependent excitations, depending on the length of the device, and of the strength of the interactions which are present, the theoretical approach is more or less restrictive. One of the most widespread approximations, is the so-called Landauer-Büttiker formalism (LBF). This scheme is the basis of many other more involved methods and computational implementations. A brief review of it will be depicted in next section.

Landauer-Bütikker Formalism for Electronic Transport

In the LBF [93], the system under study is considered to be splitted in three regions: the scattering region (Ω) which is attached to two reservoirs L and R (figure 2.1). At zero applied voltage, the chemical potential of the two reservoirs are equal, but when a bias is applied to the device, these chemical potentials become different and the current flows through the system.

The problem is viewed as a scattering problem, and can be formulated in terms of incoming and outgoing electron waves propagating along the system and are scattered by a potential connecting the two leads. Then, the current flowing is related to the probability of the electron to be transmitted from one lead to the other.

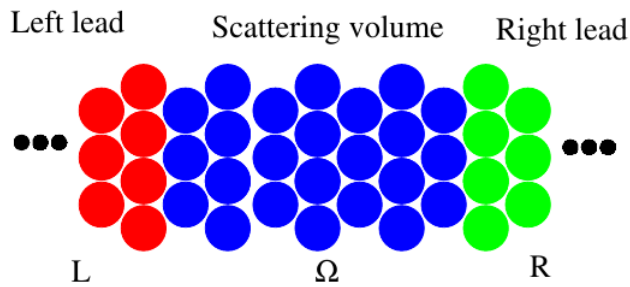


Figure 2.1: Basic setup of the Landauer approach to transport. The leads act as reservoirs and are assumed to be in thermal equilibrium. Image from [94].

Let the system be an ideal one-dimensional wire of length L between two leads. It is assumed the ballistic regime in the system. The electron density per unit length corresponding to a given perpendicular state in the momentum range between k and $k + dk$, including spin is:

$$n(k)dk = 2\frac{1}{2\pi}f(k)dk \quad (2.66)$$

where $f(k)$ is the Fermi distribution function. At finite bias, the Fermi functions of the leads are different, and the current flowing through the device is given by the current due to all electrons traveling from L to R minus the current due to the electrons traveling vice versa:

$$I = 2 \int e\nu(k)n(k)dk = 2 \int e\frac{\hbar k}{2\pi m_e^*} (f_L(k) - f_R(k)) dk \quad (2.67)$$

where $\nu(k)$ is the electron velocity and m_e^* the electron effective mass. At zero temperature, the Fermi function is a step function, and the above equation can be just written as:

$$I = 2 \int_{\sqrt{2m_e^*\mu_R}/\hbar}^{\sqrt{2m_e^*\mu_L}/\hbar} e \frac{\hbar k}{2\pi m_e^*} dk = 2 \frac{e^2}{h} V \quad (2.68)$$

where μ_L and μ_R are the chemical potentials of the left and right electrode respectively and $\mu_L - \mu_R = eV$ with V being the potential difference between the leads. From the equation 2.68, it follows that the maximum conductance of a one conduction channel with two spin states (where $G = I/V$) is $G_0 = 2e^2/h$. This is called the *quantum of conductance*. However, in actual systems, the connection between the scattering region and the leads is not ideal, and so, the conduction must be written as:

$$G = \frac{2e^2}{h} T(E_F) \quad (2.69)$$

where $T(E_F)$ is the transmission at Fermi level. The above equation is only valid when there is just one channel present in the system. For a finite width device with several quantum modes carrying electrons, the equation can be rewritten as:

$$G = \frac{2e^2}{h} \sum_{i,j} T_{ij}(E_F) \quad (2.70)$$

being T_{ij} the transmission coefficient of electrons traveling from i -th conducting mode at left electrode to the j -th conducting mode at the right electrode. Finally, the current at finite bias is expressed as:

$$I = \frac{2e}{h} \int_{-\infty}^{\infty} T(E, V) [f(E - \mu_L) - f(E - \mu_R)] dE \quad (2.71)$$

which is the Landauer-Bütikker formula. This formula tells that the main ingredient is the transmission function, which is usually derived from the Green's function. Due to the importance of the Green's functions, in next subsection an introduction to them will be given.

Green's Functions for an Open System

The Green's function method for calculating the transmission or conductance in open systems [92], which is going to be discussed here, is on the base of the two codes that have been used for transport calculations along this thesis. A deeper explanation on the codes as well as some remarks on them, will be given in next sections.

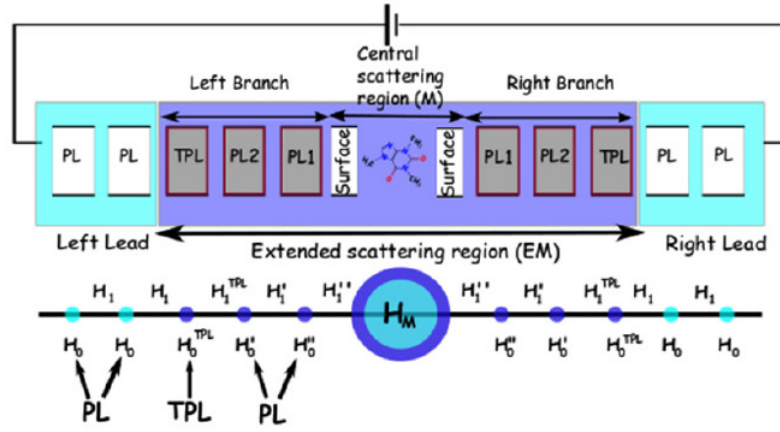


Figure 2.2: Completar.

Before going ahead, it is necessary to introduce the setup of the system, namely, how it is modeled (figure 2.2). This will bring an important concept: *principal layer* (PL), which can be defined as *the smallest cell that repeats periodically in the direction of the transport constructed in such a way to interact only with the nearest-neighbor PL's*. The system comprises an extended scattering region (extended molecule, EM, colored dark blue in figure 2.2) connected to external crystalline leads (colored light blue in figure 2.2).

So, it can be defined H_0 as the $N \times N$ matrix describing the interactions within a PL, where N is the total number of orbitals; H_1 is the $N \times N$ matrix describing the interaction between two PL's; finally, the EM region is described by H_M which is a $M \times M$ matrix and $H_{LM}(H_{RM})$ is the $N \times M$ matrix containing the interaction between the last PL of the left-hand side (right-hand side) and the extended molecule, which in the figure is called *Terminating Principal Layer* (TPL). It is worth noting that in actual calculations, the terminating principal layer Hamiltonian, must be close enough to that of corresponding lead Hamiltonian, in order to match smoothly with them. With the definitions given above, the final form of the Hamiltonian describing the whole system is then:

$$\mathcal{H} = \begin{pmatrix} \cdot & \cdot \\ \cdot & 0 & H_{-1} & H_0 & H_1 & 0 & \cdot & \cdot & \cdot & \cdot \\ \cdot & \cdot & 0 & H_{-1} & H_0 & H_{LM} & 0 & \cdot & \cdot & \cdot \\ \cdot & \cdot & \cdot & 0 & H_{ML} & H_M & H_{MR} & 0 & \cdot & \cdot \\ \cdot & \cdot & \cdot & \cdot & 0 & H_{RM} & H_0 & H_1 & 0 & \cdot \\ \cdot & \cdot & \cdot & \cdot & \cdot & 0 & H_{-1} & H_0 & H_1 & \cdot \\ \cdot & \cdot \end{pmatrix} \quad (2.72)$$

In the above Hamiltonian, calligraphic symbol \mathcal{H} means infinitely dimensional matrix. Furthermore, for a system which preserves time-reversal symmetry $H_{-1} = H_1^\dagger$, $H_{ML} = H_{LM}^\dagger$ and $H_{MR} = H_{RM}^\dagger$. Finally, as the overlap matrix \mathcal{S} has exactly the same structure of \mathcal{H} , it can be adopted the same notation to describe it and hence S_0, S_1, S_{LM}, S_{RM} and S_M , in complete analogy with the Hamiltonian counterparts.

The problem of an open system described with the Hamiltonian and overlap matrices given above is solved in the framework of the Green's functions. Specifically by computing the retarded Green's function for the whole system by solving the Green's function equation:

$$[\epsilon^+ \mathcal{S} - \mathcal{H}] \mathcal{G}^R(E) = \mathcal{I} \quad (2.73)$$

where \mathcal{I} is the infinite-dimensional identity matrix and $\epsilon^+ = \lim_{\delta \rightarrow 0^+} E + i\delta$. Then, taking into account the block-diagonal form for the Hamiltonian and overlap matrices given above, the Green's function equation can be written:

$$\begin{pmatrix} \epsilon^+ \mathcal{S}_L - \mathcal{H}_L & \epsilon^+ \mathcal{S}_{LM} - \mathcal{H}_{LM} & 0 \\ \epsilon^+ \mathcal{S}_{ML} - \mathcal{H}_{ML} & \epsilon^+ \mathcal{S}_M - \mathcal{H}_M & \epsilon^+ \mathcal{S}_{MR} - \mathcal{H}_{MR} \\ 0 & \epsilon^+ \mathcal{S}_{RM} - \mathcal{H}_{RM} & \epsilon^+ \mathcal{S}_R - \mathcal{H}_R \end{pmatrix} \times \\ \times \begin{pmatrix} \mathcal{G}_L & \mathcal{G}_{LM} & \mathcal{G}_{LR} \\ \mathcal{G}_{ML} & \mathcal{G}_M & \mathcal{G}_{MR} \\ \mathcal{G}_{RL} & \mathcal{G}_{RM} & \mathcal{G}_R \end{pmatrix} = \begin{pmatrix} \mathcal{I} & 0 & 0 \\ 0 & I_M & 0 \\ 0 & 0 & \mathcal{I} \end{pmatrix} \quad (2.74)$$

where the symbol R indicating retarded quantities has been dropped, and the Green's functions have been divided into the infinite blocks describing the left- and right-hand-side lead (L and R), the block describing the interaction between the leads and EM (LM and RM) and describing the finite block of the EM. In order to solve equation 2.74 it must be written the corresponding equation for the Green's function of the EM and surface PL's of the left and right lead, and then evaluated the retarded Green's functions for the EM G_M^R , which has the following form:

$$G_M^R(E) = [\epsilon^+ S_M - H_M - \Sigma_L^R(E) - \Sigma_R^R(E)]^{-1} \quad (2.75)$$

So, the semi-infinite leads have been taken into account through the retarded self-energies $\Sigma_{L,R}^R$, which are defined by:

$$\Sigma_L^R(E) = (\epsilon^+ S_{ML} - H_{ML})G_L^{0R}(E)(\epsilon^+ S_{LM} - H_{LM}) \quad (2.76)$$

$$\Sigma_R^R(E) = (\epsilon^+ S_{MR} - H_{MR})G_R^{0R}(E)(\epsilon^+ S_{RM} - H_{RM}) \quad (2.77)$$

G_L^{0R} and G_R^{0R} corresponds to the retarded surface Green's function of the leads, which means the lead retarded Green's function evaluated at the PL neighboring the EM. Now, G_M^R and Σ 's can be used to calculate the total transmission coefficients as:

$$T(E) = Tr[\Gamma_L G_M^{R\dagger} \Gamma_R G_M^R] \quad (2.78)$$

where

$$\Gamma_\alpha(E) = i[\Sigma_\alpha^R(E) - \Sigma_\alpha^{R\dagger}(E)] \quad (2.79)$$

It has been shown in such brief discussion, that the Green's function method provides an elegant and relatively easy way to grasp all the information about the electronic structure of a system comprising an extended molecule attached to leads. As it was pointed out before, this method, with slightly differences, is on the basis of the two transport codes utilized throughout this thesis GOLLUM and SMEAGOL.

2.4.1 Equilibrium Formalism: GOLLUM Code

GOLLUM [95] is a new code developed in recent years that computes charge, spin and electronic contribution to the thermal transport properties of a multi-terminal junctions. It is based on equilibrium transport theory, which means that it has a simpler structure, is faster and consumes less memory than other transport codes which are based on NEGF. GOLLUM is capable to read model tight-binding Hamiltonians as well as Hamiltonians calculated with the DFT code SIESTA.

The setup of a system which is going to be studied with GOLLUM is the same as was shown in figure 2.2. So, GOLLUM describes open systems splitting them into Leads (L, left and R, right) and the scattering region (EM), and defining the same Hamiltonians as before, for each part. However, in the construction of the total Hamiltonian of the system, there is a slight difference. As an example, for a two terminal device, the Hamiltonian of the system will be:

$$K = \begin{pmatrix} K_L & 0 & K_{LM} \\ 0 & K_R & K_{RM} \\ K_{ML} & K_{MR} & K_M \end{pmatrix} \quad (2.80)$$

where $K_{L,R,M} = H_{L,R,M} - ES_{L,R,M}$, $K_{LM,RM} = H_{LM,RM} - ES_{LM,RM}$ and $K_{ML,MR} = H_{ML,MR} - ES_{ML,MR}$. This different arrangement regarding to those shown in previous section enables the straightforward generalization of the approach to an arbitrary number of leads. As before, the transport properties can be obtained by computing the Green's function of the whole junction, simplified replacing the semi-infinite lead Green's functions by the surface Green's functions, obtaining an expression similar to 2.78.

The input Hamiltonians of the EM region and each lead, are provided by the DFT code SIESTA. To do this, separate calculations must be done: on the one hand, a calculation for the extended molecule region, and on the other hand, a calculation for each lead, which is reduced to one lead if they are equal.

Thermoelectric Properties

When a junction is subject to an electrostatic potential difference and a temperature gradient, electric and heat current flow from one electrode to another. With just an electrostatic potential, electrons move from the negative to the positive electrode, whereas the electric current is defined to flow in the opposite direction. With a temperature gradient, however, there is no rule of thumb that allows one to determine how the current flows without accurate information on the electronic structure, i.e., the transmission of the junction. If the transmission below the Fermi level is higher, electrons flow from the cold to the hot electrode, whereas the contrary happens if the transmission is higher above the Fermi level. The electrostatic potential and the temperature gradient generate also a heat current which, in general, flows from the hot to the cold electrode. For a system with spin polarization [97], this is summarize in the following equation:

$$\begin{pmatrix} I \\ \dot{Q} \end{pmatrix} = \frac{1}{h} \begin{pmatrix} e^2 L_0^t & \frac{e}{T} L_1^t \\ e L_1^t & \frac{1}{T} L_2^t \end{pmatrix} \begin{pmatrix} \Delta V \\ \Delta T \end{pmatrix} \quad (2.81)$$

where I and \dot{Q} are the electric and heat currents, respectively, and the moments $L_n^t = L_n^\uparrow + L_n^\downarrow$ ($n=0,1,2$) of the transmission coefficients are given by [98]:

$$L_n^\sigma = \int_{-\infty}^{\infty} (E - E_F)^n T^\sigma(E) \frac{\delta f(E, V, T)}{\delta E} dE \quad (2.82)$$

where f is the Fermi distribution function, which depends on voltage and temperature. Equation 2.81 can be expressed in terms of measurable thermoelectric quantities: the electric conductance G , thermopower S , Peltier coefficient Π , and the electronic contribution to the thermal conductance κ :

$$\begin{pmatrix} \Delta V \\ \dot{Q} \end{pmatrix} = \begin{pmatrix} R & S \\ \Pi & \kappa \end{pmatrix} \begin{pmatrix} I \\ \Delta T \end{pmatrix} \quad (2.83)$$

where

$$G = \frac{e^2}{h} L_0^t \quad (2.84)$$

$$S = -\frac{1}{eT} \frac{L_1^t}{L_0^t} \quad (2.85)$$

$$\Pi = \frac{1}{e} \frac{L_1^t}{L_0^t} \quad (2.86)$$

$$\kappa = \frac{1}{hT} \left(L_2^t - \frac{L_1^{t^2}}{L_0^t} \right) \quad (2.87)$$

The figure of merit can also be expressed in terms of the transmission moments by substituting the above expressions in the ZT definition:

$$ZT = \frac{1}{\frac{L_0^t L_2^t}{L_1^{t^2}} - 1} \quad (2.88)$$

The calculation of the thermoelectric properties listed above, has been implemented in GOLLUM, and they can be extracted from it.

Spectral Adjustment in Nanoscale Transport (SAINT)

A phenomenological scheme that improves the agreement between theoretical simulations and experiments, e.g., in single-molecule electronics, consists of shifting the occupied and unoccupied levels of the M region downwards and upwards respectively to increase the energy gap [99–102] of such a region. The procedure is conveniently called *spectral adjustment in nanoscale transport* (SAINT). This adjustment is implemented in GOLLUM. To do this, the code modifies the Hamiltonian operator of the M region as follows:

$$\hat{K}_M = \hat{K}_M^0 + \Delta_o \sum_{no} |\Psi_{no}\rangle \langle \Psi_{no}| + \Delta_u \sum_{nu} |\Psi_{nu}\rangle \langle \Psi_{nu}| \quad (2.89)$$

where $\Delta_{o,u}$ are energy shifts and (no, nu) denote the occupied and unoccupied states, respectively. By using the definition of the density matrix operator of the M region:

$$\hat{\rho}_M = \sum_{no} |\Psi_{no}\rangle \langle \Psi_{no}| \quad (2.90)$$

$$\hat{I} = \sum_n |\Psi_n\rangle \langle \Psi_n| \quad (2.91)$$

the above Hamiltonian can be rewritten as:

$$\hat{K}_M = \hat{K}_M^0 + (\Delta_o - \Delta_u)\hat{\rho}_M + \Delta_u\hat{I} \quad (2.92)$$

which can be put in matrix form:

$$K_M = K_M^0 + (\Delta_o - \Delta_u)S_M\rho_M S_M + \Delta_u S_M \quad (2.93)$$

In the simplest case, for a single-molecule junction, the shifts $\Delta_{o,u}^0$ are chosen to align the highest occupied and lowest unoccupied molecular orbital (i.e. the HOMO and LUMO) with (minus) the ionization potential (IP) and electron affinity (EA) of the isolated molecule:

$$\Delta_o^0 = \epsilon_{HOMO} + IP \quad (2.94)$$

$$\Delta_u^0 = -(\epsilon_{LUMO} + EA) \quad (2.95)$$

However, the Coulomb interactions in the isolated molecule are screened if the molecule is placed in close proximity to the metallic electrodes. Currently, GOLLUM takes this effect by using a simple image charge model [99], where the molecule is replaced by a point charge located at the middle point of the molecule and where the image planes are placed 1 Å above the electrodes' surfaces. Then the shifts are corrected by screening effects as follows:

$$\Delta_o = \Delta_o^0 + \frac{e^2}{8\pi\epsilon_0} \frac{\ln 2}{a} \quad (2.96)$$

$$\Delta_u = \Delta_u^0 - \frac{e^2}{8\pi\epsilon_0} \frac{\ln 2}{a} \quad (2.97)$$

where a is the distance between the image plane and the point image charge.

2.4.2 Non Equilibrium Green's Function: SMEAGOL Code

Spin and Molecular Electronics Algorithm on a Generalized atomic Orbital Landscape (SMEAGOL) is a quantum electronic transport code based on the non-equilibrium Green's function formalism (NEGF) [103, 104]. It uses DFT with the

numerical implementation contained in the code SIESTA. SMEAGOL has been designed for calculating the current-voltage characteristics of a system. The setup of the investigated system is the same that was shown in 2.2, and it utilizes the Green's function scheme discussed in a previous section, but with slightly modifications in order to take into account the non-equilibrium effects when the system is under bias voltage.

When an external bias voltage V is applied to the system, the charge distribution of the EM will be different of that at equilibrium since both the net charge and the electrical polarization are affected by the bias which in turn determine a new electrostatic potential profile with different scattering properties.

To have this modifications into account the following changes have to be introduced in the original formulation presented in section 2.4. First the only effect of the external bias in the electrodes is that of a rigid shift of the on-site energies. So, the Hamiltonian will become:

$$\mathcal{H} = \begin{pmatrix} \mathcal{H}_L + \mathcal{S}_L eV/2 & \mathcal{H}_{LM} + \mathcal{S}_{LM} eV/2 & 0 \\ \mathcal{H}_{ML} + \mathcal{S}_{ML} eV/2 & \mathcal{H}_M & \mathcal{H}_{MR} - \mathcal{S}_{MR} eV/2 \\ 0 & \mathcal{H}_{RM} - \mathcal{S}_{RM} eV/2 & \mathcal{H}_R - \mathcal{S}_R eV/2 \end{pmatrix} \quad (2.98)$$

The Hamiltonian of the EM depends on the density matrix ($H_M = H_M[\rho]$), which can be calculated using the lesser Green's functions $G_M^<$

$$\rho = \frac{1}{2\pi i} \int dE G_M^<(E) \quad (2.99)$$

where the lesser Green's function at non-equilibrium is given by [22, 92, 105–107]:

$$G_M^<(E) = iG_M^R[\Gamma_L f(E - \mu_L) + \Gamma_R f(E - \mu_R)]G_M^{R\dagger} \quad (2.100)$$

being $\mu_{L,R} = \mu \pm eV/2$, $f(x)$ the Fermi function, $\Gamma_{L,R} = \Gamma_{L,R}(E \mp eV/2)$ and $G_M^R(E)$ is that given in 2.75 where has been substitute $\Sigma_{L,R}(E)$ with $\Sigma_{L,R}(E \mp eV/2)$. The flow of a calculation utilizing the SMEAGOL is as follows: first, a trial charge density ρ_0 is used to compute $H_M[\rho]$. After this, $\Gamma_{L,R}$ and G_M^R are calculated. From them, the lesser Green's function is computed using the equation 2.100, which is fed back into equation 2.99 to find a new density ρ_1 . This process is repeated until a self-consistent solution is achieved, which means that $\|\rho^j - \rho^{j+1}\| \ll 1$. When this point is reached, the current can be calculated using [23]:

$$I = \frac{e}{h} \int dE \text{Tr}[\Gamma_L G_M^{R\dagger} \Gamma_R G_M^R] [f(E - \mu_L) - f(E - \mu_R)] \quad (2.101)$$

The transmission coefficient $\text{Tr}[\Gamma_L G_M^{R\dagger} \Gamma_R G_M^R]$ in this case, depends on both the energy E and the bias V .

Quantum Interference Effect in MetalloPorphyrins Wires

3.1 Introduction and Outline

In the search for molecular compounds that give rise to new or improved functionalities, compounds that include quantum interference effects [108] are specially appealing due to the large variation of conductance that such phenomena generate [109]. Porphyrin molecules, constitute in this respect promising candidates due to the presence of Fano-like [110] resonances that can greatly affect their transport or thermoelectric properties. These molecules play an essential role in many biological processes such as electron transfer, oxygen transport, photosynthetic processes and catalytic substrate oxidation [111]. Porphyrins have been extensively studied in the past by biologists and chemists [112–115]. However, an increasing number of theoretical [98, 110, 116, 117] and experimental [118, 119] physics studies have appeared in the past few years. Progress in the design of supramolecular structures involving porphyrin molecules has also been rather spectacular [120].

Porphyrins are cyclic conjugate molecules. Their parent form is the porphin, which is made of four pyrrole groups joined by carbon bridges and has a nearly planar D_{4h} symmetry [121]. The alternating single and double bonds in its structure make porphyrins chemically very stable. In addition, the macrocycle can accommodate inside a metallic atom, such as Fe (which is the base of the hemoglobin

in mammals), Cu (hemolymph in invertebrates), Mg (chlorophyll in plants), etc, which gives rise to metalloporphyrins. Large porphyrin systems can undergo certain ruffling distortions because of its peripheral ligands, its metallic atom inside or the environment [122]. It is precisely the large number of possible configurations, which give rise to a wide variety of interesting properties that make these molecules very attractive for molecular-scale technological applications.

From the electronic point of view, metalloporphyrins have frontier states (HOMO, LUMO) that extend across the whole molecule, owing to their conjugate character. The inclusion of metallic atoms with d states that couple to such frontier states can give rise to quantum interference effects due to the presence of an additional path through the metallic center [110]. It is not clear however how this additional path affects the electronic structure and generates different transport resonances for different metallic atoms. The combination of extended frontier orbitals and localized spin-polarized d states makes these systems promising for the exploitation of quantum properties in nanoelectronics, since large changes in the conductance are expected when spin-polarized d -generated resonances cross the Fermi level due to e.g. the influence of gate potentials or the attachment to the metallic center of other atoms or molecules.

In this chapter, a systematic study of a series of metalloporphyrins molecules is presented. The metallic atom placed inside the metalloporphyrins can be Fe, Co, Ni, Cu and Zn, so that the metalloporphyrins are denoted FeP, CoP, NiP, CuP and ZnP, respectively. In the first part, the electronic structure of the molecules, both in vacuum and sandwiched between gold electrodes, is addressed. In the gold-MPorphyrin-gold, the porphyrin molecule is attached to the gold surface by a thiol group and oriented perpendicular to it, as sketched in figure 3.1.

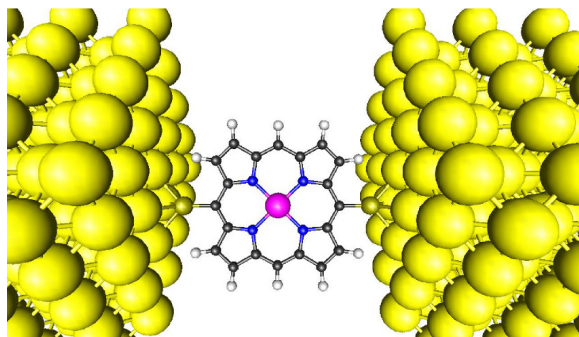


Figure 3.1: Schematic view of a Fe-porphyrin molecule between gold leads. Yellow, dark yellow, gray, black, blue and magenta represent gold, sulphur, hydrogen, carbon, nitrogen and iron, respectively

Then, the ab-initio transport properties so as a simple model which can describe the different features in transmission will be displayed and discussed. Finally, the thermoelectric properties of selected porphyrins are analysed from first-principles, and using the simple model.

3.2 Computational Method

The electronic structure calculations have been performed using SIESTA. For the exchange and correlation potential both the local density approximation (LDA), as parameterized by Ceperley and Adler [72], and the generalized gradient approximation (GGA), as parameterized by Perdew, Burke and Ernzerhof [123] have been used. SIESTA parameterizes the pseudopotentials according to the Troullier and Martins [124] prescription and factorizes them following Kleyman and Bylander [125]. Non-linear core corrections in the transition metal pseudopotentials were introduced to correctly take into account the overlap between the valence and the core charges [86]. It has been also used small non-linear core corrections in all the other elements to get rid of the small peak in the pseudopotential close to the nucleus when using the GGA approximation.

In the Linear Combination of Atomic Orbitals has been placed explicitly the s and d orbitals of gold as valence orbitals and employed a single- ζ basis (SZ) to describe them. A double- ζ polarized basis (DZP) was used for all the other elements (H, C, O, N, S and TM). The density, Hamiltonian, overlap and the matrix elements were calculated in a real space grid defined with an energy cutoff of 400 Ry. When performing the structural relaxations and transport calculations, a single k -point has been used, which is enough to relax the coordinates and correctly compute the transmission around the Fermi level in the case of gold electrodes. The coordinates were relaxed until all forces were smaller than 0.01 eV/Å. The U -parameter and the radii of the U -projectors have been varied and compared the results with experiments or previous simulations of the molecules. Fig. (3.1) shows the central part of the extended molecule in a gold-FeP-gold junction. The gold electrodes have been grown in the (001) direction, which has been taken as the z axis. Notice that the molecules have laid down on the XZ plane. The sulphur atoms have been contacted to the gold surfaces in the hollow position. It has been carried out a study of the most stable position and distance and have found, both in GGA and LDA, that the hollow configuration is more stable than the top and bottom sites, in agreement with previous results obtained for other molecules. The most stable distances are 1.6 Å and 1.8 Å for LDA and GGA, respectively. Finally a distance of 1.8 Å was chosen for all cases in order to make

a systematic study of geometrically identical systems. The transport calculations have been performed using the GOLLUM code. According to the transport formalism the junctions have been divided in three parts: left and right leads and extended molecule (EM). The EM block includes the central part of the junction (molecule attached to the gold surfaces) and also some layers of the gold leads to make sure that the electronic structure was converged to the bulk electronic structure. The same general parameters as in the bulk simulation (real-space grid, perpendicular k -points, temperature, etc.) and also the same parameters for the gold electrodes (bulk coordinates along x and y and basis set) have been used in the transport simulation.

As It was explained in chapter 2, the DFT+ U functional can be written as

$$E^{\text{DFT}+U} = E^{\text{DFT}} + \frac{U_{\text{eff}}}{2} \sum_{m,\sigma} n_{m,\sigma}(1 - n_{m,\sigma}) \quad (3.1)$$

where $U_{\text{eff}} = U - J$. In order to determine the influence of different U 's and cutoff radii and see how the results compare to previous experiments and calculations It was first studied the case of the bulk iron oxide FeO (wustite) [126], where DFT is known to give qualitatively different behavior (metallic instead of insulating character) [127]. The calculations were performed with $U = 4$ eV and $U = 4.5$ eV, which is the range of values most used in the literature for iron [127], and used projectors with different radii (see section 2.3.4). It was found that the results were very sensitive to such radii, i.e. the FeO gap was only reproduced for radii larger than 2.5 Bohr. The parameters that best fitted the experiments and previous calculations for FeO were $U = 4.5$ eV and $r_c = 5.5$ Bohr, which gave a gap of 2.5 eV (2.4 eV in Ref. [126]).

To reproduce previous theoretical results for the iron metalloporphyrin [116, 128], a $r_{\text{cut}} = 1.5$ Bohr had to be chosen, which is smaller than the values used for FeO. This is possibly justified by the fact that the values of U and the projectors radii depend on the environment where the strongly correlated atom is located. In case of the other transition metals (Co, Ni, Cu and Zn), U is expected to increase towards Zn but still be similar [78]. The same can be said when the metalloporphyrins are coupled between gold electrodes. Hence, the same parameters were used for all metalloporphyrins, which also simplified the comparison between different cases and made the study more systematic. The use of slightly different U 's for different elements does not affect qualitatively and quantitatively the transport results (only slight movements of some resonances around the Fermi level).

3.3 Electronic Structure

3.3.1 Isolated molecules

In this section, the electronic structure of the isolated molecules is discussed. The spin configuration of the molecules does not change when the U -term is included, except in the case of NiP, which becomes magnetic (see Tab. 3.1). The effect of the inclusion of the U -term can be seen in Fig. 3.2, which shows the Density of States projected (PDOS) onto the iron d states calculated with GGA and GGA+ U in FeP. It is seen that when U is included all gaps increase as a consequence of the movement of the filled orbitals to lower energies and the empty orbitals to higher energies. This gap increase is produced in all molecules, except in ZnP due to its closed shell (see Tab. 3.1).

In all molecules, the main contribution to the HOMO comes from the C $2p$ states, a small part of the S $3p$ and N $2p$ and some contribution of the $3d$ states of the metals (except in CuP and ZnP, which are completely formed by C, N and S states). Unlike to C, N and S states, which are not affected, the inclusion of the U -term can change the part of the HOMO coming from the $3d$ states. So, for the FeP and CoP cases, without U , both d_{xy} and d_{yz} make a contribution, remaining just d_{xy} when U is included. In NiP, d_{z^2} and $d_{x^2-y^2}$ contribute to the HOMO in GGA, but they vanish in GGA+ U calculation.

In LUMO, there are also $2p$ states from C and N and a contribution from $3d$ states of the metals. Again, when the U is introduced, the d states can suffer a rearrangement or even vanish. In FeP, with and without U , Fe $3d_{xy}$ is the most important in LUMO. However, in CoP the contribution changes from $d_{x^2-y^2}$ and d_{z^2} (GGA) to d_{xz} (GGA+ U) happening the opposite in NiP, namely from d_{xz} to d_{z^2} and $d_{x^2-y^2}$, when U is introduced. Finally, in CuP $3d_{xz}$ is the state that contributes to LUMO, but it changes its spin polarization in GGA+ U calculation.

By using the spatial projection of the density of states (local density of states, LDOS) it is also possible to understand where a particular molecular state is located. In Fig. 3.3 the LDOS projected on the molecular states associated to the d_{yz} (a) and d_{xz} (b) spin down states is shown (with an isosurface value of $0.001 \text{ eV}/\text{\AA}^3$), i.e. those peaks in the density of states where the weight of these d orbitals for spin down is largest, calculated with GGA. These states are located at $E - E_F = 0.3 \text{ eV}$ (yz) and 2.3 eV (xz) and move across the Fermi level when the atomic charge of the metal increases towards the Zn. Notice that in the d_{yz} case, due to the strong hybridization, the d peak splits in two and therefore the choice is ambiguous (see Fig. 3.2). The spatial distribution of each peak is similar however. On each d state it is possible to see the typical shape associated to it,

i.e. four lobes on the diagonals of the YZ or XZ planes, plus some charge on other atoms of the molecule due to hybridization with other molecular orbitals. Notice that the d_{yz} state does not interact too much with the nitrogens but rather with the carbons, specially with those located closest to the sulphur atoms. This produces an hybridization between this orbital and the carbon π states, as can be clearly seen in Fig. 3.3 (a) where the charge on the carbon atoms is mainly located on top of them. On the other hand, in the d_{xz} case, the lobes are directed exactly towards the nitrogen atoms and therefore this state interacts strongly with them. This interaction is σ -like, which is the type of interaction that nitrogen forms with the adjacent atoms, and therefore localizes the charge between atoms. The differences between the d_{yz} and d_{xz} orbitals and their coupling to different molecular states has a direct impact on the transport properties of some of these molecules, as it will be seen.

Table 3.1: Magnetic moments in units of μ_B (left part) and HOMO/LUMO energy gaps of the molecules in isolation, calculated with GGA and GGA+ U .

	Magnetic Moment		HOMO/LUMO Gap	
	GGA	GGA+ U	GGA	GGA+ U
FeP	2.00	2.00	0.48	1.10
CoP	1.00	1.00	0.90	1.80
NiP	0.00	1.00	1.50	1.60
CuP	1.00	1.00	0.75	1.40
ZnP	0.00	1.00	1.60	1.60

3.3.2 Molecules contacted by gold

The molecular orbitals of the porphyrines are broadened when the molecules are contacted by the gold electrodes. This broadening is however minimal for the d -orbitals of the transition-metal atom, because of their small coupling to the rest of the molecule. Even so, for example, a small broadening can be appreciated in Fig. 3.4 for FeP. Panel (b) of this Fig. 3.4 shows the PDOS projected on the orbital d_{yz} of iron, which is spread and reduced. This indicates a larger delocalization of this state as a consequence of its coupling to other molecular states that hybridize with the gold states. Something similar happens to the d_{xz} and, to a lesser extent, to the other d orbitals. This effect is maintained when the U -term is included. Also, as a consequence of hybridization and charge transfer the total spin of the molecule is reduced by more than a half as compared to the

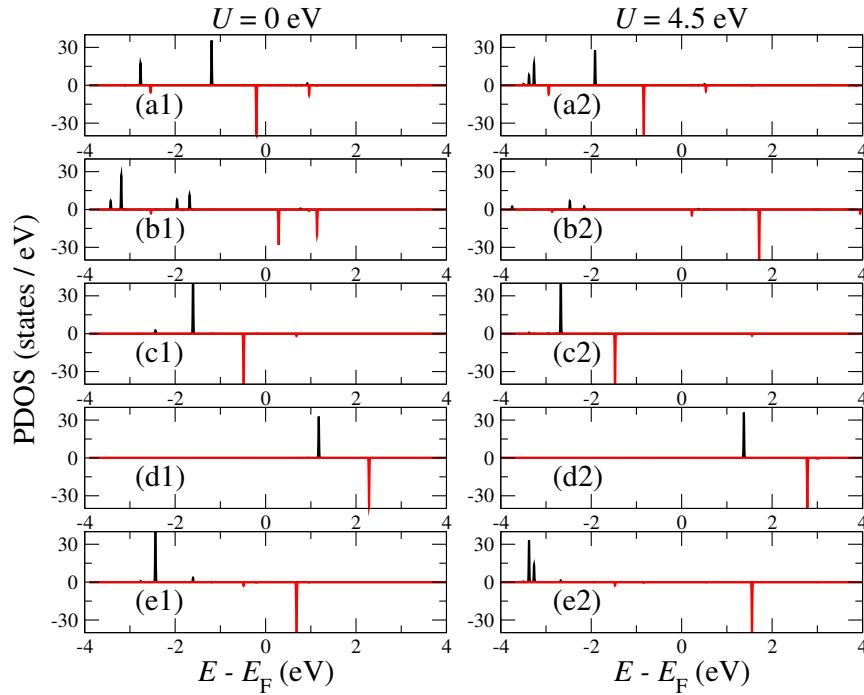


Figure 3.2: PDOS projected on $-d_{xy}$ (a), d_{yz} (b), d_{z^2} (c), d_{xz} (d) and $d_{x^2-y^2}$ (e) – for an isolated FeP molecule, computed with spin-polarized GGA. The left (1) and right (2) columns correspond to calculations without U and with $U = 4.5$ eV, respectively. Positive and negative values represent spin up and spin down electrons.

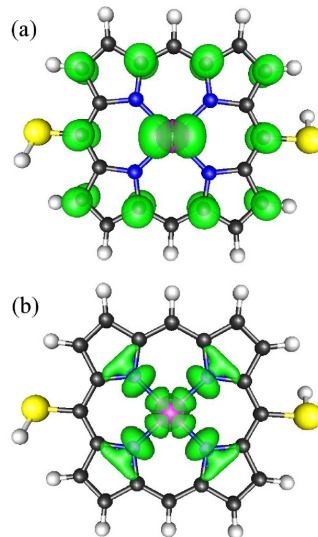


Figure 3.3: Spatial distribution of the density of states projected on d_{yz} (a) and d_{xz} (b) orbitals of the metallic atom computed with GGA. The first case has a clear π character, whereas second case has a more pronounced σ character.

isolated molecule (from $2 \mu_B$ to $1.07 \mu_B$ and $1.34 \mu_B$, for GGA and GGA+ U , respectively). This reduction comes mainly from the d_{yz} state, which crosses the Fermi level as a consequence of the spreading.

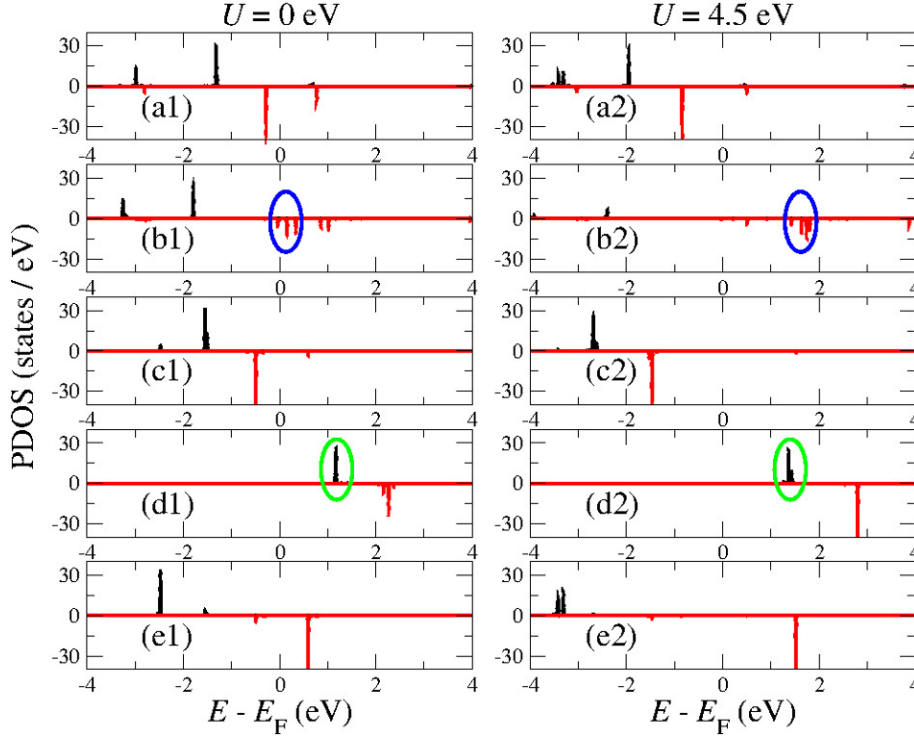


Figure 3.4: PDOS projected on the Fe d states (a) d_{xy} , (b) d_{yz} , (c) d_{z^2} , (d) d_{xz} and (e) $d_{x^2-y^2}$ of a contacted FeP molecule, computed with spin-polarized GGA. Positive and negative values represent spin up and spin down electrons.

In molecules other than FeP and CoP, the broadening of resonances is not so clear, because the d states become more localized when the atomic number increases. The case of Ni is striking because the differences between the isolated and contacted molecules are not only quantitative but qualitative (the spin calculated with U decreases from $2 \mu_B$ to $0 \mu_B$). This can be explained by taking into account that electrons in the d_{xz} and $d_{x^2-y^2}$ can be more delocalized in the contacted molecule, which decreases the effect of Hund's interaction. As a consequence, the contacted molecule loses its magnetism (even after including the U -term).

3.4 Transport Properties

3.4.1 Zero-bias

In this section, firstly, the impact of the U -term on the transport properties of the junctions will be discussed. It was found that the impact is largest in FeP and CoP

because they have the strongest electron correlations. The zero-bias transmission coefficients $T(E)$ are shown in Fig. 3.5, computed using spin-polarized GGA. Both systems present Fano-like resonances close to the Fermi level that move upwards (Fe) or downwards (Co) when $U = 4.5$ eV is included. The Fano resonance in FeP (no U) is spin-polarized, leading to a strong spin-filtering behavior. However, including the U -term kills the resonance as a consequence of changes in the coupling between the d -state and the molecular orbitals. For CoP, including the U -term reduces the spin polarization and moves several of the sharp resonances (in particular the clear Fano resonances appearing at about -0.7 eV, which is moved to -1.6 eV). From these results it is clear that accounting for strong correlations is necessary to accurately describe these systems. We will therefore discuss from now on the results obtained using spin-polarized GGA+ U .

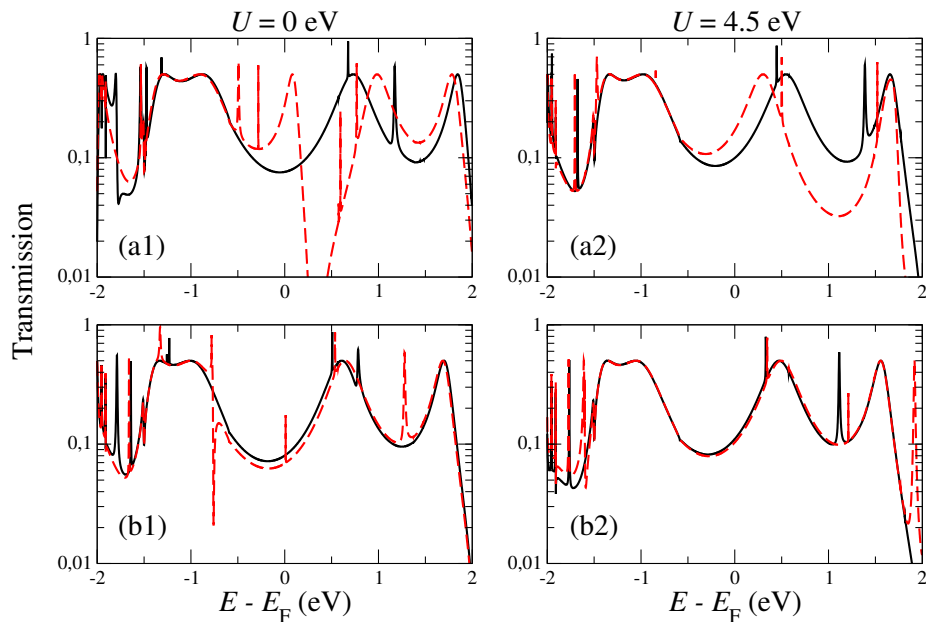


Figure 3.5: Transmission coefficients of a FeP (a) and a CoP (b) contacted by gold electrodes, computed with spin-polarized GGA. Left (1) and right (2) columns correspond to calculations with $U = 0$ eV and $U = 4.5$ eV. Continuous and dashed lines represent spin up and spin down electrons.

The zero-bias transmission $T(E)$ of all the molecules is shown in Fig. 3.6. As can be seen, four very broad Breit-Wigner resonances appear at energies about -1.4, -1.0, 0.5 and 1.5 eV (HOMO-1, HOMO, LUMO and LUMO+1). Resonances with the same shape at the same energy appear in the transmission coefficients of the contacted porphyrin molecule, which has no metallic atom. They therefore correspond to the conjugated molecular orbitals of the porphyrines, associated mainly to the sulphurs (HOMO) and the carbons and nitrogens (HOMO-1, LUMO and LUMO+1). Superposed to them, there appear a number of sharp peaks,

which are found to be either sharp Breit-Wigner or Fano resonances. Notice that the sharp peak at $\sim 0.3-0.5$ eV marked by a red ellipse remains at the same position for all the porphyrines. This peak also appears in the porphyrin junction. It corresponds to a sharp Breit-Wigner resonance associated to a weakly coupled molecular orbital with weight in the carbon and nitrogen atoms. A clear Fano resonance marked by a blue ellipse can be seen for the FeP and CoP junctions at ~ -1.5 eV. This resonance moves down and disappears from the energy window in the following junctions.

In contrast, the sharp resonance marked by a green ellipse which looks like a sharp Breit-Wigner resonance is actually a masked Fano resonance. Notice that it changes its energy position from FeP to ZnP, starting at ~ 1.4 eV for FeP, moving down in energy from FeP to CuP, appearing very close to the Fermi level on CuP, and disappearing for ZnP. Notice that it is spin-polarized except in the NiP junction. It must be stressed that these three resonances appear regardless of the kind of calculation.

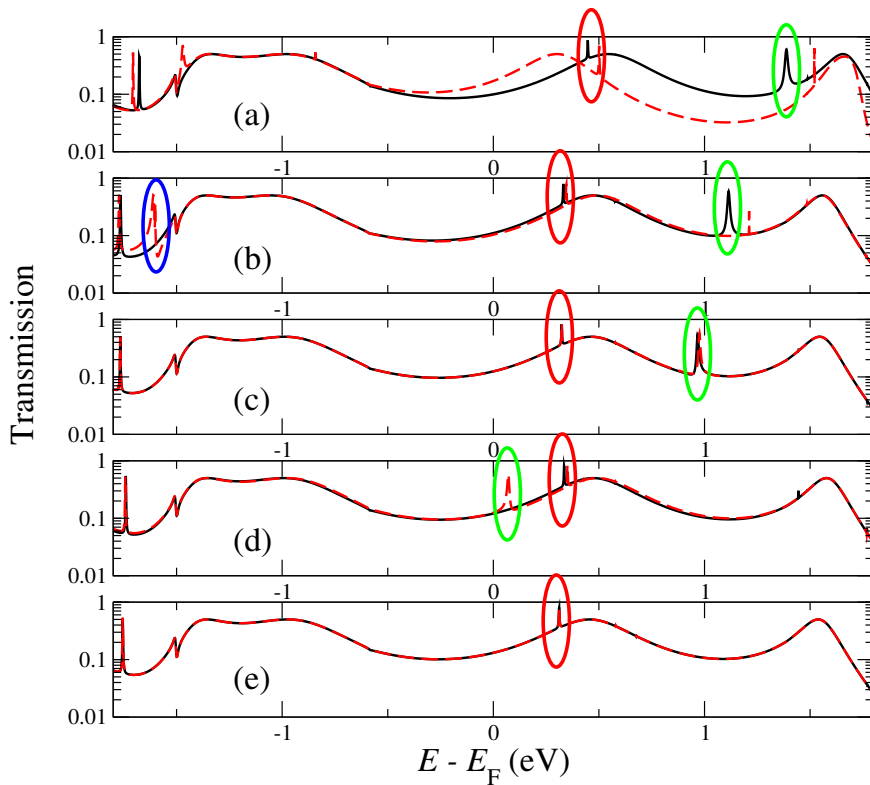


Figure 3.6: Transmission coefficients of a (a) FeP, (b) CoP, (c) NiP, (d) CuP and (e) ZnP molecules contacted by gold electrodes, computed with spin-polarized GGA and $U = 4.5$ eV. Continuous and dashed lines represent spin up and spin down electrons. The red ellipse circles a sharp Breit-Wigner resonance. The blue ellipse signals a Fano resonance. The green ellipse indicates a masked Fano resonance.

Simple Model For Fano-Like quantum interference in molecule electronic systems

A simple model which can grasp the features in Transmission shown in last section, will be introduced. This model describes quantum interference effects arising from Fano resonances [102, 129] in single- molecule junctions, where a metallic atom with localized d -orbitals resides in the backbone of the molecule. The existence or not of Fano resonances in a given junction can be elucidated by looking at the energy dependence of the transmission coefficient $T(E)$. The hallmark for a Fano resonance is the appearance of a sharp peak followed by a strong dip (or the reverse) in $T(E)$. However, these features might be masked by neighboring Breit-Wigner resonances. The model can be thought of as the minimal model that describes the masking or smoothing of Fano resonances inside the HOMO-LUMO gap. It will be only considered those molecular orbitals in the neighborhood of the Fermi level which have the strongest coupling to the leads. Specifically, the model includes three molecular levels: a σ level below the HOMO, one level (S) associated mainly to the linker atoms (sulphurs) that represents the HOMO and a π level which represents the LUMO. Finally, the model includes a single d orbital with no direct coupling to the electrodes, but coupled instead to either the σ or the π levels, depending on the symmetry of the molecule. The model and its two possible couplings is sketched in Fig. 3.7 (a) and (b), respectively. So, starting from the following Hamiltonian:

$$\hat{\mathcal{H}} = \hat{\mathcal{H}}_{\text{gold}} + \hat{\mathcal{H}}_{\text{M}} + \hat{\mathcal{H}}_{\text{gold-M}} \quad (3.2)$$

$$\hat{\mathcal{H}}_{\text{gold}} = \sum_{k,\sigma} \epsilon_k c_{k\sigma}^\dagger c_{k\sigma} \quad (3.3)$$

$$\begin{aligned} \hat{\mathcal{H}}_{\text{M}} = & \sum_{\sigma} \epsilon_{d\sigma} \hat{d}_{\sigma}^\dagger \hat{d}_{\sigma} + \sum_{i=1,2,3,\sigma} \epsilon_i \hat{c}_{i\sigma}^\dagger \hat{c}_{i\sigma} + \\ & + \sum_{i=1,3} t_i \left(\hat{c}_{i\sigma}^\dagger \hat{d}_{\sigma} + \hat{d}_{\sigma}^\dagger \hat{c}_{i\sigma} \right) \end{aligned} \quad (3.4)$$

$$\hat{\mathcal{H}}_{\text{gold-M}} = \sum_{k,i,\sigma} T_i (c_{k\sigma}^\dagger c_{i\sigma} + c_{i\sigma}^\dagger c_{k\sigma}) \quad (3.5)$$

where the operators $\hat{c}_{i,\sigma}$, $i = 1, 2, 3$ represent the σ level (HOMO-1), S Level (HOMO) and π level (LUMO) molecular levels and the operator \hat{d} represents the d level associated to the central metallic atom. In this model, the leads are featureless, meaning that they are treated in the wide-band approximation, so that its density of states ρ_e and therefore the Gamma matrices ($\Gamma_i = T_i^2 \rho_e$) are constant. Finally, assuming that the d level is spin polarized so that only the spin-up d level enters the relevant energy window, the Hamiltonian and the Gamma

matrices can be written as:

$$\hat{H} = \begin{pmatrix} \epsilon_\sigma & 0 & t_\sigma & 0 \\ 0 & \epsilon_S & 0 & 0 \\ t_\sigma^* & 0 & \epsilon_d & t_\pi \\ 0 & 0 & t_\pi^* & \epsilon_\pi \end{pmatrix}, \quad (3.6)$$

$$\hat{\Gamma}_L = \hat{\Gamma}_R = \begin{pmatrix} \Gamma_\sigma & 0 & 0 & 0 \\ 0 & \Gamma_S & 0 & 0 \\ 0 & 0 & 0 & 0 \\ 0 & 0 & 0 & \Gamma_\pi \end{pmatrix} \quad (3.7)$$

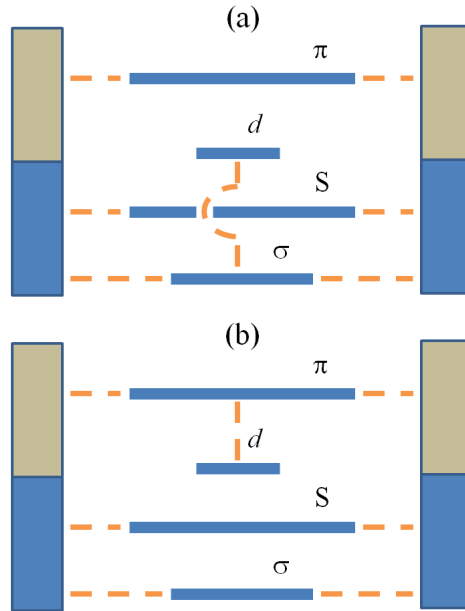


Figure 3.7: Schematic representation of the simple model. Case (a) corresponds to the d level coupled to the σ state and case (b) to the d level coupled to one of the π levels.

To facilitate the comparison with the ab-initio results in previous section the following values have been chosen for the on-site energies and the couplings: $\epsilon_\sigma = -2$, $\epsilon_S = -1$, $\epsilon_d = 0$, $\epsilon_\pi = 0.6$, $\Gamma_\sigma = 0.04$, $\Gamma_S = 0.06$, and $\Gamma_\pi = 0.06$, where all energies are measured in eV . For model (a), $t_\sigma = -0.4$ and $t_\pi = 0$, while for model (b) $t_\sigma = 0$ and $t_\pi = -0.2$. From the Hamiltonian and the Γ matrices it is easy to calculate the retarded Green's function and the transmission, which are given by

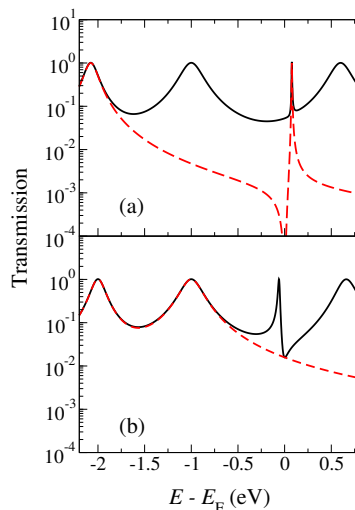


Figure 3.8: (a) Transmission coefficients calculated for model (a) described in the text and schematically shown in Fig. 3.7 (a). The black solid line corresponds to the full model, whereas the red dashed corresponds to a simplified model where the HOMO (S) and π orbitals have been dropped from the calculation. (b) Transmission coefficients calculated for model (b) described in the text and schematically shown in Fig. 3.7(b). The black solid line corresponds to the full model, whereas the red dashed corresponds to a simplified model where the d and π levels have been dropped from the calculation.

$$\hat{G}^R(E) = [E\hat{I} - \hat{H} - i\hat{\Gamma}]^{-1} \quad (3.8)$$

$$T(E) = \text{Tr} [\hat{\Gamma}\hat{G}^{R\dagger}(E)\hat{\Gamma}\hat{G}^R(E)] \quad (3.9)$$

The transmissions obtained for models (a) and (b) are shown in Fig. 3.8. The solid lines represents the transmission calculated with the full model. The dashed line in Fig. 3.8 (a) shows the transmission when the HOMO (S) and π orbitals in model (a) are dropped and only the d and σ orbitals are considered. This is to show that a clear-cut Fano resonance emerges at the d level on-site energy. Such resonance is masked when the HOMO (S) and π orbitals are re-integrated back into the calculation because the additional transmission hides the dip. This leaves what looks at first sight a conventional and very narrow Breit-Wigner resonance. The transmission of the full model in Fig. (3.8) (b), however, features a clearer Fano resonance. In this case, the dip of the resonance is not washed out, because the transmission of the σ and HOMO (S) resonances (dashed line) can not completely mask the drop in transmission at higher energies. Therefore, when a localized d level is present in a molecule and coupled to one molecular orbital, quantum interference may appear in two different ways: like a narrow peak close to the d level on-site energy (a masked Fano resonance) or like a clear Fano resonance (resonance followed by antiresonance, only partially masked by other

molecular resonances). Notice that by looking at the parity of the clear Fano resonance (resonance-antiresonance, or vice versa) it is possible to determine to which molecular orbital it is coupled. If the molecular orbital is lower in energy then the antiresonance appears first (see the dashed line in Fig. 3.8 (a)), whereas if the molecular orbital is higher in energy the resonance comes first.

Now, taking into account the previous data and the simple model presented in this section, it is possible to explain the behaviour of these junctions as follows. The d orbitals are localized states that couple to certain molecular states. Such configurations are similar to those where a side state couples to a molecular backbone, which produce Fano resonances in the transmission coefficients. The d orbitals generate therefore Fano resonances associated to one or several molecular states. If, for example, the molecular state is the LUMO and the d orbital is in the HOMO-LUMO gap, the effect of the Fano resonance is clearly seen because it affects the transmission in the gap, which has a large weight from the LUMO. The Fano resonance does not go to zero, however, because of the tails of the transmission of other molecular states. If, on the other hand, the d orbital couples to a state below the HOMO or above the LUMO, the effect of the Fano resonance turns out to be much smaller because the transmission of such state does not affect too much the transmission in the HOMO-LUMO gap. There is however one effect produced by the Fano resonance, which is related to its peak. This peak has a transmission of 1 at the tip (without additional molecular resonances) and therefore can be seen above the background of the transmission of other states. It can be therefore confirmed that the sharp Breit-Wigner-like resonances that appear at different energies come in reality from Fano resonances. In view of these results it is possible to conclude then that the clear Fano features inside the HOMO-LUMO gap are produced by d orbitals that couple to the π states, which appear mainly on the LUMO. One d orbital responsible for such a feature is clearly the d_{yz} , as seen in Fig. 3.3. The isolated sharp resonances are also Fano features but are generated by d orbitals, such as the d_{xz} , that couple to σ states above the LUMO or below the HOMO.

3.4.2 Finite-bias

From the zero bias transmission coefficients it is not clear whether the sharp resonances associated to the d levels can give rise to distinctive features or even survive when a finite bias is applied. To clarify that, a finite bias has been applied by using an approximation that includes non-equilibrium effects by shifting differently the levels associated to the electrodes and the molecule [130]. The focus will be put

on the CuP (GGA+ U), which has a spin-polarized resonance very close to the Fermi level, and compared it to the ZnP, which has no sharp resonances coming from the d levels. The bias applied is small but enough to cover the resonance with the integration window. The resonance, however, does not remain static but moves to lower energies, as can be seen in Fig. 3.9 (a). To further enhance the effect of the resonance a gate voltage (3 V) has been also applied on the central part of the junction, which brought the resonance even closer to the Fermi level, as can be seen in Fig. 3.9 (b).

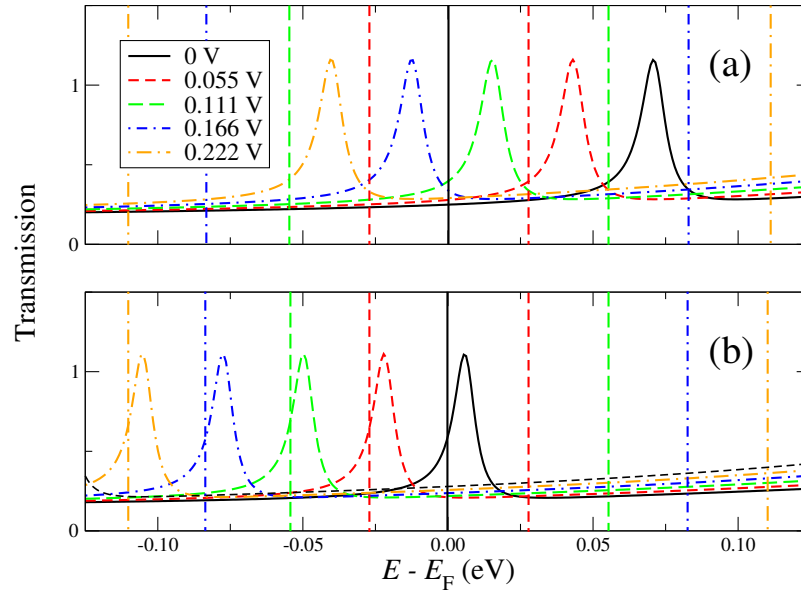


Figure 3.9: Spin-down transmission coefficients around the Fermi level for CuP (GGA+ U) under different bias voltages and a gate voltage of 0 V (a) and 3 V (b).

The $I - V$ characteristics calculated with the resonance differ from those obtained without it (ZnP), as can be seen in Fig. 3.10. These small differences become more evident when the derivative of the current is taken. Without gate, the resonance produces a peak when the bias reaches it, at approximately 0.065 V. When the gate is included the peak develops at zero voltage. The resonance produce therefore different $I - V$ characteristics and can increase the total value of the conductance by a factor larger than 2 at the peak maxima. Notice however that these values are masked by the spin-up conductance, which is the same for all cases. If only the spin-down conductance is taken into account the changes are larger. These results also prove that a spin-polarized current can be generated under finite bias since the peaks are only associated to the spin-down component.

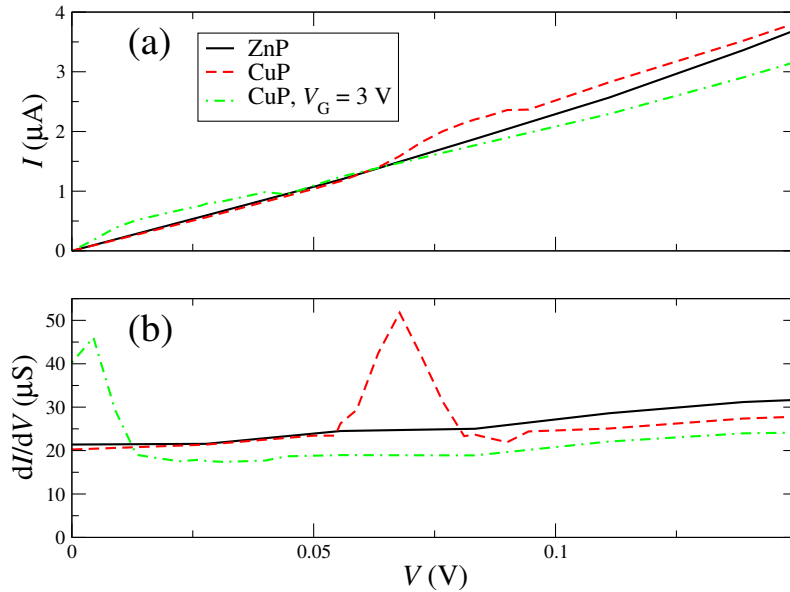


Figure 3.10: Total current (a) and its derivative (b) for ZnP and CuP porphyrins. A gate voltage of 3 V in the central part of the junction is also included in the CuP case.

3.5 Thermoelectric Properties of CuP

It is known that molecular junctions that show sharp features around the Fermi level could be very good candidates to act as thermoelectric enhancers. It has been displayed in a previous section that CuP shows a resonance close to the Fermi level which is a Fano resonance, as it was demonstrated. This property makes it especially appealing for thermoelectricity since such resonance can be employed to finely tune the thermoelectric response with a gate voltage. Hence, the thermoelectric properties of the CuP between gold electrodes will be addressed in this section.

From the transmissions (see Fig. 3.6) the thermoelectric properties have been calculated by using the scheme explained in section 2.4.1. The temperature dependence on the horizontal axis enters in the Fermi distribution function, as it was explained. The results are shown in Fig. 3.11. It can be seen that the temperature evolution of some quantities has different features and changes more dramatically when the state moves. The electric conductance is rather constant and the thermal conductance increases linearly. The Seebeck coefficient shows however a dip at low temperatures, and becomes almost constant as the temperature increases. The dip disappears when the state moves to higher energies and the magnitude decreases to more negative values with T . The figure of merit is small but has a peak at low temperatures. Such peak disappears when the U -term is included and is substituted by a smooth increase. This evolution is a consequence of the

presence at the Fermi level of a sharp spin-polarized resonance which moves closer to the LUMO when the U -term is included. Such resonance, which is just a bit above the Fermi level gives rise to large derivatives and therefore dramatically increases, in absolute value, the Seebeck coefficient S . This coefficient is however not very large because the sum of the transmission of both spin channels is not small.

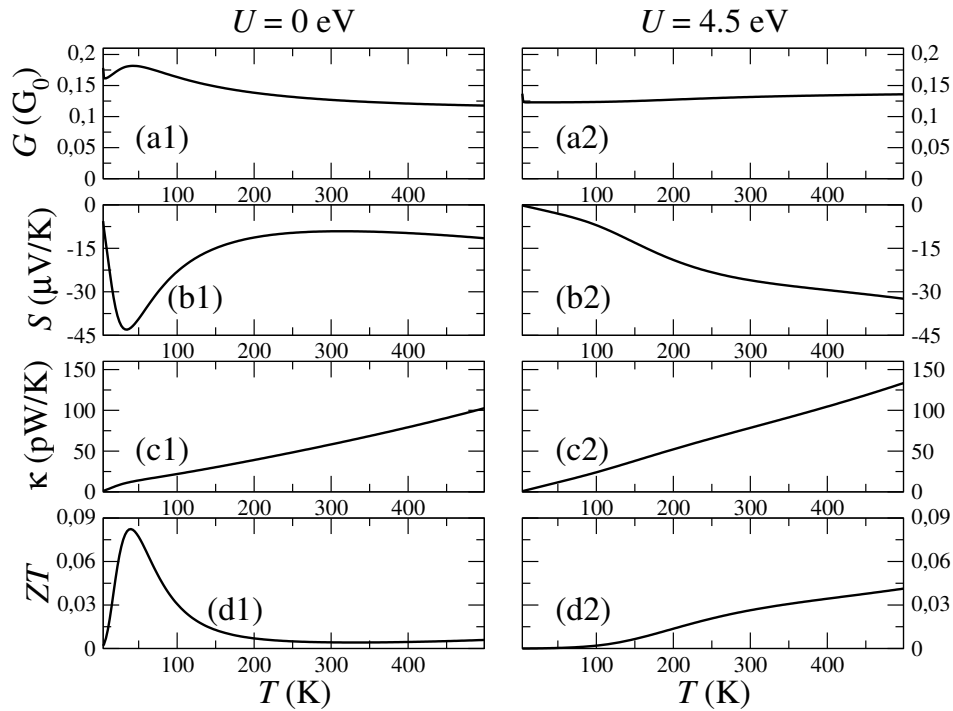


Figure 3.11: Thermoelectric coefficients for Cu metalloporphyrins dithiolate between gold electrodes, calculated with GGA and $U = 0$ eV (1) and $U = 4.5$ eV (2). From top to bottom, conductance G (a), Seebeck coefficient S (b), thermal conductance κ and figure of merit ZT .

The copper molecule could be a candidate to show large thermoelectric properties due to the presence of the Fano-masked resonance close to the Fermi level. However, the introduction of the U moves the resonance to higher energies and decreases the thermoelectric response. It is then interesting to consider the case of applying a gate voltage that brings back the resonance to the Fermi level. It can be seen in Fig. 3.12 that moving the resonance to lower energies increases the absolute value of both S and ZT ¹. The highest values are obtained when

¹Notice the value of the figure of merit would be further decreased by taking into account the phonon thermal conductance, κ_p , i.e. $ZT = S^2GT/(\kappa + \kappa_p)$. In this study, just the electronic contribution is accounted. In general, the phonon contribution, which can be obtained by calculating the dynamical matrix [129], can be relatively large at high temperatures if perfect electrodes are used. However, it can be greatly decreased by nanostructuring the electrodes to include phonon band gaps or using disordered electrodes that increase phonon scattering [131–133]

the largest slope of the resonance is just at the Fermi level ($V_G = 2.5$ V). Beyond that point S and ZT decrease ($V_G = 3.5$ V). The increase of the thermoelectric properties is not very spectacular however due to the fact that the resonance is not extremely sharp. More acute resonances can be however obtained by decreasing the coupling between the molecule and the gold electrodes, which reduces the width of all transmission features. It is shown in Fig. 3.13 results for a system where the distance between the gold electrodes and the sulphur atoms on each side increases by 0.8 \AA relative to the equilibrium configuration. As can be seen, now the resonance is very sharp and the changes in the thermoelectric properties are larger. Notice that the thermopower changes sign when the resonance crosses the Fermi level due to the change of slope. Based on these results It can be claimed that stretching molecular electronic junctions increase in general the thermoelectric performance.

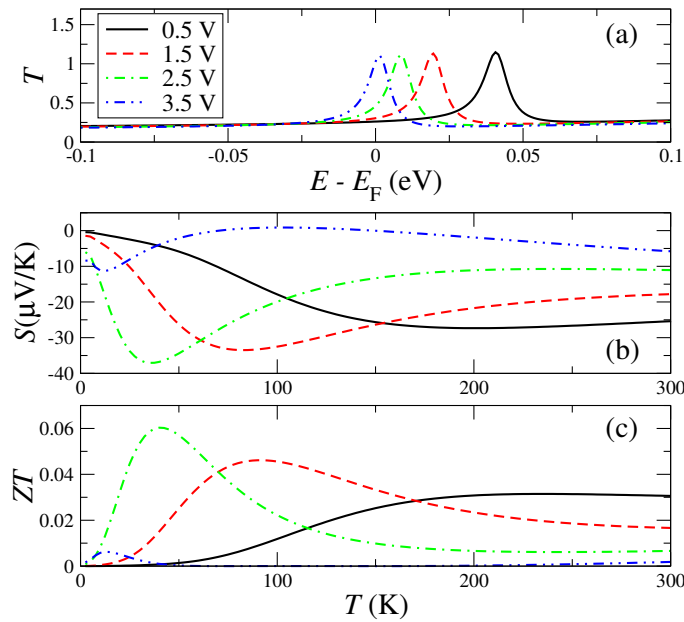


Figure 3.12: Spin-polarized transmission as a function of energy (a) and Seebeck coefficient (b) and figure of merit (c) as a function of temperature for Cu metalloporphyrins dithiolate between gold electrodes, calculated with GGA, $U = 4.5$ eV and different gate potentials.

3.6 Remarks

On the one hand, the electronic and transport properties of metalloporphyrins between gold electrodes have been studied. Also, It has been proposed a simple model that can explain the main features of the zero-bias transmission. It

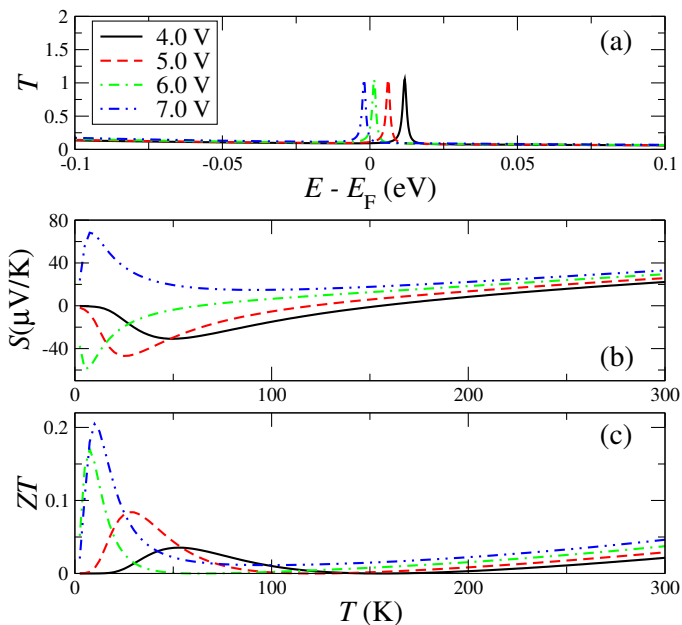


Figure 3.13: Spin-polarized transmission as a function of energy (a) and Seebeck coefficient (b) and figure of merit (c) as a function of temperature for stretched Cu metalloporphyrins dithiolate between gold electrodes (the contact distance between the molecule and the electrodes was increased 0.8 Å on each side from the equilibrium configuration), calculated with GGA, $U = 4.5$ eV and different gate potentials.

was found that the coupling to the electrodes changes only slightly the electronic properties but the magnetic moments decrease as a consequence of charge transfer and hybridization with the electrodes. Two types of features have been found in the transport properties, which are shown to be masked Fano resonances by the use of the simple model. The $I - V$ characteristics have been also computed and shown that the presence of such resonances can significantly change the value of the finite-bias conductance.

Based on these results and in particular on the evolution of the resonances as a function of the degree of freedom that the choice of different $3d$ atoms provides to position the relevant d levels and the intra-atomic potential, metalloporphyrin-based junctions are proposed as an excellent playground for the control and exploitation of Quantum Interference in functional molecular electronics devices. Whenever a given atom or molecule couples either to the metallic atom or to other parts of the molecular backbone the changes in the metallic d states affect the Fano resonances. This mechanism can generate sharp increases or decreases in the zero-bias conductance. Differences between spin-up and spin-down transmissions, which are specially important in the cases of iron, cobalt and copper, can also give rise to spin-filtering behavior.

On the other hand, the thermoelectric properties of that junctions have been calculated from first-principles. The Fano resonances greatly enhance the thermopower and figure of merit when they cross the Fermi level. The maximum value of these quantities depends on the coupling between the molecule and the electrodes. It was found that reducing it greatly enhances the figure of merit.

Strategies for Conductance Variability Reduction

4.1 Problem variability in single-molecule experiments

As It was mentioned in the introduction, a significant hindrance in molecular electronics arises from the large variability in the behaviour of conductance present in single-molecule junctions. Among the sources of this variability it can be found the non-uniformity of the electrode-molecule contacts. This means that as well as how the molecule is bonded, a huge number of arrangements of atoms could be done in the junction. So, every molecule may bind via their terminating or intermediate groups to different sites of the electrode surface, where the binding energy of these configurations usually is energetically similar. Small changes in the geometry of molecule-electrode system, can produce large differences in conductance, resulting in the observation of multiple conductance peaks of considerable width in the conductance histograms typically used to analyse statistically a significant number of measurements.

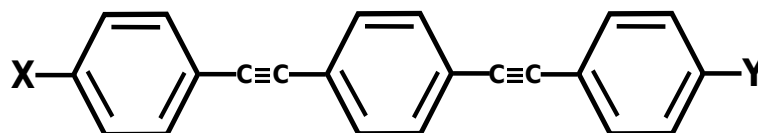
Thus, using either alkanes or conjugated molecules bridges with a wide range of different anchoring groups (thiol, pyridine, amine, etc.), instead of a unique value for the single molecule conductance, a number of single molecule conduc-

tance values appears [134–137]. In most experiments, the number of these peaks is at least three, which have been arbitrarily termed low (L) or A-type, medium (M) or B-type and high (H) or C-type conductance groups and are attributed to different contact geometries between the molecule and the electrode. So, the higher conductance groups (M and H) are more common on stepped or rough surfaces step sites while the lower conductance (L) groups appear mostly on flat surfaces regions. In the former case, It is possible that the molecule bind not only by terminating groups but also through the backbone, unlike the latter case, where the binding is most likely between the end group and flat surface.

The different contact modes have been well illustrated by studies of molecular junctions. For example, It is well-known that in molecular junctions using the thiol as terminating group, the coupling depends strongly on the exact surface site to which the sulphur atom binds, with coordination of the sulphur contact at a hollow position giving rise to larger couplings than the top or bridge configurations. Due to these different couplings, the junction conductance changes a lot as the binding site moves through these various configurations, leading to several broad conductance peaks. Other contacting groups such as amine ($-\text{NH}_2$) reduce the number of effective binding positions, but still produce several conductance peaks as a consequence of interactions between the contact group or even the backbone with surface defects.

In view of the above, the search for groups which reduce the variability in the molecule-electrode contact, either reducing the various bonds, preventing backbone contact or both, is a primary goal in the framework of molecular electronics. In this respect, one of the most promising candidates to be explored is *trimethylsilylethynyl* (TMSE, $-\text{C}\equiv\text{CSiMe}_3$). This terminating group shows, among other interesting features, the ability to form large homogeneous SAM's (with areas of several hundreds of nm^2) or a strong Au-Molecule bond [138]. But maybe the most appealing characteristic of this terminating group, is the observation of a single well resolved peak in the conductance histograms [139].

In recent experiments performed by groups from University of Zaragoza and University of Liverpool [140], the reduction of the variability in conductance when the *trimethylsilylethynyl* terminating group is used, was also demonstrated. In such experiments, they measured the conductance through an *oligo(phenylene)ethynylene* (OPE)-based molecules, with a series of anchoring groups (figure 4.1). OPE derivatives are molecules made by phenyl rings connected with triple bonds, hence they are fully conjugated molecules. The experiments were made at room temper-



Compound	X	Y
1	-NH₂	-NH₂
2	-NH₂	-C≡CSiMe₃
3	-C≡CSiMe₃	-C≡CSiMe₃
4	-C≡CSiPrⁱ₃	-C≡CSiPrⁱ₃
5	-C≡CCMe₃	-C≡CCMe₃

Figure 4.1: Compounds features in this work: the backbone is 1,4-bis(phenylethynyl)benzene, and the terminating groups can be amine (-NH₂), trimethylsilylethynyl (-C≡CSiMe₃), triisopropylsilylethynyl (-C≡CSiMePr₃ⁱ) or *tert*-butylethynyl (-C≡CCMe₃)

ature using two distinct techniques, namely: the in situ break-junction (BJ) [141] and the $I(s)$ technique [142]. The molecules are deposited onto a gold surface forming a SAM, and then the conductance is measured employing a STM, with different set-up for each technique. The results obtained in such experiments, as well as the previously reported, are the main motivation behind the work which are going to be exposed in this chapter. So, It will be presented a single molecule conductance study of a small series of amine, trimethylsilylethynyl, triisopropylsilylethynyl and *tert*-butylethynyl contacted 1,4-bis(phenylethynyl)benzene molecules (Figure 4.1) between gold electrodes grown along the (111) crystallographic direction, focusing above all, in compounds 1, 2 and 3 in figure 4.1. Firstly, the computational method including an explanation of the theoretical set-up to simulate room temperature measurements as well as the method to calculate transport properties, will be presented. Then, the transmission properties and conductance histograms calculated will be depicted and discussed; the comparison with experimental results will also be provided. It will allow to draw an unambiguous correlation between each of these groups and the number of observed conductance peaks, with special attention to C≡CSiMe₃ group.

4.2 Computational Method: theoretical set-up to simulate room temperature measurements and transport calculations

The relevant experiments measure the conductance of a SAM made by the target molecule using a STM. Each of the target molecules could bind to Au(111) surfaces via a variety of atomic arrangements and if the energy of every possible contact between a given compound and the surface were to be computed, an energy manifold with many local minima separated by low, medium and high energy barriers would be found. At room temperature, It should be expected that many of these minima will be visited in a typical duration of an experiment. To reproduced such an experimental situation, four different initial configurations were explored using ab-initio molecular dynamics (MD) at room temperature for each of the compounds **1-3** in figure 4.1. The initial configurations are shown in figure 4.2. A pyramid-shaped array of gold atoms and gold slab was employed as the top part of the junction, as a representative model of the STM tip. However, as two extremes It has been used either a flat surface or a pyramid at the bottom part of the junction to simulate molecule binding to the substrate either at a terrace (a flat surface region) or alongside a stepped pyramidal structure (which is in effective a rougher surface). In all cases, the pyramids are built from 3 layers of gold atoms. The difference between configurations **1-2** and **3-4**, is that in former case, the pyramid is placed on top of the molecule, and in the latter case is placed aside of the molecule. To sum up, different combinations of electrode surface models include either only one pyramid at the top electrode and a flat surface on the bottom contact or gold pyramids on both the top and bottom electrodes. These junction configurations lead to different chemical bonding arrangements for each of three compounds through the two different contact groups (-NH₂ and/or -C≡CSiMe₃).

The electronic structure calculations and MD were performed using SIESTA. In the Linear Combination of Atomic Orbitals was used a single- ζ polarized (SZP) basis set which explicitly included the *s*, *d* and diffuse orbitals for the gold atoms at the electrodes. The choice of a simpler basis set for gold dramatically decreases the execution time of the simulations and gives results similar to those obtained with more involved basis sets. It was indeed checked that the transmission of the studied molecules calculated with SZP+diffuse orbitals on the electrodes was qualitatively similar and gave the same transmission at the Fermi level as that obtained with DZP on the electrodes (figure 4.3). However, It was found that, in order to accurately determine the charge transfer between the electrodes and the molecule the DZP basis on the electrodes must be included. DZP was therefore

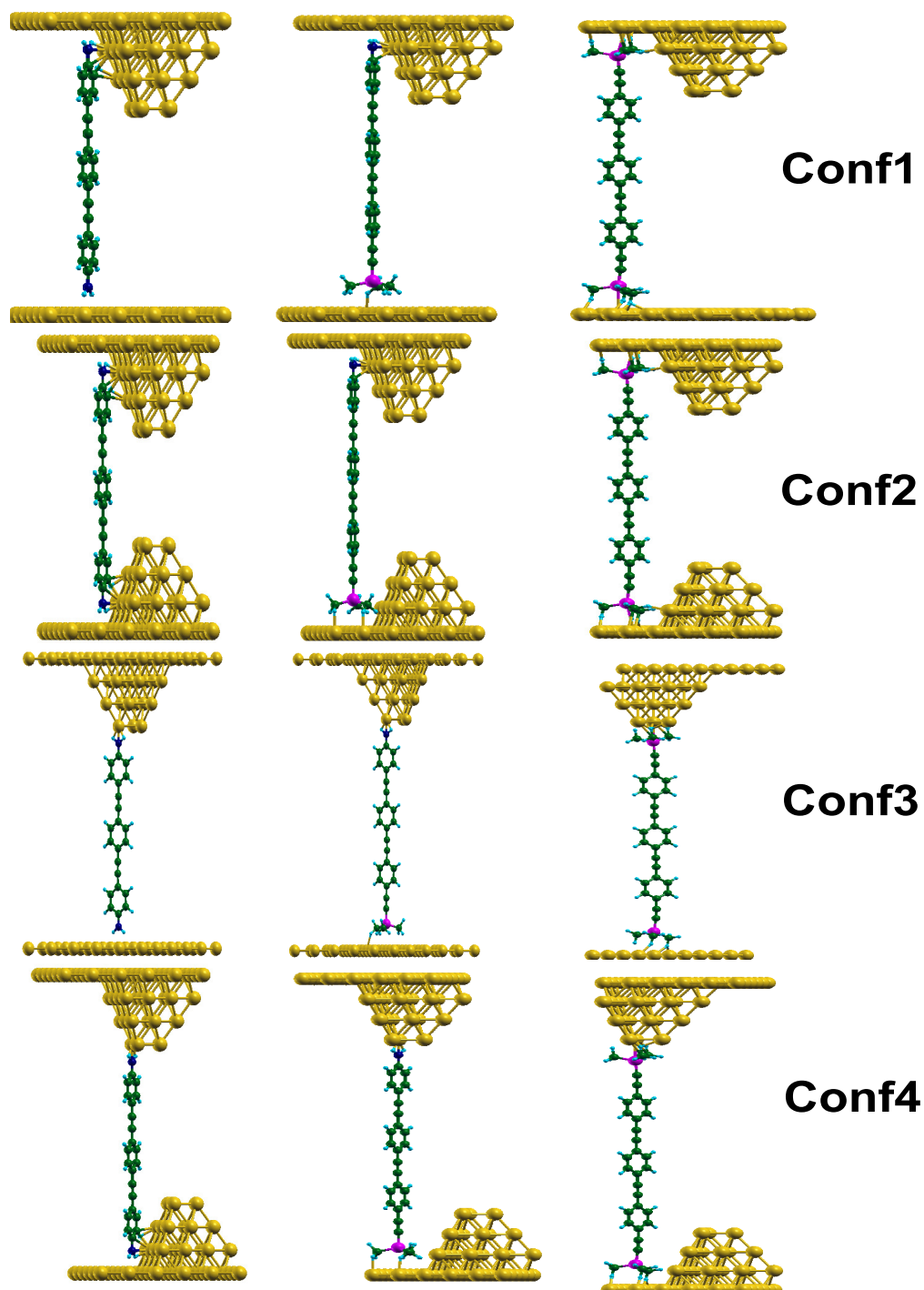


Figure 4.2: the four configurations (Conf) used to start the ab-initio molecular dynamics simulations of each junction for compounds **1**, **2** and **3** (left, middle and right columns, respectively). Blue, green, dark blue, magenta and yellow represents hydrogen, carbon, nitrogen, silicon and gold respectively.

necessary to correctly describe the bonding nature between the molecule and the electrodes. A double- ζ polarized (DZP) basis set was used for all elements in the molecule (H, C, N and Si). The density, the potential, the Hamiltonian and the overlap matrix elements were represented in a real space grid defined with an energy cutoff of 200 Ry. For the exchange and correlation potential was used the local density approximation (LDA) as parametrized by Ceperley and Adler [72]. The molecular coordinates in the gas phase were relaxed until all forces were smaller than 0.05 eV/Å. The molecules were then placed between the surfaces. The MD was performed on each configuration using a Nosé thermostat, with initial and target temperatures set to $T = 300$ K, and where the distance d between the two surfaces was kept fixed but gold atoms within the gold pyramids as well as the atoms in the molecule, were allowed to move freely on each MD step. Note that DFT computations of molecular conductance usually involve generation of transmission curves for a single relaxed molecular junction configuration. However, the numerical values of the computed conductance can have a strong dependence on fine details of the junction geometry, such as the nitrogen-gold or silicon-gold distances for example, which vary as the MD simulations proceed. A different approach was therefore pursued here, and by computing over a relatively large number of MD generated configurations and generating theoretical conductance histograms such junction-to-junction variations can be included in the computational result for better comparison to experiment. So, for each configuration 300 molecular dynamics steps, with time step length of 1 fs were allowed. The conductance was calculated every 10 steps and the resulting values organized to construct a theoretical conductance histogram. As a consequence, each histogram contains about 120 conductance values.

The transport calculations (transmission coefficients and conductance) were performed using GOLLUM code (section 2.4.1). So, the junctions were divided in three parts: left and right leads and a scattering region (named *extended molecule* (EM)). The leads are made of bulk gold electrodes grown along the (111) crystallographic direction. It has been picked as Principal Layer in the leads a cell containing three atomic layers of 6x6 atoms each. It has been chosen for the scattering region a cell containing the central part of the junction: the surface region of the electrodes and attached to them, one of the molecules under consideration. It has been chosen for the surface of each gold (111) electrode five atomic layers consisting of 6x6 atoms each. By doing so, It is sure a smooth matching of the leads and the scattering region Hamiltonian. It has been used the Γ point (1 k point) along the plane perpendicular to the transport direction, which in the case of gold is enough to achieve convergence. Finally, to correct for the deficient molecular HOMO and LUMO energy positioning and their gap predicted by DFT, It

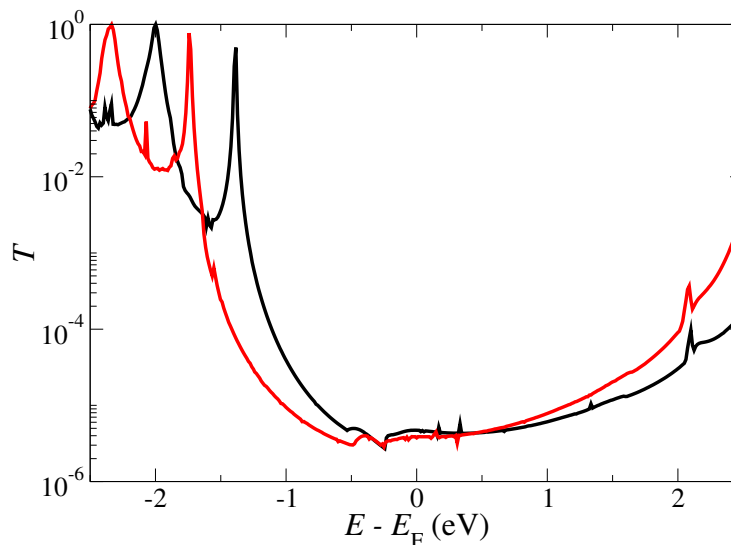


Figure 4.3: transmission coefficients for a MD step in configuration 2 and TMSE system (Conf2 and right column in figure 4.1) calculated using SZP+DiffuseOrbitals (black line) and DZP (red line) as a basis for gold. Note that at Fermi level, the transmission is very similar

has been included the phenomenological spectral adjustment explained in section 2.4.1.

4.3 Theoretical Results

4.3.1 System's geometry: How the molecules are bonded to gold electrodes?

The origin of the low variability produced by $-C\equiv C\text{SiMe}_3$ group (the observation of only a L-conductance group) is proposed to be due to the presence of $-CH_3$ groups, which limit steric access of the TMSE group to the surface and hence promote a single L conductance feature. In order to test this hypothesis, initial simulation of idealized top, bridge and hollow configurations of molecules with $-NH_2$ or $-C\equiv C\text{SiMe}_3$ groups between flat (terrace) gold surfaces were performed. So as to do this initial calculation, the equilibrium distance to gold surface in top, hollow and bridge position (namely, the lowest energy position) was studied. The molecule with $-NH_2$ or $-C\equiv C\text{SiMe}_3$ groups was placed onto a gold surface on top, hollow or bridge, varying the perpendicular distance to the surface. In each location, a relaxation of the coordinates in $-CH_3$ or $-NH_2$ groups were allowed. Finally, using the geometry at the equilibrium distance the transmission was calculated. It can be seen in figure 4.4 the result obtained. The values of the conductance (transmission at Fermi level) differ little across the range of binding configurations

for the TMSE group (figure 4.4(b)). However, for the $-\text{NH}_2$ group the conductance is very similar for the bridge and hollow configurations (black and red curves, respectively, in figure 4.4(a)) but it is one order of magnitude smaller for the top configuration (blue curve). The differences in conductance for the $-\text{NH}_2$ group are mainly due to the dissimilar equilibrium distance for bridge and hollow (2.8 Å) comparing with top (3.2 Å) unlike $-\text{C}\equiv\text{CSiMe}_3$ group where all distances are equal (4.0 Å)¹. This shows that at least on flat terraces the TMSE group reduces the variability of the conductance measurements.

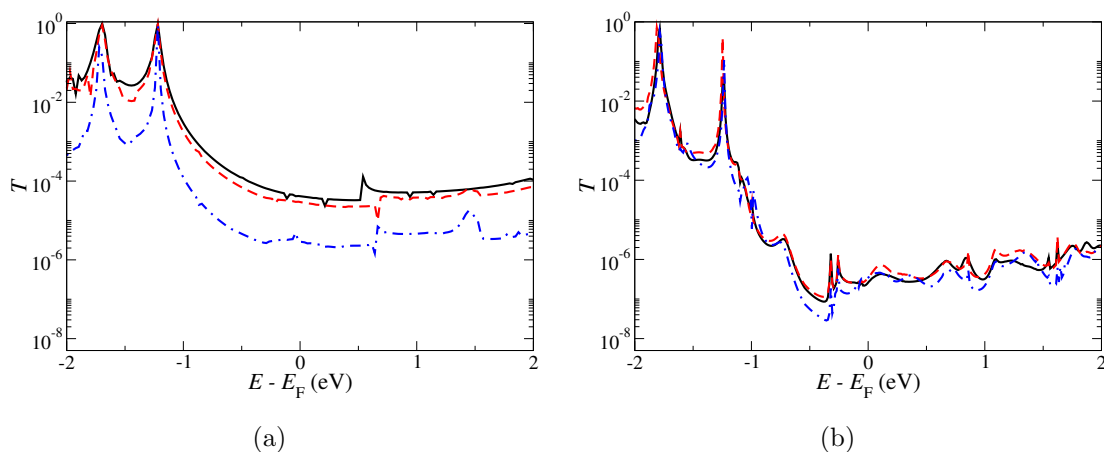


Figure 4.4: Transmission coefficients for molecules with both anchor groups being (a) $-\text{NH}_2$ and (b) $-\text{C}\equiv\text{CSiMe}_3$, calculated between flat gold surfaces, in bridge (black curve), hollow (red curve) and top (blue curve) configurations at equilibrium distance

The room-temperature MD simulations point out that in some conformations, the amine anchor group in compounds **1** and **2** binds to the pyramid-like electrode features either through the $-\text{NH}_2$ group, via a π -type interaction with the associated phenyl ring, or through both at the same time. Similarly, compound **1** also binds to the terrace regions on the bottom electrode only via the $-\text{NH}_2$ group. Nevertheless, as noted above, the terrace sites offer multiple different contact geometries, with the $-\text{NH}_2$ group able to bind to a top, a hollow or a bridge gold site, each of which leads to a different conductance value. The $-\text{NH}_2$ results are thus consistent with a broad conductance distribution or multiple conductance groups.

The TMSE groups in **2** and **3** also bind to the gold atoms at the bottom electrode in several different ways. When the bottom electrode is a terrace, the TMSE group binds weakly via the methyl groups to the surface. These groups remain quite inert and keep the silicon relatively far away from the surface. There is no

¹The equilibrium distances which are shown here, indicate perpendicular distance between N (in $-\text{NH}_2$ group) or Si (in $-\text{C}\equiv\text{CSiMe}_3$ group) and gold surface.

significant rearrangements of the local silicon geometry. The tetrahedral geometry at silicon and positioning of the methyl groups in contact with the surface results in the silicon atom being displaced from the surface, at distances greater than 3.5 Å, and thereby interacting weakly with the Au surface atoms. This long Si-gold distance gives rise to a decrease in the conductance and to a reduction in the conductance dispersion. In order to gain a first insight into the nature of the chemical bonds and check how stable are the junctions, the binding energies for configurations where the TMSE groups of compound **3** molecules lie in the hollow, top and bridge positions of a flat gold surface were computed. These binding energies are compiled in table 4.1. The first thing that can be said according to the binding energy results is that all energies are greater than kT at room temperature. So, simple estimates based on the Arrhenius law indicate long stability times. For these systems the hollow site appears as the most stable configuration. In simulations where the bottom electrode features a pyramid (figure 4.2, Conf. 2 and Conf. 4) the binding energies are increased by about 150 meV, suggesting that compound **3** will preferably place itself at irregularities of the surface such as steps rather than in the middle of the terraces. These findings are in excellent agreement with the data obtained by Fichou *et al.* from SAMs of TMSE functionalised unsaturated hydrocarbons on flat gold substrates [143]. The high binding energy calculated is consistent with the stability of the films and the evidence of pit-etching. However, in contrast to the initial proposals, a local five-coordinate silicon complex, the calculations here indicate a more subtle molecule substrate interaction.

Table 4.1: Binding energies of a single $-\text{C}\equiv\text{CSiMe}_3$ group of compound **3** for different positions and configurations. The surface+pyramid configuration corresponds to cases that model the L-conductance group. The group is considered as either binding to a "terrace surface" at either hollow, top or bridge sites, or at a "surface + pyramid" contact (e.g. as illustrated in figure 4.2. right column, Conf. 1, top contact).

Configuration	Hollow	Top	Bridge
Terrace Surface	0.59 eV	0.40 eV	0.45 eV
Surface + Pyramid	0.74 eV	0.61 eV	0.53 eV

To improve the knowledge about the nature of the molecule-surface interaction, the charge redistribution once the binding is done, has been estimated using Mulliken Population analysis. Whilst the silicon atom retains its four coordinate,

tetrahedral configuration, there is a charge transfer from the substrate to the molecule of 0.4-0.8 electrons, depending on the MD step. Most of this charge goes to the TMSE groups and is divided equally among them. Inside each group, the atoms that gain more charge are the hydrogens, which are the ones closer to the surface, whereas the C and Si do not gain too much charge ($\sim 0.1 e^-$ or less each).

A significant junction conductance with compound **3** is nearly always achieved for a rather specific configuration of the TMSE anchoring group. It happens when the molecule binds to a pyramid as depicted in Conf. 2 of figure 4.2. A closer inspection of the geometry junction shows that the $-C\equiv C\text{SiMe}_3$ group interacts with the flat terrace surface at the base of the pyramid and at the same time with the Au atoms on the pyramid. In this configuration the methyl groups are oriented so that the silicon atoms are as close as possible to the pyramid, i.e. the space between two methyl groups is directed towards the pyramid and close to it. Importantly, an analysis of Mulliken Population reveals a greater charge transfer than before between the molecule and the surface (the molecule gains ~ 0.8 - 0.9 electrons) and the binding energy increases (maximum binding energy in table 4.1). This charge transfer increases the ionic character of the bond between the molecule and the surface. However, in many cases the TMSE group does not interact with the pyramid, especially when the methyl groups are directed towards it, and these configurations do not produce a conductance peak in the theoretically-generated histograms (even at very low conductances). In such situations the charge transfer is bit smaller and the binding energy is lower and similar to that on a flat surface, which implies there is no bond between the molecule and the pyramid. In other words, the methyl groups hinder the silicon-pyramid attachment.

A top view of the $-C\equiv C\text{SiMe}_3$ group and the pyramid in the model of the L-conductance group is shown in figure 4.5(a). The top view of the Au pyramid is depicted along with the TMSE group directed in such a way to bring the Si atom to directly face it (in that figure the Au terrace underlying the Au pyramid is not shown). By contrast, figure 4.5(b) shows a configuration in which a methyl group rotates towards the pyramid and the Si atom away, producing an essentially non-conductive configuration. Notice that in the L-conductance group configuration (figure 4.5(a)) the space between methyl groups is directed towards a gold atom and the silicon is closer to the pyramid than in configuration of figure 4.5(b). Furthermore, It is found in all MD simulations that, due to the specific geometrical arrangements imposed on the position of the molecule with respect to the pyramid by the SiMe_3 group, the phenyl rings of the molecular backbone can not bind in π -fashion to the pyramid, as happened with the $-\text{NH}_2$ group.

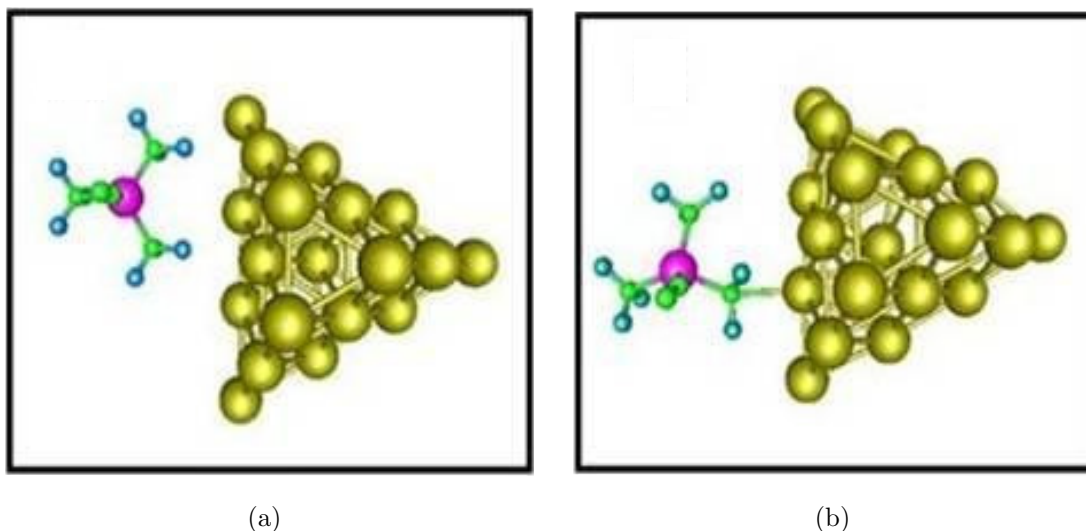


Figure 4.5: A top view of the relative $-\text{C}\equiv\text{CSiMe}_3$ group-pyramid arrangements. Blue, green, magenta and yellow atoms represent hydrogen, carbon, silicon and gold atoms, respectively. In order to make easier the visualization, only the gold atoms of the pyramid are shown and not the underlying gold terrace

To sum up, the steric hindrance provided by the methyl groups restricts the available binding energetics between TMSE groups of compounds **2** and **3** and the Au electrodes and the bonding between the TMSE group and flat terrace surfaces and single atom defects is relatively weak, van der Waals-type, with some ionic character. On the other hand the TMSE group can bind more strongly to the pyramid model surface, with a slightly larger degree of charge transfer leading to the stronger interactions, and stabilization of the junction through the resulting image charge. Thus, when the TMSE group is directed in such a way to allow the closest approach of the Si atoms to the pyramid, a significant binding energy is achieved and junction conductance which models the L-conductance group is obtained. The ionic character and image charge stabilisation plays an important role in the stability and conductance profiles of these structures. The steric bulk of the methyl groups prevents the close approach of the silicon atom and gold surface, and the resulting charge separated structures hold some analogy with molecular frustrated Lewis pairs [144].

4.3.2 Transport Properties

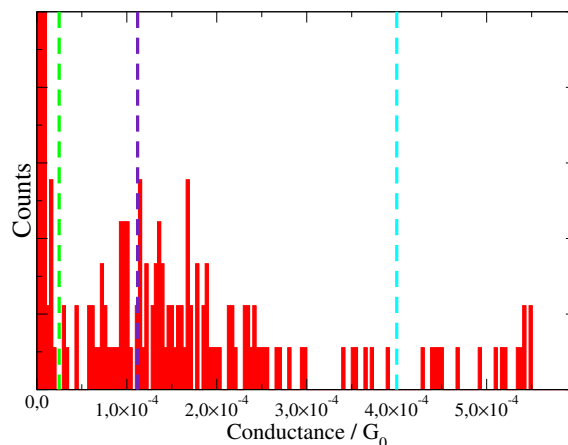
The theoretical conductance histograms for compounds **1**, **2** and **3** derived from the MD simulations are shown in figure 4.6. Note that each of the peaks contains

contributions from several atomic arrangements, which are classified according to their gross similarity to the initial snapshots shown in figure 4.2. A breakdown of these contributions is summarized in table 4.2. The statistics of the simulation data is limited by the computational cost of the simulations and are not as large as those obtained experimentally but in spite of this smaller statistics, the number of conductance peaks featuring in the calculated histograms agrees with experimental results, which are shown in figure 4.7, for each of the three compounds: three, two and one conductance peaks for compounds **1**, **2** and **3**, respectively (table 4.2). The poorer statistics results in a third conductance peak in figure 4.6(a), being under-developed, although a number of configurations give rise to conductance values which cluster close to the experimental H group value. It should also be noted that for the computational data represented in figure 4.6 there is an uncertainty in the choice of bin size which is most suited for generating the histogram. Nevertheless, the theoretical and experimental position of the conductance peaks agrees quantitatively for compound **1**.

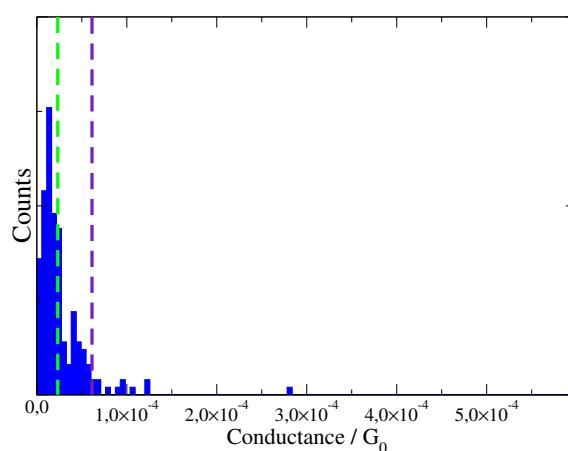
Table 4.2: relative contribution of each of the four configurations shown in figure 4.2 to the conductance peaks shown in figure 4.6.

Compound	L-Group	M-Group	H-Group
1	Conf. 1 (~60%)	Conf. 1 (~20%)	Conf. 1 (~33%)
		Conf. 2 (~20%)	Conf. 2 (~42%)
	Conf. 3 (~40%)	Conf. 3 (~30%)	Conf. 3 (~8%)
		Conf. 4 (~30%)	Conf. 4 (~17%)
2	Conf. 1 (~27%)	Conf. 1 (~55%)	
	Conf. 2 (~21%)	Conf. 2 (~42%)	
	Conf. 3 (~44%)		
	Conf. 4 (~8%)	Conf. 3 (~3%)	
3	Conf. 1 (~21%)		
	Conf. 2 (~70%)		
	Conf. 3 (~9%)		

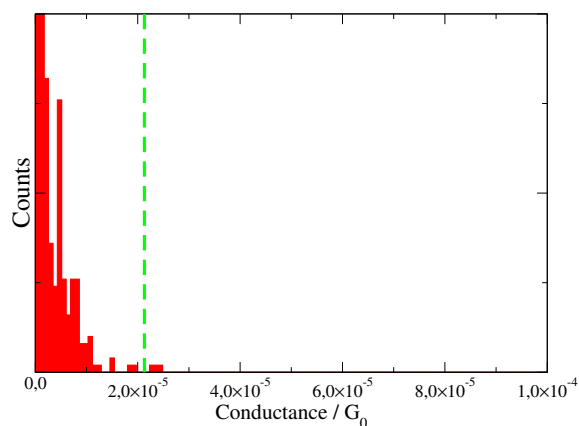
The two theoretical histogram peaks shown in figure 4.6 for compound **2** are slightly shifted towards smaller values with respect to the experimental peaks. This may be due to a slightly incorrect placement of the Fermi level with respect to the HOMO and LUMO orbitals. For compound **3**, only those junctions in which the TMSE group adopts the special position shown in figure 4.5(a) contribute to the single conductance peak shown in figure 4.6(c). Any other configuration yields



(a)



(b)



(c)

Figure 4.6: Conductance histograms of (a) compound **1**, (b) compound **2** and (c) compound **3**. Vertical dashed lines correspond to the experimental values (e.g. three conductance groups for **1**, two conductance groups for **2** and one conductance group for **3**

conductance values below 10^7 - 10^8 G_0 . The larger disagreement between the experimental value and the theoretically-generated conductance peak for **3** is due to

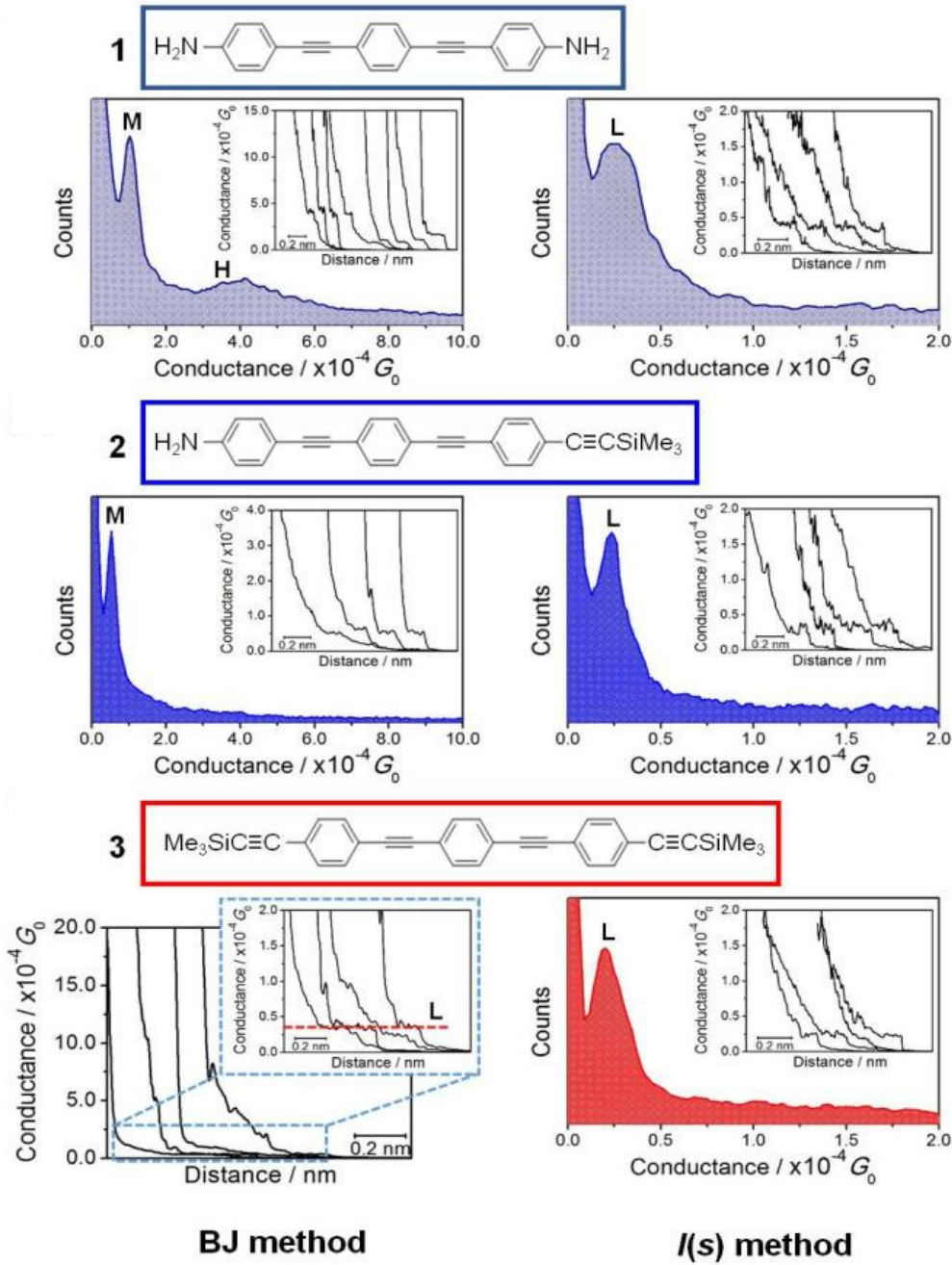


Figure 4.7: Experimental conductance histograms for the three compounds, reproduced from [140]

the rather small values produced from the simulated junction configuration.

In order to gain further understanding on the mechanisms that give rise to each conductance group the transmission coefficient $T(E)$ as a function of energy corresponding to a representative data point in each group (L,M,H) is plotted in figure 4.8. The low-voltage conductance is estimated as $T(E_F)$, where E_F is the Fermi energy. The Fermi level falls roughly in the middle of the HOMO-LUMO gap in all cases, which means that the junctions fall in the tunneling regime. In these transmission curves, peaks at negative energies to the left of the gap correspond to HOMO resonances, while peaks on the right of the gap, at positive energy values, correspond to LUMO resonances.

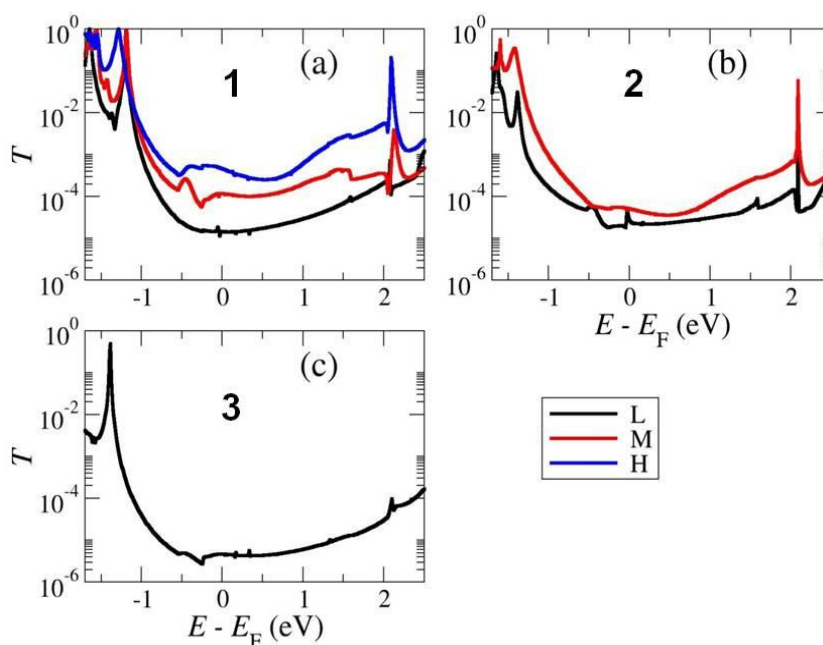


Figure 4.8: Transmission as a function of energy for a junction comprising (a) compound **1**, (b) compound **2** and (c) compound **3** on a gold surface with pyramids

In the case of **1**, enhancement of the conductance from the L to the M and to the H groups is due to an increase of the transmission in the gap, which in turn originates from an increase of the width of the HOMO resonance, while the energy position of the HOMO level itself remains constant. These width changes come from changes in the hybridization between the HOMO orbitals and the surface gold atoms. Note that, according to the local density of states (LDOS), the HOMO in all these molecules is spread roughly through the whole molecule and is affected by the interaction with the electrodes, in contrast to earlier assumptions.

In the transmission curve for **3** (figure 4.6(c)), the arrangement shown in figure 4.5(a) corresponds to the L group observed in the experimental measurements. Although this is labeled as a "low" contact configuration in the analysis of experimental results (see figure 4.7, compound **3**), the conductance of this junction is higher than other cases observed in the MD simulations of this compound. The higher relative conductance for this arrangement versus other junction geometries comes from a competition between two factors. The first is that the resonance width increases from 5 meV to 8 meV, which enhances the conductance of the junction and can be traced back to a larger molecular orbital-electrode hybridization. In contrast, the second is a shift of the HOMO transmission resonance to lower (more negative) energies, which serves to decrease the junction conductance. On balance, the shift in the HOMO resonance cannot compensate for the increased molecule-surface interactions, and as a consequence the conductance increases.

Transmission curves for junctions formed from compounds **4** (with triisopropylsilylethynyl, $-\text{C}\equiv\text{CSiMePr}_3^i$, anchor groups) and **5** (*tert*-butylethynyl, $-\text{C}\equiv\text{CCMe}_3$, anchor groups) were also calculated. Figure 4.9 compares the transmission of triisopropylsilylethynyl contacted **4** and trimethylsilylethynyl contacted **3** on a flat surface and demonstrates the conductance is much smaller for **4**. This further confirms that the use of the very bulky isopropyl groups leads to very low or no observable conductance. Various configurations for compound **5** starting from configurations similar to those that gave the L group for **3** were also explored. Although the transmission curves from **5** resembled those of **3**, the conductance at the Fermi level was 2-3 times smaller. This low conductance indicates that the *tert*-butylethynyl group is unlikely to produce junction with significant conductances in agreement with the experimental observation.

4.4 Remarks

It has been shown here that trimethylsilylethynyl moiety, $-\text{C}\equiv\text{CSiMe}_3$, provides a means to control the range of conductive molecule-metal contacts. Thus, whilst the TMSE molecules can form weak van der Waals-type contacts with some ionic character on terraces at top, bridge and hollow sites, the conductance of these configurations is lower than the detection limits of the experiments. Rather, in stark contrast to the initial models, contacts at defect sites within a very narrow range of molecular orientations are necessary to allow an increase of the binding energy between the TMSE groups and the gold atoms. This enhanced interaction serves to stabilize the binding of the molecule to the surface through overlaps and a

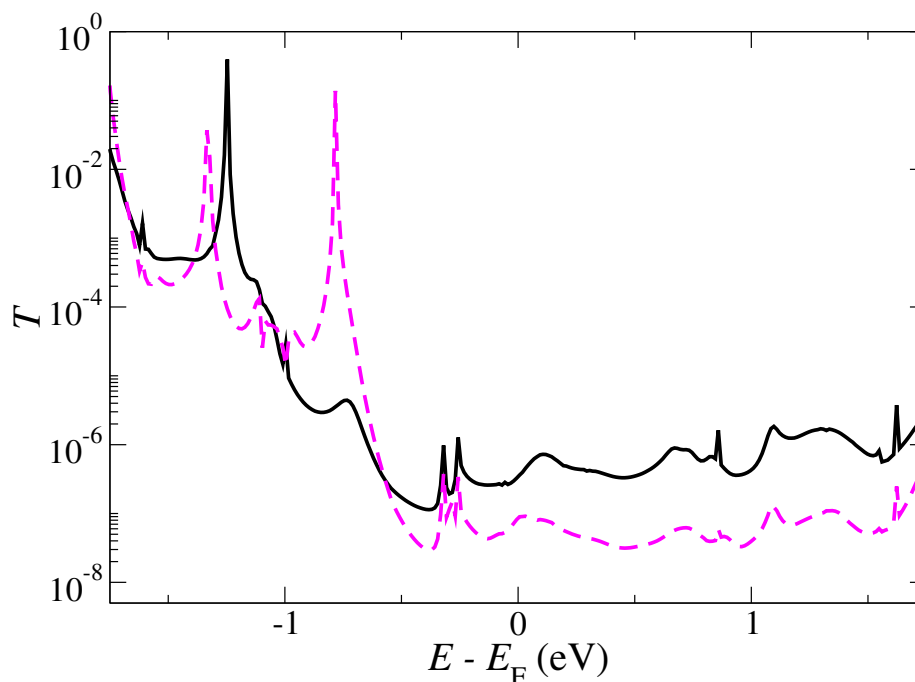


Figure 4.9: Transmission as a function of energy for a junction comprising **3** and **4** (solid black and magenta dashed lines, respectively) on a flat gold surface (without pyramids), calculated at the equilibrium distances (4.0 Å and 5.0 Å from the Si atom to the surface for **3** and **4** respectively).

image charge or electrostatic model. The net effect on the molecular conductance comes from the hybridization between the molecular levels and the gold atoms, which increases the width of the resonances (from 5 meV to 8 meV) and overall enhances the transmission at the Fermi level.

The very specific molecular orientation necessary for achieving significant molecular conductance results in a single low conductance peak for the TMSE-terminated compound **3**, which contrasts to the multiple conductance features of the amine terminated group **1**. The single conductance feature observed with $-\text{C}\equiv\text{CSiMe}_3$ terminated group is similar to conductance values from the L-type contacts on gold substrates with amine anchor groups. In this respect, **the $-\text{C}\equiv\text{CSiMe}_3$ group is a promising, but low conductance, contact group in fundamental studies of molecular junctions.**

Single-molecule Diodes with Asymmetric Molecules

5.1 General Introduction

In the framework of electronics, one of the most important elements in the heart of a circuit is the diode. A diode is a two-terminal electronic component which allows the current to flow appreciably only in one direction. So, this unidirectional behaviour when a current pass through a diode is used to convert an AC current into a DC current. This effect is called *rectification*, and is the most important functionality that diodes offer. Rectifiers are the most fundamental components employed for logic circuits and memory cells. Also, diodes are used as main components in signal limiters, voltage regulators, switches, signal mixers or signal demodulators. Traditionally, diodes were comprised of metal electrodes in a chamber evacuated or filled with a pure elemental gas at low pressure but nowadays, in conventional electronics, most diodes are made with semiconductor materials such as silicon, germanium or selenium in a p-n junction arrangement.

As It was pointed out on the introduction of this thesis, the use of molecules as active elements in electronic devices is considered a desirable way to continue the miniaturization of the components in such devices. Thereby, the search for molecules capable to provide diode-type behaviour has become a primary goal in

molecular electronics. But, what is behind a molecular rectifier? Rectification in a molecular system is usually as a result of two main factors: intrinsic asymmetry within the molecule and/or asymmetric bonding between the molecules and the electrodes. There are several ways to provide this asymmetry to the system. On one hand, the use of asymmetric linker groups or two different electrode materials [145] have proved to give current rectification. On the other hand, intrinsic asymmetry inside the molecules can derive from a structural asymmetry [146] or it can be forced by adding dopants at specific parts of molecules [147, 148]. Finally, a combination of two factors can enhance the rectification performance [149].

To sum up, some kind of asymmetry must be present in the system, and that asymmetry produce basically two rectifying mechanisms: the donor- σ -acceptor mechanism, where the electron transport is through either inelastic [1] or elastic tunneling [150] and the asymmetric position of the molecular levels with respect to the Fermi level of the leads [151, 152]. In both mechanisms, the non-trivial potential profile through the molecule, namely, between the electrodes, make that the molecular states align at different voltage values whether the bias is positive or negative. As well as this electrostatic influence, another factor could affect to the states alignment: the population of the molecular levels might depend on the bias direction. The latest factor is expected to affect in most extent to systems with a poor coupling and large asymmetry in their couplings [153].

Since the first theoretical proposal for a molecular rectifier [1], many experiments, using different strategies, have successfully reported rectification in molecular systems. Nonetheless, in some cases the rectification ratio (ratio between forward and reverse current or vice versa) is very low (less than 10) as well as the conductance and in other, the devices need to operate at very high voltages (greater than 1 V). In these high voltage regimes the room-temperature stability of single-molecule junctions can become a limiting factor or the measurement may become irreproducible. The latest problem was already observed in the earliest experiments where the alignment of molecular orbitals with chemical potential of the electrodes under such a high bias causes the molecule to heat reducing the current after each measurement. Finally, it is worth noting that rectification behaviour is generally very sensitivity to the junction structure.

Recently, Latha Venkataraman *et al* [154] have shown that molecular junctions comprising symmetric molecules display rectification ratios as large as 200 at voltages relatively small (around 400 mV). Unlike the usual strategies, which used an asymmetric molecular backbones or an asymmetric molecule electrode linkers to

get the rectification or a combination of both, Venkataraman and colleges use a symmetric molecule embedded in a polar solvent, which means that the environment can play a key role in the rectification behaviour.

But, even though much effort has been devoted to this topic from the experimental side, showing amazing results, the rectifying features of molecular junctions are still not clear enough. In this chapter, a theoretical study of molecular rectifying systems are going to discuss. The systems are based on a promising experimental measurements which show high rectification ratios, conductances of the order of $10^{-2} - 10^{-3}G_0$ and nice reproducibility and stability.

The chapter is organized as follows: first, a simple model which shows rectification is presented and discussed. This is made from a pedagogical point of view. Next, the systems under study will depicted and explain, giving the motivation of that choice. After that, the theoretical results obtained are shown and discussed. Finally, some remarks and conclusions are given.

5.2 Simple Model

Beyond the donor- σ -acceptor mechanism, one of the simplest models which can lead to rectification was first proposed by Krzeminski *et al* [151] and lately develop by Williams, Bratkovski and collaborators [152, 155]. They claimed that using simpler molecules with some preferential characteristics, a rectification behaviour could appear. The model consists of one molecular state slightly above (lowest unoccupied molecular orbital, LUMO) or below (highest occupied molecular orbital, HOMO) to the Fermi level of the leads, isolated to the electrodes for asymmetric tunneling barriers. The molecular state is an electroactive unit, and the asymmetry in the potential profile due to the disimilar barriers will drive diode-type behaviour in such a system.

This molecular rectifier could be achieved with molecules made by five structural parts: the end groups which link the molecule to the leads, the insulators and the conductor part. Such a construction is thought to provide a localized level in the conductor part, isolated from the electrodes. In most cases, the localized level will be the LUMO of the molecule, hence the transmission probability should be resonant close to the energy of the LUMO. A picture of the schematic structure for the molecular rectifier proposed can be seen in the figure 5.1



Figure 5.1: Schematic structure of an asymmetric tunneling barrier molecular rectifier.

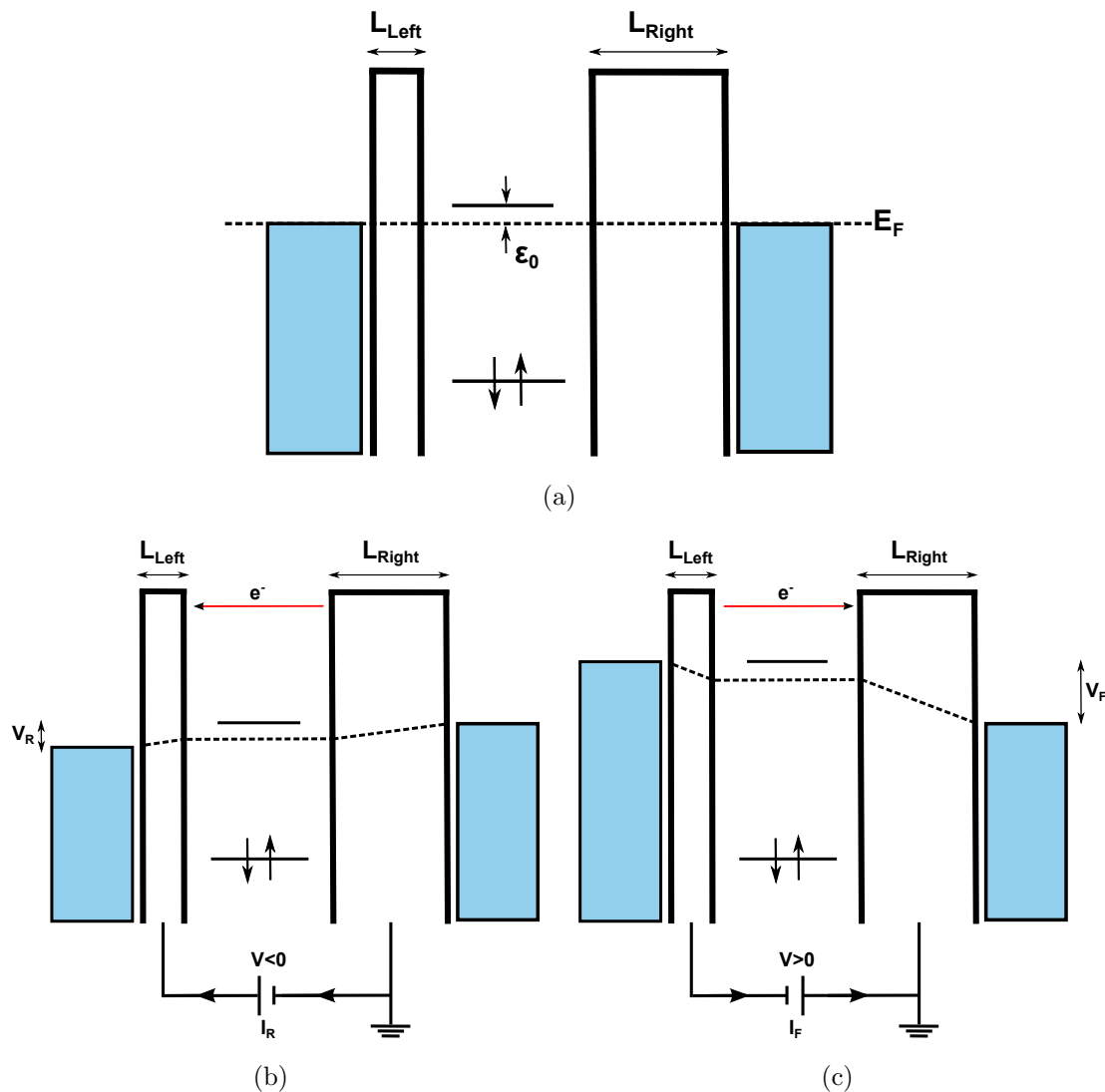


Figure 5.2: the basic principle of rectification by asymmetric tunneling barriers. In (a) ϵ_0 is the energy difference between the LUMO and the Fermi Level. In (b) a negative bias is applied; the current rises when the molecular state aligns with the right Fermi level at V_R . In (c), positive bias is applied, and the current rises when the molecular state aligns with left Fermi level at V_F .

The principle of the molecular rectifier is sketched in figure 5.2. There are two main parameters which define the rectification features of the molecular rectifier: the energy difference between the LUMO and the Fermi energy of the electrodes at equilibrium (named ϵ_0 in figure 5.2(a)) and the ratio of the voltage drops on the right and left insulating compounds named η . The model assumes that due to the larger polarizability of the conductor compound, the voltage drop is mostly

produced on the insulating parts and it is proportional to their respective lengths, hence $\eta \approx L_{Right}/L_{Left}$. Employing the convention that the right electrode is grounded, its Fermi energy can be used as the reference energy. So, when a positive potential is applied to the left electrode, the states of that electrode shifts to lower absolute energies. Thus, under negative bias, the Fermi energy of the left electrode goes down. Because of the non-zero electric field between the leads, the LUMO will be dragged down too, and the energy shift of that ΔE_{LUMO} is determined by the parameter η . Under the assumptions made before, the potential drop on the two insulating barriers have to sum up the total external potential $U_{Right} + U_{Left} = V$, where

$$U_{Right} = \left(\frac{\eta}{1+\eta}\right)V \quad , \quad U_{Left} = \frac{V}{1+\eta} \quad (5.1)$$

Then, it can be shown that:

$$\Delta E_{LUMO} = \frac{\eta}{1+\eta}qV \quad , \quad V < 0 \quad (5.2)$$

So, in the resonant condition, which means $\Delta E_{LUMO} = \epsilon_0$, the corresponding reverse voltage will be:

$$V_R = \frac{1+\eta}{\eta} \frac{\epsilon_0}{q} \quad (5.3)$$

When a negative voltage is applied to the left electrode, both the left Fermi energy and the LUMO go up in energy. So, for positive bias, ΔE_{LUMO} will be:

$$\Delta E_{LUMO} = \frac{qV}{1+\eta} \quad , \quad V > 0 \quad (5.4)$$

and hence, in the resonant condition the forward bias is:

$$V_F = (1+\eta) \frac{\epsilon_0}{q} \quad (5.5)$$

From the above equations, it is clear that there is a difference between the forward and reverse voltages, their ratio being $\eta = V_F/V_R$. Then, a notable difference between forward and reverse current will be observed in the voltage range $V_R < |V| < V_F$. The main transport features can be qualitatively explained using a model of resonant tunneling through a localized state in the barrier. The current can be written as:

$$I = \frac{2q}{h} \int dE [f(E - \frac{qV}{2}) - f(E + \frac{qV}{2})] T(E, V) \quad (5.6)$$

where the transmission $T(E)$ at zero temperature is given by (including both spin directions):

$$T(E, V) = \frac{\Gamma_L \Gamma_R}{(E - \epsilon)^2 + \frac{1}{4}(\Gamma_L + \Gamma_R)^2} \quad (5.7)$$

being ϵ the energy of the molecular orbital, which is given by:

$$\epsilon = \epsilon_0 + \frac{\eta}{1 + \eta} qV \quad (5.8)$$

and Γ_i the couplings between the state and left and right electrodes. It is known that $\Gamma_i \propto e^{-2\kappa_i L_i}$, and by cause of this $I \propto e^{-2\kappa L_>}$, where $L_>$ is the length of the largest tunneling barrier. So, It has been shown that the asymmetry in this rectification mechanism is controlled by the largest length. In addition, a good isolation is mandatory to have small broad of the level involved. Nevertheless, the current fall off exponentially with the length of tunneling barriers. So, all this things must be taken into account to achieve a nice molecular rectifier.

In order to gain insight into the rectification mechanism explained before, a simple first-principles calculation has been performed. On it, two gold chains are bridged by a sodium atom. The calculation were carried out using the nonequilibrium Green's function code SMEAGOL (for more details, see section 2.4.2). That code compute the electronic density matrix using DFT. It was utilized the local density approximation for the exchange and correlation energy and potential as parametrized by Perdew and Zunger (ref. CA). The density, the potential, the Hamiltonian and the overlap matrix elements were represented in a real space grid defined with an energy cutoff of 200 Ry. A single- ζ (SZ) basis set including only s states was chosen for both kind of atoms, gold and sodium. The idea was to do as simple as possible the calculations, in order to avoid misunderstandings in the interpretation of the results. A single transverse k -point was used when performing transport calculations. In figure 5.3 it can be seen the system. Each chain is built by six gold atoms separated each other 2.9 Å. The sodium atom has been placed 5.0 Å away from the first chain and 10 Å from the other. The sodium atom provides a single level, that will possible become a LUMO state as it is expected to donate its electron to the gold electrodes.

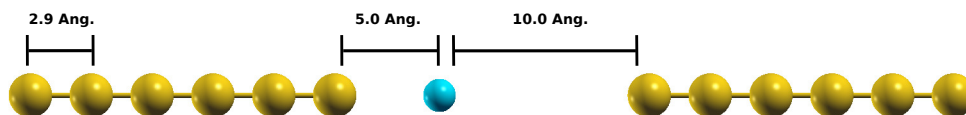


Figure 5.3: schematic view of the gold-sodium system. Yellow and blue represent gold and sodium respectively.

The I-V characteristics of the system are displayed in figure 5.4(a). It shows that for negative voltages, the current rises very quickly until around 0.3 V, and then reaches a plateau. However, for positive voltages, the current rises very slow, staying almost flat and smaller than for negative bias. The inverse of rectification ratio (RR), where the RR is defined as I_F/I_R , can be seen in figure 5.4(b). Notice that the maximum rectification is 10 at 0.37 V. This behaviour can be understood by studying the transmission coefficients of the system and the projected density of states (PDOS) onto the sodium atom, which are shown in figure 5.5 for some significant voltage values: -1.40 and -0.35 volts in figure 5.5(a), and 0.35 and 1.40 volts in figure 5.5(b). For the sake of comparison, the PDOS and transmission coefficients at zero voltage are shown in both figures. It follows that the PDOS at zero voltage indeed shows a single state at positive energies, confirming that the sodium state is a LUMO. The transmission curve shows a very wide resonance. This means that the junction is highly transparent.

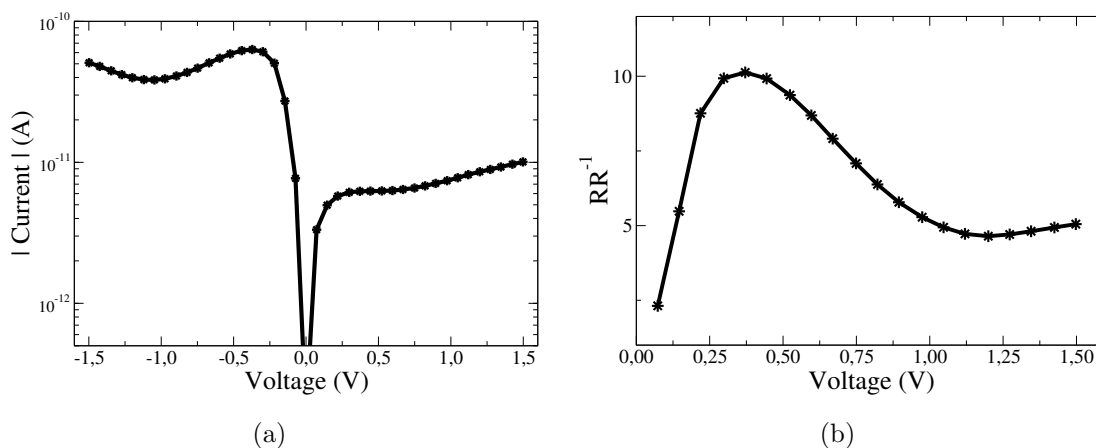


Figure 5.4: (a) I-V characteristics for the gold-sodium system, which shows an asymmetric behaviour. In the Y-axis, is represented the absolute of the current in amperes, and in the X-axis the bias voltage in volts and (b) RR for the system

For negative voltages, which means that a positive voltages is applied on the left electrode and their states shifts to lower energies, the LUMO is dragged to lower energies too, so the resonance enters quickly in the bias window and as con-

sequence, the current rises very fast. Nonetheless, for positive voltages, the LUMO moves to higher energies as the voltage rises, and the peak of the resonance stays always out of the bias window, in the voltage range studied. It is seen that the LUMO follows the left electrode. This is evident from the figure 5.6, where the sodium state energy versus bias voltage is represented. It is clear that that level, indeed, follows the chemical potential of the left electrode, and enters in the bias window for negative voltages quickly (green arrow in the figure). This happens due to the construction of the system and provides the rectification mechanism.

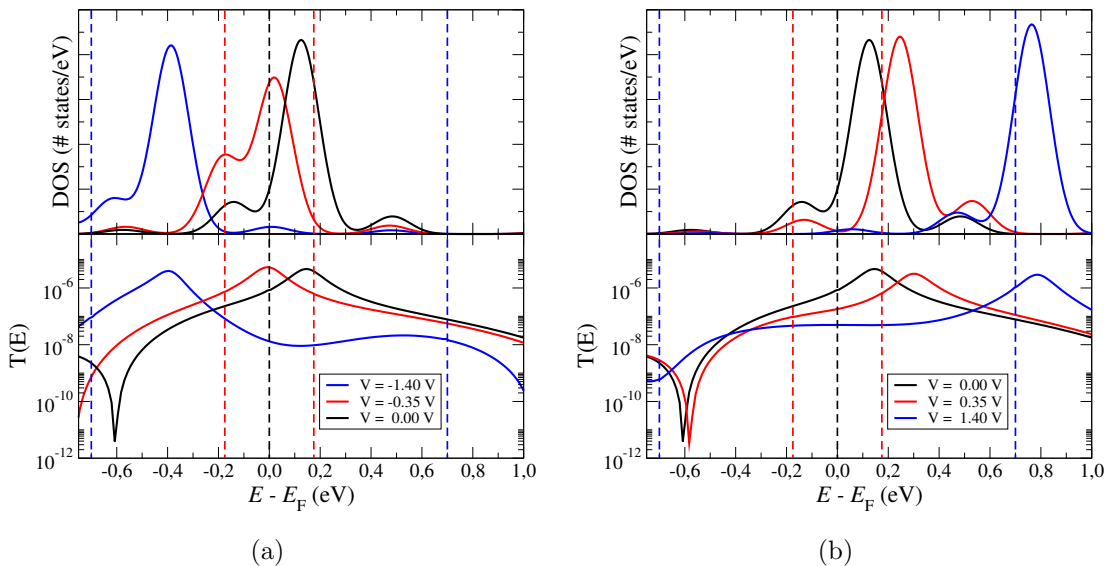


Figure 5.5: projected density of states onto sodium atom (PDOS) -top panel- and transmission coefficients -bottom -panel- for (a) -1.40 and -0.35 volts and (b) 0.35 and 1.40 volts. PDOS and transmission coefficients at zero voltage are shown in both. The zero of the energy is the Fermi level. Broken vertical lines represent the bias window when the voltage is changing.

The results shown for such a simple system, agrees with Williams' model. However, due to the oversimplified construction, η parameter can no longer be represented as in the assumption made before, and it does not correspond with the ratio of the tunneling lengths. A glimpse to the figure 5.6 confirms this point, because it is easy to see that the LUMO state is going to enter in the bias window for positive bias at some voltage greater than 1.5 V, which is a value much bigger than the voltage predicted by the recipe $\eta = V_F/V_R$, where $\eta \approx L_R/L_L = 2$ and $|V_R| \approx 0.17V$. Because of the poor isolation of the sodium atom, the potential drop can not be represented by that parameter. This can be seen in figure 5.7, where is plotted the voltage drop, *i.e.* the change in Hartree potential between the case of zero and finite bias, being the finite bias equal to -1.40 V. It follows that the voltage drop is concentrated between the last gold in right chain and the sodium atom.

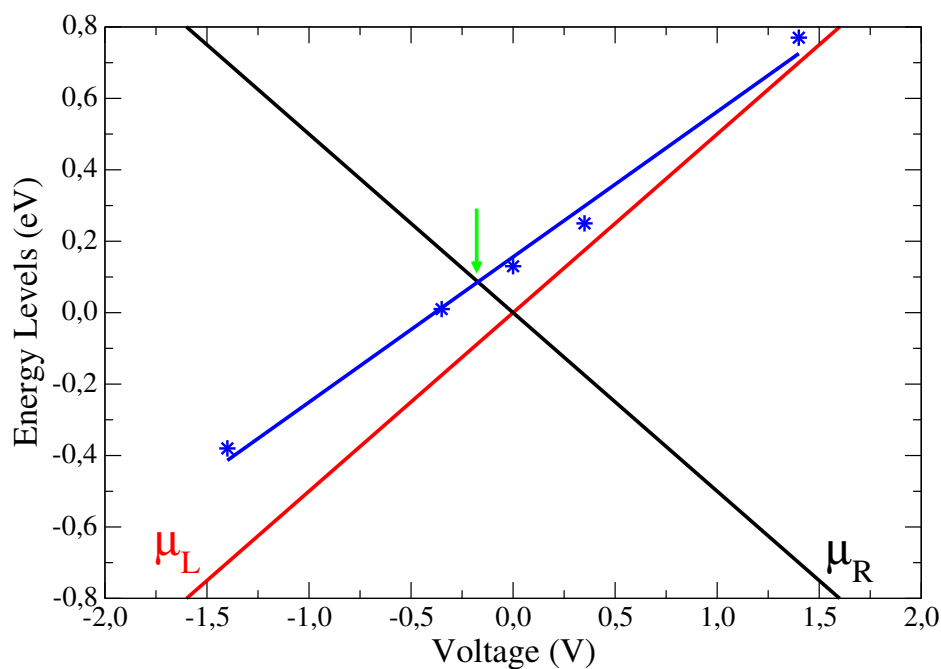


Figure 5.6: Energy of the sodium state (LUMO) versus bias voltage. Stars represent the energy extracted from the calculation and blue straight line its linear regression. Red and dark blue straight lines represent left and right chemical potentials respectively. Green arrow points out the voltage value where the state enters in the bias window.

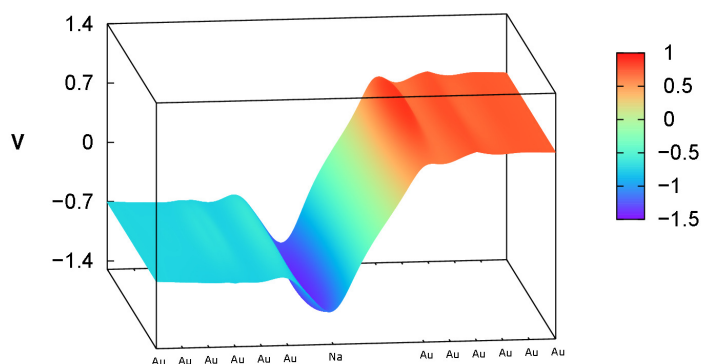


Figure 5.7: The voltage drop for an applied bias of -1.40 V, calculated in a plane going along the chain.

However, from a qualitatively point of view, knowing how the energy of sodium state changes with voltage, is easy to recover the previous recipe. Using the equation for the straight line in figure 5.6, it is obtained $V_F = 1.56V$ hence $\eta \approx 9.17$.

Now, choosing $\epsilon_0 = 0.15eV$, $\Gamma_L = 1.210^{-1}eV$ and $\Gamma_R = 1.210^{-7}eV$, the current can be calculated from (5.6) and (5.7), taking into account (5.8). The result is shown in figure 5.8.

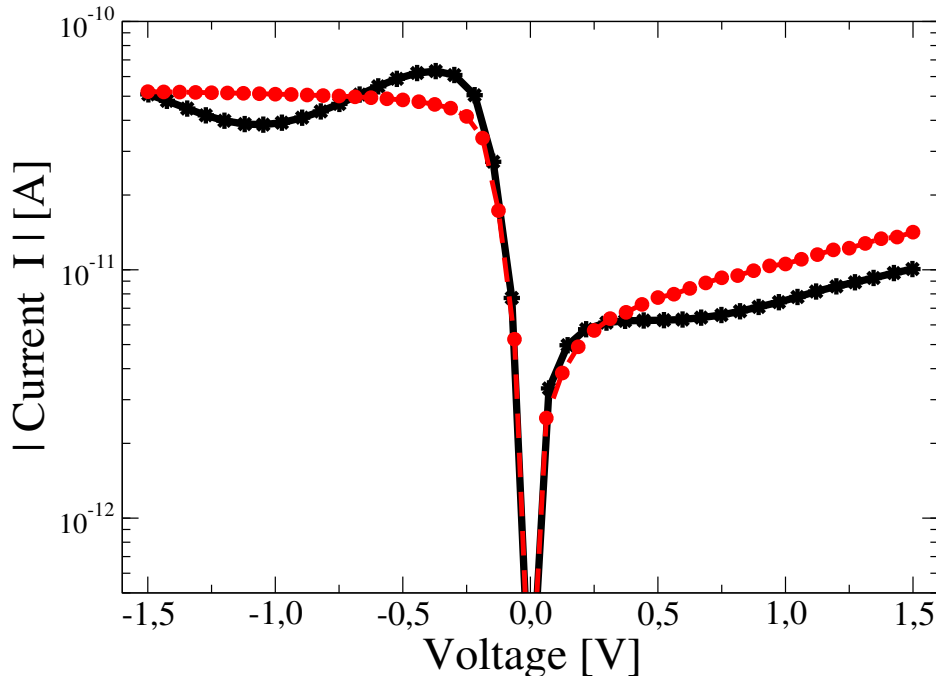


Figure 5.8: IV characteristics for the *Ab-Initio* calculation (black solid curve) and for the model of resonant tunneling (red dashed curve).

It shows that there is a nice agreement between *Ab-initio* calculations and the tunneling resonant model results, both qualitatively and quantitatively. So, It has been shown that such a mechanism like the presented here, having one isolated level slightly lower or higher to the Fermi level, could produce asymmetric IV characteristics, and therefore, diode-type features in molecular systems. In next sections, they will be shown results for more realistic systems, where the molecules belong to the MR family.

5.3 Searching for enhancing rectification ratios in single-molecule junctions

As it was indicated in latest section, in the fabrication of a nice molecule to implement the asymmetric tunneling barriers rectification mechanism into molecular electronic systems (see figure 5.1), there is a competition between the asymmetry of current onsets, which grows linearly with the asymmetry of the lengths and

therefore with the total length of the molecule, and the resistance of the molecule, which grows exponentially with its length. This is the typical trade-off problem.

There have been many proposals for the different parts of system 5.1, but one of the most popular uses thiols as anchor groups, saturated aliphatic chains $(\text{CH}_2)_n$ as insulators and a phenyl ring as central part. The molecules which are made by this pieces are named as the MR(m,n) family: $\text{HS}-(\text{CH}_2)_m-\text{C}_6\text{H}_4-(\text{CH}_2)_n-\text{SH}$. One molecule belonging to this family is sketched in the figure 5.9. It is thought that some of these MR molecules could achieve a good balance between rectification features and conduction. Because of this and the promising results that some experimental groups have reported recently (for example, the experimental group headed by Dr. Emanuel Loertscher from IBM and the experimental group headed by Dr. Florian von Wrochem from SONY Deutschland), here it is going to present a theoretical study of two MR molecules.

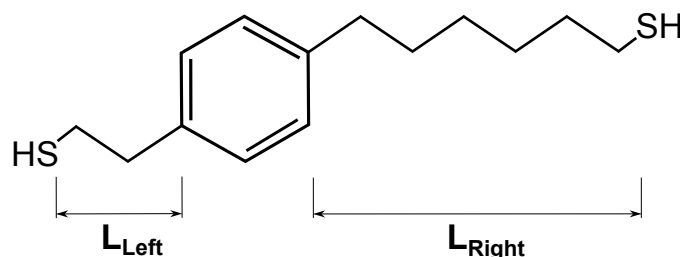


Figure 5.9: Schematic structure of the (2,6) member of the MR family.

The molecules under study are shown in figure 5.10. Both are MR(2,5), but with a small difference in their contacting groups. In the first case, figure 5.10(a), the end groups are dithiocarbamate group (DTC) in one side and a thiol group in the other side (named MR(2,5)-asymmetric). In second case, 5.10(b), both end groups are thiols (named MR(2,5)-symmetric). Such a construction produces in the first case, not only an asymmetry in the alkyl chains, but also in the contact groups and it is expected to give some differences in transport features comparing with the molecule with symmetric anchors.

5.3.1 Computational Details and System geometry

To simulate possible different experimental molecular junctions, several junction configurations has been explored utilizing the following scheme: as a first step, a coordinate relaxation in vacuum for each molecule was done. Next, the equilibrium

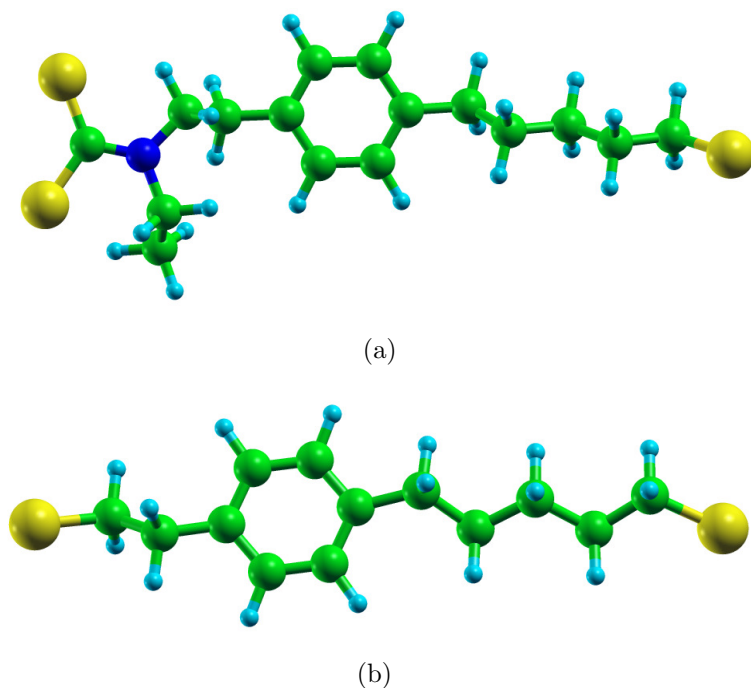


Figure 5.10: Molecules under study: MR(2,5) with (a) asymmetric and (b) symmetric anchoring groups. Molecules are shown as they would be in the contact configuration, namely, without final hydrogen atoms. Blue, green, dark blue and yellow represent hydrogen, carbon, nitrogen and sulphur respectively.

position of each anchoring group respect to the surface was calculated through a energy minimization, and is taken as the initial position. In figure 5.11 these initial positions with their corresponding distances between molecule and surfaces and between gold surfaces, are shown. Finally, the electrodes were opened (from here on, opening cycle, OC) and closed (from here on, closing cycle, CC) in steps of 0.4 \AA (0.2 at each side) allowing coordinates' relaxation in the molecule, calculating transport properties in for each step after the relaxation.

Geometry optimization was done using the DFT code SIESTA. Transport calculations were performed using the nonequilibrium Green's function code SMEAGOL. For the exchange and correlation potential was used the local density approximation as parametrized by Perdew and Zunger (CA referencia). The density, the potential, the Hamiltonian and the overlap matrix elements were represented in a real space grid defined with an energy cutoff of 200 Ry . A double- ζ polarized (DZP) basis set was chosen for all atoms in molecules both in the geometry optimization and transport calculations. For gold atoms either a double- ζ polarized (DZP) basis set including explicitly the s and d orbitals or single- ζ with only the s orbital in the valence was used in the geometry optimization and transport calculations respectively. In order to justify the latest simpler choice for gold, one calculation

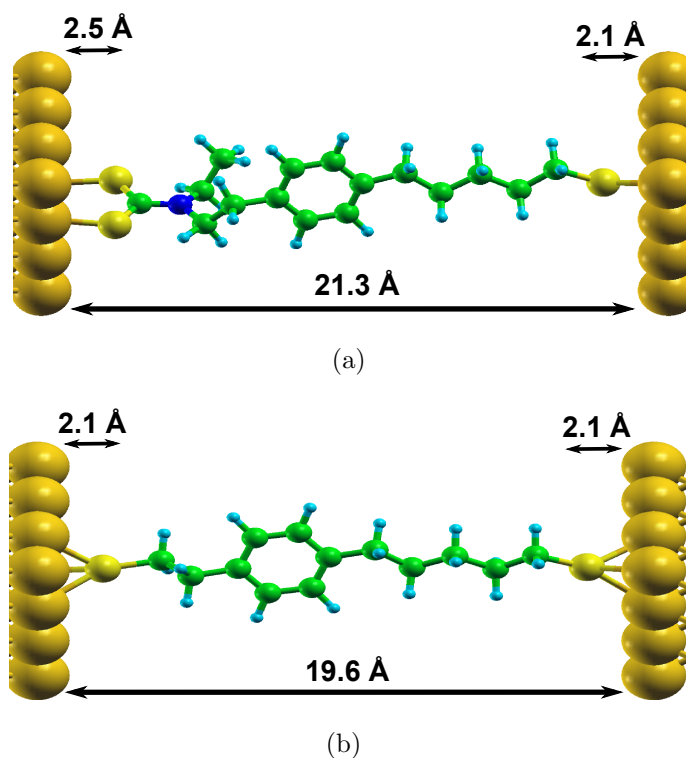


Figure 5.11: Initial positions after geometry optimization for MR(2,5) with (a) asymmetric or (b) symmetric anchoring groups. Blue, green, dark blue, yellow and dark yellow represent hydrogen, carbon, nitrogen, sulphur and gold respectively.

was done employing as a basis set single- ζ polarized (SZP) including explicitly s and d orbital, finding no significant change in the main transport results. A single transverse k -point was used when performing geometry and transport calculations. The coordinates was relaxed, employing a conjugated gradient scheme (CG), until all forces were smaller than $0.05 \text{ eV}/\text{\AA}$. For transport calculations, the junctions were divided in three parts: left and right leads and a scattering region. The leads are made of bulk gold electrodes grown along the (111) crystallographic direction. It was taken as Principal Layer in the leads a cell containing three atomic layers of 4×4 atoms each. In addition, it was chosen for the scattering region a cell containing the central part of the junction: the surface region of the electrodes and the molecule attached to them. It has been chosen for the surface of each gold (111) six atomic layers consisting of 4×4 atoms each. This ensures a smooth matching of the leads and the scattering region Hamiltonian. It must be mentioned, that to correct the molecular HOMO and LUMO energy positioning and their gap predicted by DFT, it has been included the phenomenological spectral adjustment explained in section 2.4.1

In the CC, the electrodes was moved until the distance between them was 17.7

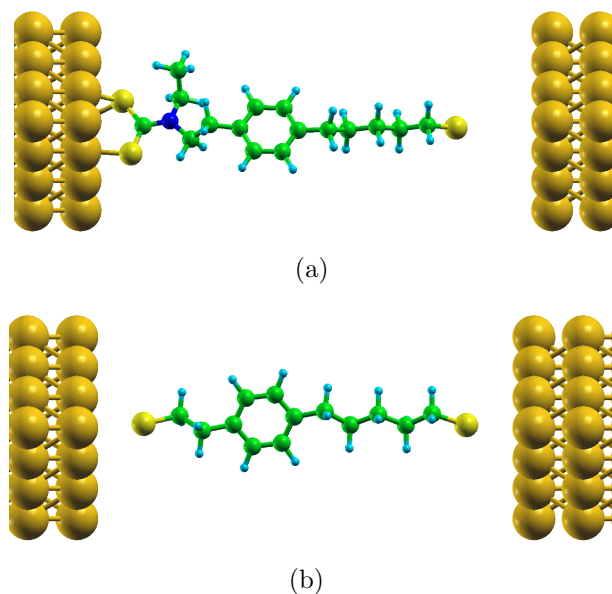
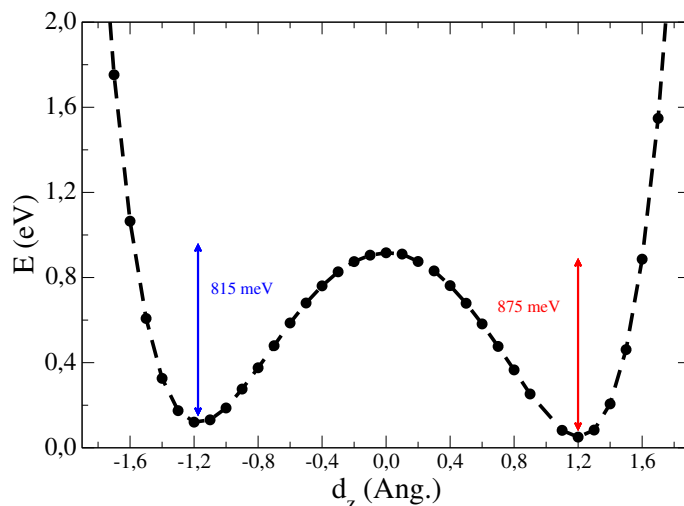
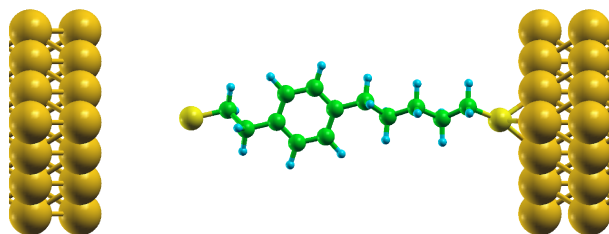


Figure 5.12: Final positions in the OC for MR(2,5) with (a) asymmetric or (b) symmetric anchoring groups. Blue, green, dark blue, yellow and dark yellow represent hydrogen, carbon, nitrogen, sulphur and gold respectively. It is worth mentioning that the distance in (a) between the sulphur in thiol and the gold surface is 4.8 \AA .

\AA and 16.0 \AA for the system with MR(2,5)-asymmetric and MR(2,5)-symmetric, respectively. The final distances in the OC was 23.3 \AA in MR(2,5)-asymmetric and 22.00 \AA in MR(2,5)-symmetric. In both cases, it can be seen that when the end atom is a thiol, and the coordinates are relaxed, the position of such an atom is a hollow position which means that the sulphur atoms sits in front of the center of the triangle pad of the three gold atoms on the Au(111) surface, keeping the equilibrium distance between sulphur and surface. However, when the end group is the di-thiol, the position is not so clear, but is placed mostly in a configuration where one sulphur atoms is on top (sits on gold atom), and the other is on bridge (sits on a bond between two gold atoms), again keeping the equilibrium distance. The maintenance of the equilibrium distance is possible thanks to the flexible character of the molecules under study, which accommodate their backbones to keep the end groups at roughly the same position. It is worth noting a significant difference between the geometry in the OC for each molecule. By the end of the cycle, the MR(2,5)-asymmetric has stuck to the electrode where the DTC groups is. Notwithstanding, the MR(2,5)-symmetric seems to be placed in the middle of the two electrodes. This can be appreciated in the figure 5.12. In order to take into account other possible scenarios, where the MR(2,5)-symmetric is expected to stick to a lead, in this final position, an energy calculation of the system when the molecule is moved towards one or the other lead has been done. In figure 5.13(a) the energy versus position is shown. It can be appreciated that the system has



(a)



(b)

Figure 5.13: (a) Energy versus position in the system with MR(2,5)-symmetric at the end of OC. The zero is the position shown in figure 5.12(b) and (b) position after coordinates relaxation adopted for the calculations. The distance between left sulphur and gold surface is 5.3 \AA

two minimum energy separated by an energy barrier of 815-875 meV. These two minimum energy positions, correspond to the molecule binding to one or the other lead. So, due to the symmetric movement of the leads in the OC as well as the symmetry in its anchoring groups and the fact that in the coordinates relaxation $T \rightarrow 0$, the molecule is finally placed in a position which seems to be an unstable equilibrium position. This position is expected not to occur in real systems, where even at low temperatures, the fluctuations drive the molecule to one or the other equilibrium situation. So, the molecule has been placed in one side, in this case close to the right lead, allowing a new coordinate relaxation. The final position is shown in figure 5.13

In next section, *Theoretical Results*, the transport properties which are going to be shown, belong to the end of CC (named *a* geometry), the end of the initial position (named *b* geometry) and at the end of OC (named *c* geometry), corresponding in the MR(2,5)-symmetric case to the geometry shown in figure 5.13

5.3.2 Theoretical Results

MR(2,5)-asymmetric

In table 5.1 are represented the current-voltage characteristics for MR(2,5)-asymmetric as well as the geometry where they were calculated. These are the three significant positions mentioned before a , b and c . It follows that for the first geometry, the current for negative voltages rises very slowly, with a small slope. For positive voltages, the current has a significant jump at around 0.7 V. Then, the current reaches a plateau. In the positive branch current is always greater than in the negative one. However, for the second and third geometries represented, the branch with larger current is always the negative one. In the middle panel, the current in the positive branch rises slowly reaching a plateau at around 0.6 V with a small jump at 1.1 V. For negative voltages, there is a jump at 0.75 V and the current reaches a plateau, being almost flat until that voltage. Finally, in the bottom geometry, It can be seen that the current for negative voltages rises very quickly and reaches its maximum value at a voltage around 0.25 V and then goes down, showing a small negative differential resistance. For positive voltages, it grows slowly until around 1.10 V where it seems to saturate.

From the rectification ratio, which are shown in the right panels of table 5.2, is easy to see that all geometries exhibit rectification, with dissimilar maximum values at different voltages. In that table, is represented the RR, defined as I_F/I_R , for the first and second geometries, and the inverse of the RR for the third geometry. It can be seen that the maximum ratio is 200 at 0.75 volts, 15 at 0.65 volts and almost 300 at 0.25 volts for a , c and c geometries respectively. In addition, the absolute of the differential conductance is shown. From that, it can be inferred that, as it was expected, the maximum differential conductance value goes down when one moves from first to third geometry, being these values: $10^{-2}G_0$, $10^{-3}G_0$ and $10^{-6}G_0$ for a , c and c geometries respectively. As well as the maximum conductance, the conductance gap, which is defined as the gap between two significant conductance values, can be obtained. It is found that for a geometry this gap is bigger than 1.7 volts, being for b geometry ~ 1.4 V and for c geometry, which as it has been shown exhibit the largest RR, around 1.0 volts. So, It is seen that the conductance gap is reduced when the distance between the electrodes gets larger.

In order to analyze the role of the molecular states in Current-Voltage characteristics, the projected density of states onto carbon atoms at the benzene ring and in the sulphur atoms in thiol and di-thiol as well as the transmission coefficients have been calculated. First, the focus will be put on the a and b geometries. In

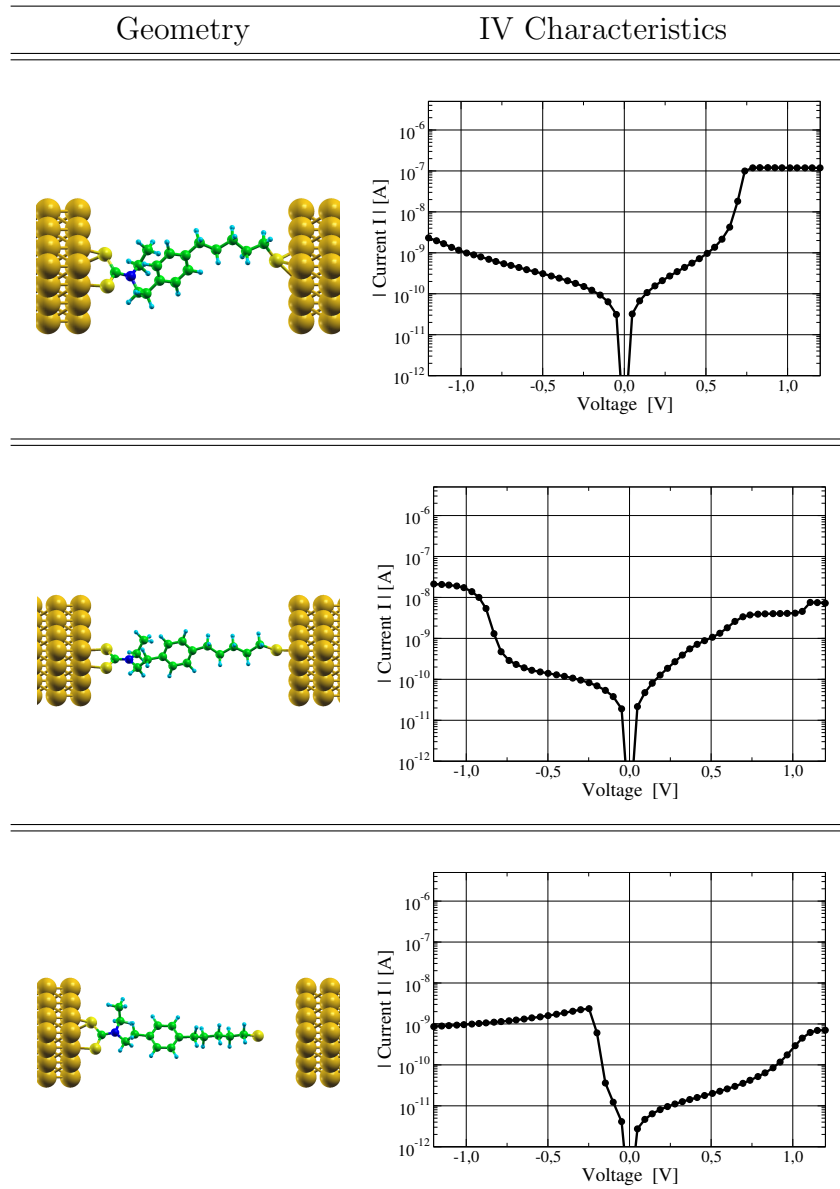


Table 5.1: Geometry and IV characteristics for MR(2,5)-asymmetric. From top to bottom, *a* geometry, *b* geometry and *c* geometry. In Y-axis, absolute current in amperes, and in X-axis voltages in volts.

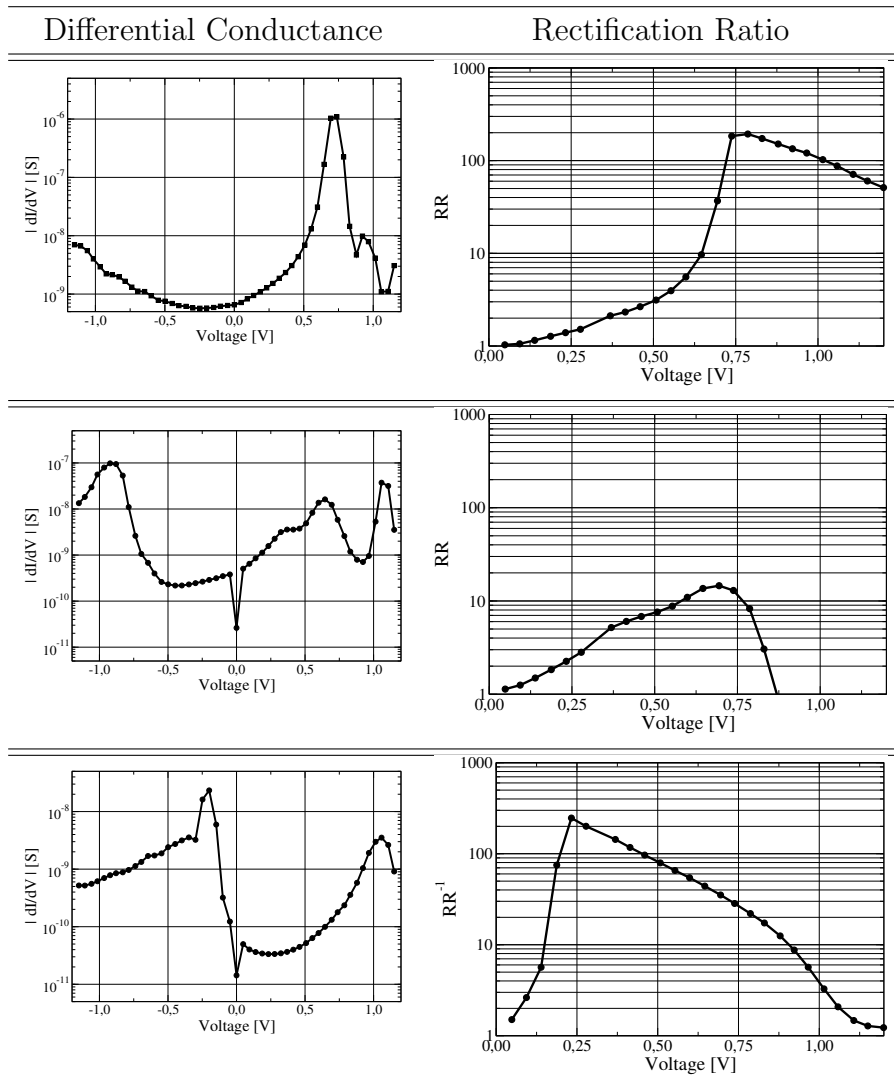


Table 5.2: Differential conductance (left panels) and rectification ratio, for the geometries listed in table 5.1. The differential conductance and voltage are given in Siemens and Volts respectively.

figure 5.14 the PDOS and transmission coefficients for these geometries are shown. In panels 5.14(a) and 5.14(b), which correspond to *a* geometry, It can be seen that the sulphur states, both for thiol and di-thiol, are spread along a large range of energies due to hybridization with gold and do not contribute significantly to the transmission. It is clear that the main features in the transmission are coming from the benzene. There are two well defined benzene states (see for example black curve in panel 5.14(a)) placed at around -0.5 eV and -0.8 eV, which in turns produce sharp resonances in the transmission. This resonances evolve in a different way depending on the bias polarity. This evolution can be better seen in figure 5.15(a), where is represented the energy of the benzene states as a function of the applied bias. On the one hand, It is seen that they follow the left chemical potential. Hence for negative voltages, which means that left chemical potential goes down in energy, they go to lower energies, while for positive voltages go to higher energies and so they get closer to Fermi level. It is seen that there is a clear asymmetry regarding to the voltage where they enter in the bias window. On the other hand, the coupling of the benzene states either the bias is positive or negative does not change too much. In order to see how are the couplings, an estimation of the coupling of the benzene states as a function of the applied voltages has been performed. To do this, a model with Breit-Wigner resonances centered at two different energy positions has been used. Two asymmetric gammas have been utilized for each of the resonances. The results can be seen in figure 5.15(b). The figure shows that Γ_1 for both resonances are in the order of 10^{-2} eV, being Γ_2 for both resonances in the order of 10^{-4} eV. Furthermore, the model shows that the couplings are roughly constant. These small couplings produce, as It was displayed, sharp resonances in the transmission. So, for positive voltages, the first resonance enters in the bias window at around 0.7 V and It gives an abrupt jump in the current (right top panel in table 5.1). However, for negative voltages, the resonance will enter in the bias window at voltages greater than -1.2 V. The local density of states calculated in a small range around -0.5 eV at zero voltage, can be seen in figure 5.15(c). It shows that the state responsible of the rectification is localized in the benzene ring, with some weight in one sulphur in di-thiol and in two carbon atoms belonging to alkene chains which are closest to the phenyl. It can be seen, that this state is an isolated state, which preserves in high degree its molecular form. The asymmetric movement of the benzene states can be attributed, as It was explained in the *Simple Model* section, to an asymmetric voltage drop. In figure 5.15(d) a two dimensional plot of the potential calculated along the molecule is presented. It can see that indeed, there exists the above mentioned asymmetry. In such case, the potential drop is produced in the alkene chains (mainly in right alkene, as It was expected), being almost flat in the ben-

zene ring.

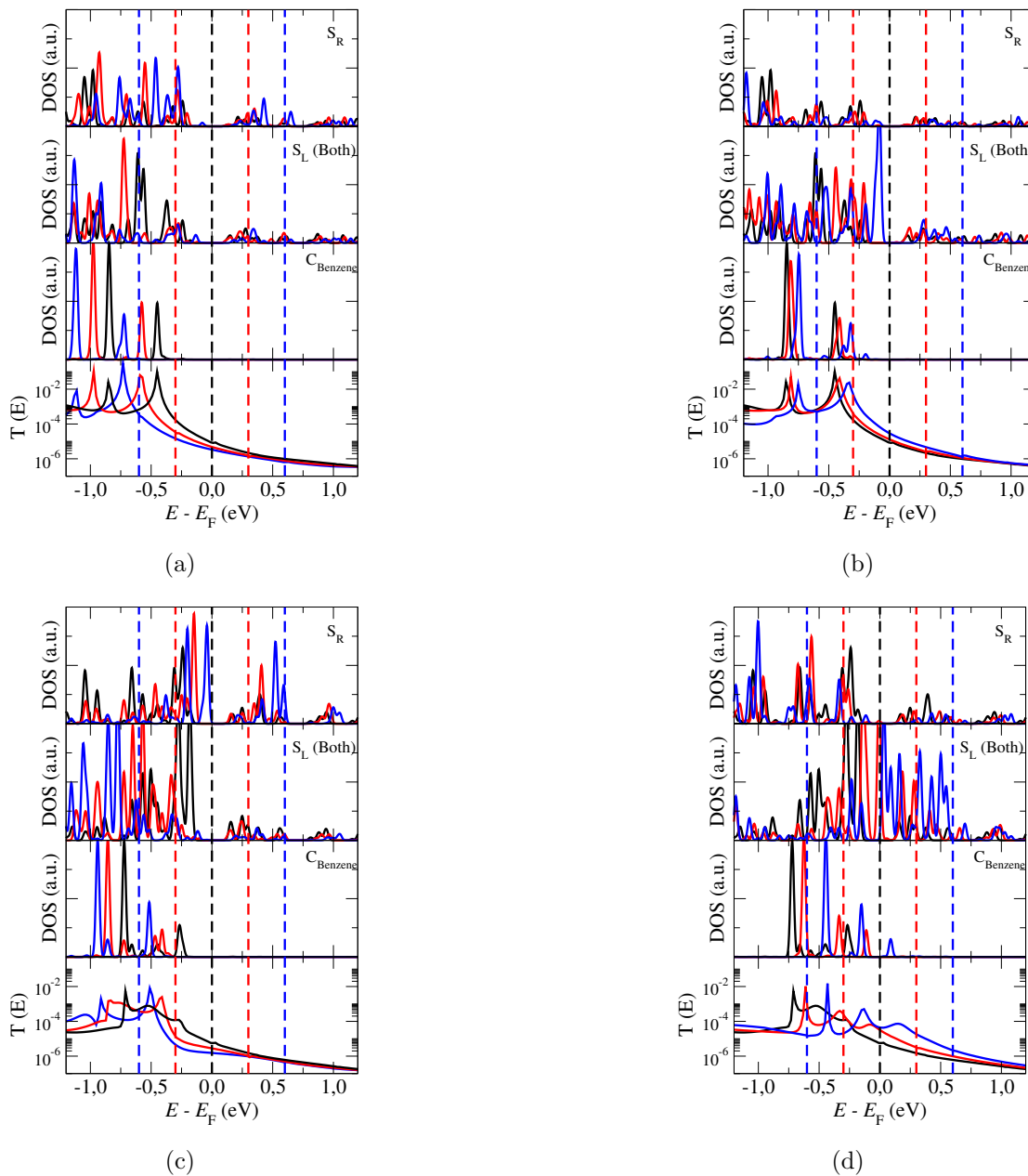


Figure 5.14: projected density of states onto sulphur in thiol (S_R), both sulphurs in di-thiol (S_L) and carbon atoms in benzene ring ($C_{Benzene}$) and transmission coefficients for a geometry in (a) and (b), and for b geometry (c) and (d); panels represent PDOS and $T(E)$ for -1.2 V (blue) -0.6 (red) and 0.0 V (black); right panels represent 0.0 V (black), 0.6 V (red) and 1.2 V (blue). The zero of the energy is the Fermi level at zero voltage. Broken vertical lines represent the bias window when the voltage is -1.2 or 1.2 volts (blue), -0.6 or 0.6 (red) and at zero voltage (black).

The case for b geometry is a bit different. In the figures 5.14(c) and 5.14(d) are shown the PDOS and the transmission coefficients for such geometry. As before,

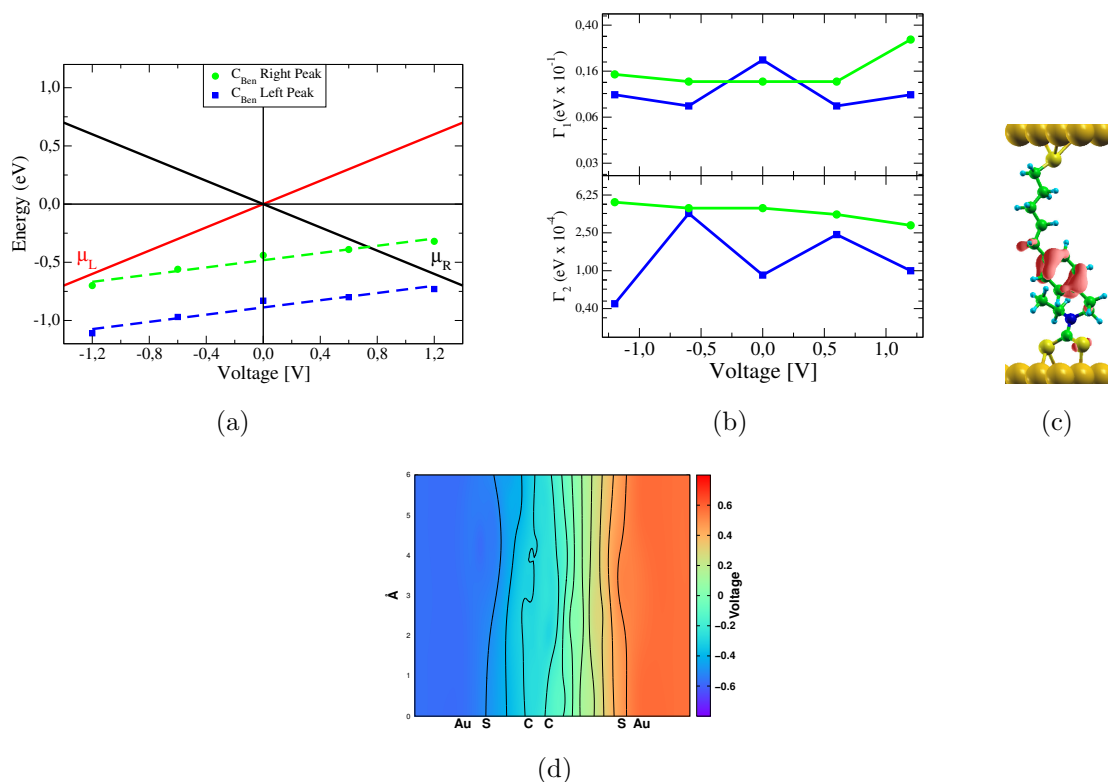


Figure 5.15: (a) evolution of the molecular states energy as a function of applied bias voltage for (a) *a* geometry. Solid red and black lines represent the electrode chemical potentials, which are symmetrically shifted by the applied voltage $\mu_{R(L)} = E_F - (+)qV/2$. (b) an estimation of Γ_1 and Γ_2 calculated with Breit-Wigner model. The colour code represents: highest energy benzene state in green (named $C_{Ben}^{Right Peak}$) and lowest energy benzene state in blue (named $C_{Ben}^{Left Peak}$). (c) local density of states calculated in small range around -0.5 eV at zero voltage. (d) 2D plot of the voltage calculated along the molecule for -1.2 V. Solid contour are separated by 0.1 V.

the sulphur states show a high hybridization and do not produce significantly features in transmission. However in this case, due to hybridization with sulphur atoms in di-thiol, the benzene presents three well separated states at zero voltage (black curve in figures 5.14(c) and 5.14(d)). They are placed at -0.25 eV (small peak) -0.5 eV (the smallest peak) and -0.75 eV (highest peak). As in the previous geometry, these states evolve differently either the bias is positive or negative. Again, the benzene states follow the left chemical potential and they go to lower or higher energies when the bias voltage is negative or positive respectively (see figure 5.16(a)). Nevertheless, in this case the couplings change a lot with the bias voltage. As before, an estimation of the couplings, using the same Breit-Wigner model but with resonances centered at three different energy positions, has been performed. The Γ 's estimated can be seen in figure 5.16(b). So, coming back to the figures 5.14(c) and 5.14(d), It can be seen that the highest energy

resonance evolves from a narrow resonance with almost no tail and a transmission coefficient $\sim 10^{-2}$ to a broad resonance and transmission coefficient $\sim 10^{-4}$, which corresponds with the change in coupling which is shown in figure 5.16(b) (the larger Γ 's the broadener resonances, and the bigger asymmetry between Γ_1 and Γ_2 the smaller the transmission coefficients). Accordingly, for positive voltages the first benzene state enters in the bias window at a voltage around 0.2 V, but due to the big width and small transmission coefficient, there is no appreciable change in the current. Then, the second state enters in the bias window at around 0.5 V, but again, because of the broad resonance, there is a smooth jump in the current. Finally, at almost 1.0 V, the third state enters an small but sharper jump happens. However, for negative due to the no tail of the resonance, the current is almost a plateau until the the first narrow resonance enters in the bias window producing a brisk jump in current at around -0.8 V. As a consequence of this jump, the reverse current becomes larger than the forward current. In figure 5.16(c) the local density of states calculated around the highest energy benzene state, which means in a small range around -0.25 eV, is shown. It is noted that in this case, the state is not only localized on the phenyl, but also in both end groups, in the nitrogen and in the carbon atoms in the alkene chains closest to the phenyl. So, the state is less isolate than in the previous case. It becomes more like in the previous geometry for negative voltages, but there is a strong coupling for positive voltages. The voltage drop calculated as before, is shown in figure 5.16(d). It can see, that the main voltage drop is still in the alkene chains, but due to the poorer isolation, there is some drop in the benzene ring. In fact, this could have been inferred from the slope of the energy versus applied voltage straight lines: in the former case, namely for *a* geometry, the slope of the green and blue straight lines in figure 5.15(a) was ~ 0.16 , being for the *b* geometry (green, violet and blue straight lines in figure 5.16(a)) ~ 0.25 , which means that in the latest case, the benzene states are more affected by the left chemical potential due to the poorer isolation.

Up to now, It has been shown that rectifying is driven by the benzene states. However, It is going to show that when the molecule is almost in the break situation (*c* geometry), some different states play the key role in rectification mechanism. In figure 5.17 the PDOS and transmission for *c* geometry are shown. Again, sulphur states in di-thiol are spread due to hybridization, but in this case, because of the larger distance between the sulphur in thiol and right electrode, the states of such an atom do not show hybridization and produce narrow resonances in transmission. The carbon states in benzene ring also present narrow resonances in the transmission, but in this case, they are placed at lower energies than in the previous systems. Albeit they also move following the left chemical potential,

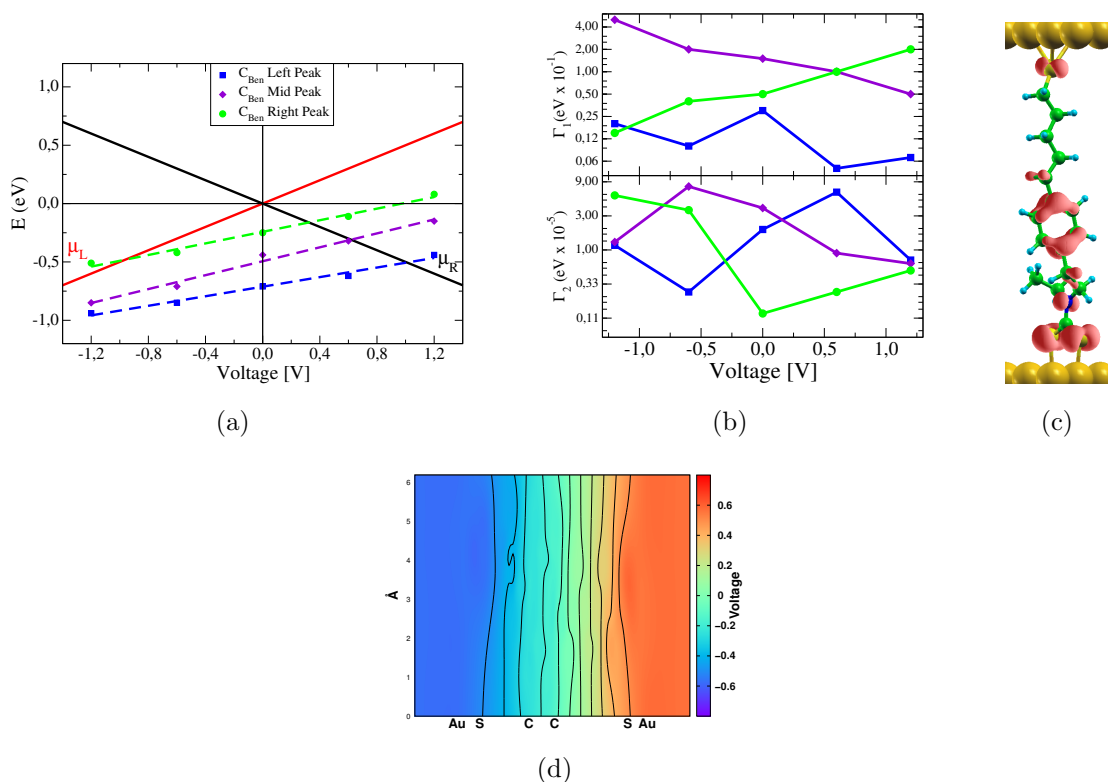


Figure 5.16: (a) evolution of the molecular states energy as a function of applied bias voltage for (a) b geometry. Solid red and black lines represent the electrode chemical potentials, which are symmetrically shifted by the applied voltage $\mu_{R(L)} = E_F - (+)qV/2$. (b) an estimation of Γ_1 and Γ_2 calculated with Breit-Wigner model. The colour code represents: highest energy benzene state in green (named C_{Ben} Right Peak), middle energy benzene state in violet (named C_{Ben} Mid Peak) and lowest energy benzene state in blue (named C_{Ben} Left Peak). (c) local density of states calculated in small range around -0.25 eV at zero voltage. (d) 2D plot of the voltage calculated along the molecule for -1.2 V. Solid contour are separated by 0.1 V.

they do never enter in the bias window. In this case, the relevant state comes from the sulphur in thiol, as it can be seen in the figure 5.17(c) where the local density of the states calculated around such state is presented. Notwithstanding, the state is influenced by the right chemical potential, and so the rectification is in opposite bias polarity. The state is placed, at zero voltage, at around -0.18 eV. When the voltage is negative, which means that the right chemical potential goes to higher energies, that state also goes up in energy and enters quickly in the bias window giving a really abrupt jump in the current (see right bottom panel in table 5.1). This does not happen for positive voltage, because the sulphur state stays always outside the bias window, as It can be checked in the figure 5.17(d), where is presented the evolution of the energy as a function of the applied bias.

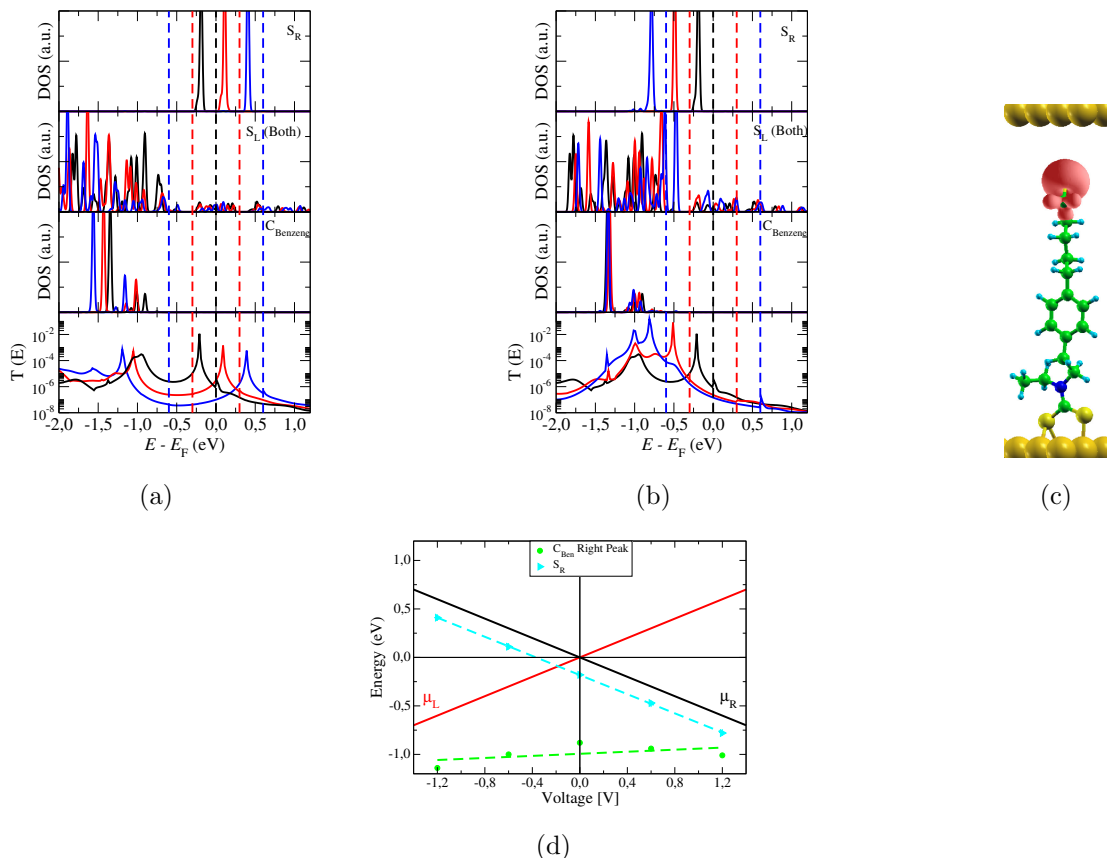


Figure 5.17: projected density of states onto sulphur in thiol (S_R), both sulphurs in di-thiol (S_L) and carbon atoms in benzene ring ($C_{Benzene}$) and transmission coefficients for c geometry; panels represent PDOS and $T(E)$ for (a) -1.2 V (blue) -0.6 (red) and 0.0 V (black) and (b) 0.0 V (black), 0.6 V (red) and 1.2 V (blue). The zero of the energy is the Fermi level at zero voltage. Broken vertical lines represent the bias window when the voltage is -1.2 or 1.2 volts (blue), -0.6 or 0.6 (red) and at zero voltage (black). (c) local density of states calculated in small range around -0.18 eV at zero voltage. (d) evolution of the molecular states energy as a function of applied bias voltage. Solid red and black lines represent the electrode chemical potentials, which are symmetrically shifted by the applied voltage $\mu_{R(L)} = E_F - (+)qV/2$. The colour code represents: highest energy benzene state in green (named C_{Ben} Right Peak), and the sulphur state in thiol in magenta (named S_R).

MR(2,5)-symmetric

As in the previous case, this section begins showing the current-voltage characteristics for MR(2,5)-symmetric which are presented in table 5.3. It can be seen that for a and b geometries, the current-voltage characteristics are very similar. For positive voltages, they show a jump at around 0.25 V and then they saturate. This jump is sharper for system b . The current value when they are saturated is of the order of $5 \cdot 10^{-7} A$. For negative voltages they grow slowly with a smooth slope. In the c geometry however, the current for positive voltages has a jump at a voltage a bit smaller than 0.12 V, and then it goes down, showing negative differential resistance. Unlike the positive bias, for negative the current rises slowly with smooth slope, as in the previous geometries.

As It happened to previous molecule, all geometries show rectification, but in this case, it grows from a to c and its maximum goes to smaller voltages (see right panels in table 5.4). The maximum RR is 4 at 0.3 V, 50 at 0.3 V and 300 at 0.14 V for a , b and c geometries respectively. With regard to the maximum differential conductance (left panels in table 5.4), it follows that for a and b geometries is very similar $\sim 10^{-2} G_0$, being for c geometry $\sim 10^{-4} G_0$. Finally, it must be pointed out the difficulty to give the value of the conductance gap in a geometry, due to the fact that the differential conductance is roughly of the same order of magnitude for both bias polarities. However, it can be said that for b geometry, is ~ 1.0 V., being for c geometry bigger than 1.2 V.

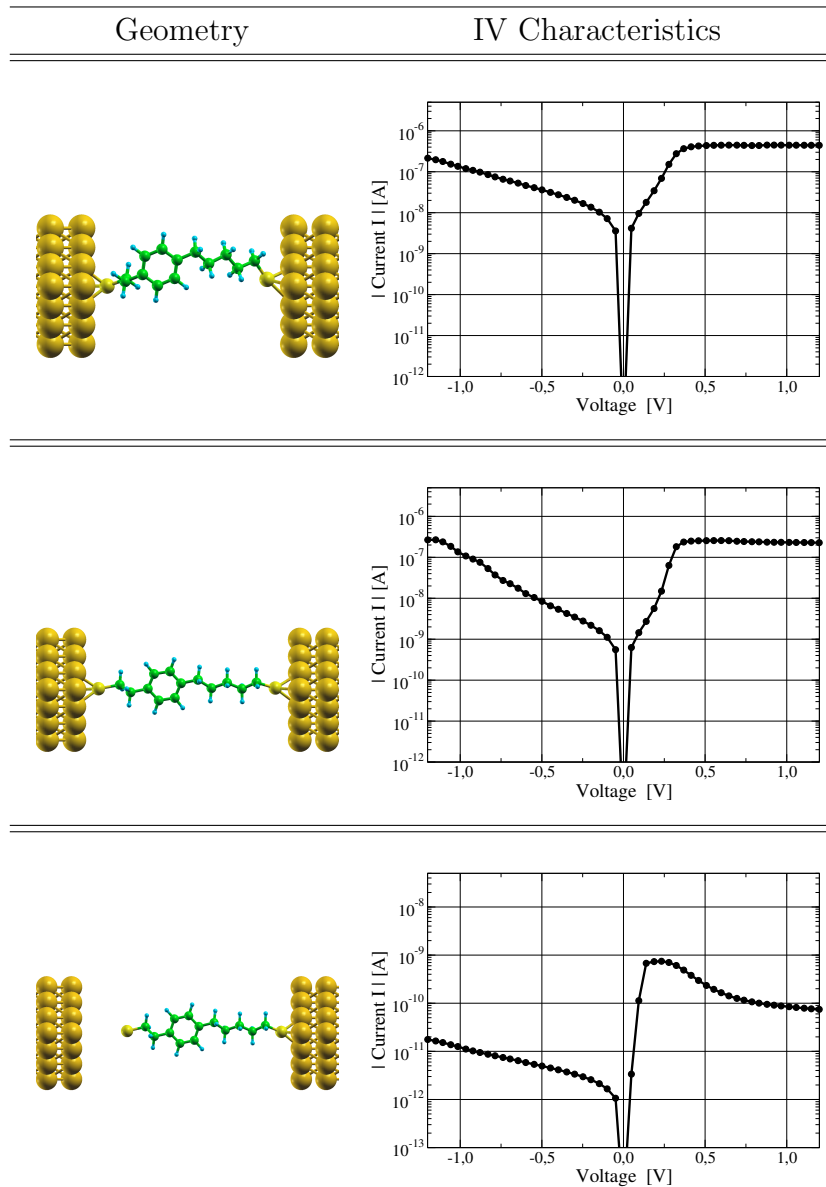


Table 5.3: Geometry and IV characteristics for MR(2,5)-symmetric. From top to bottom, *a* geometry, *b* geometry and *c* geometry. In Y-axis, absolute current in amperes, and in X-axis voltages in volts.

To see the role of the different molecular states in the current-voltage behaviour, the projected density of states and transmission coefficients have been calculated as before. Figure 5.18 shows the PDOS and transmission coefficients for system *a* (top panels) and for system *b* (bottom panels). It is seen that, as usual, the states of sulphur atoms are spread due to hybridization with gold and do not contribute to the transmission in any system. Instead of this, the transmission features are mainly due to benzene states. In both geometries can be appreciated two benzene states, which are placed at -0.25 eV and -0.62 eV at zero bias voltage

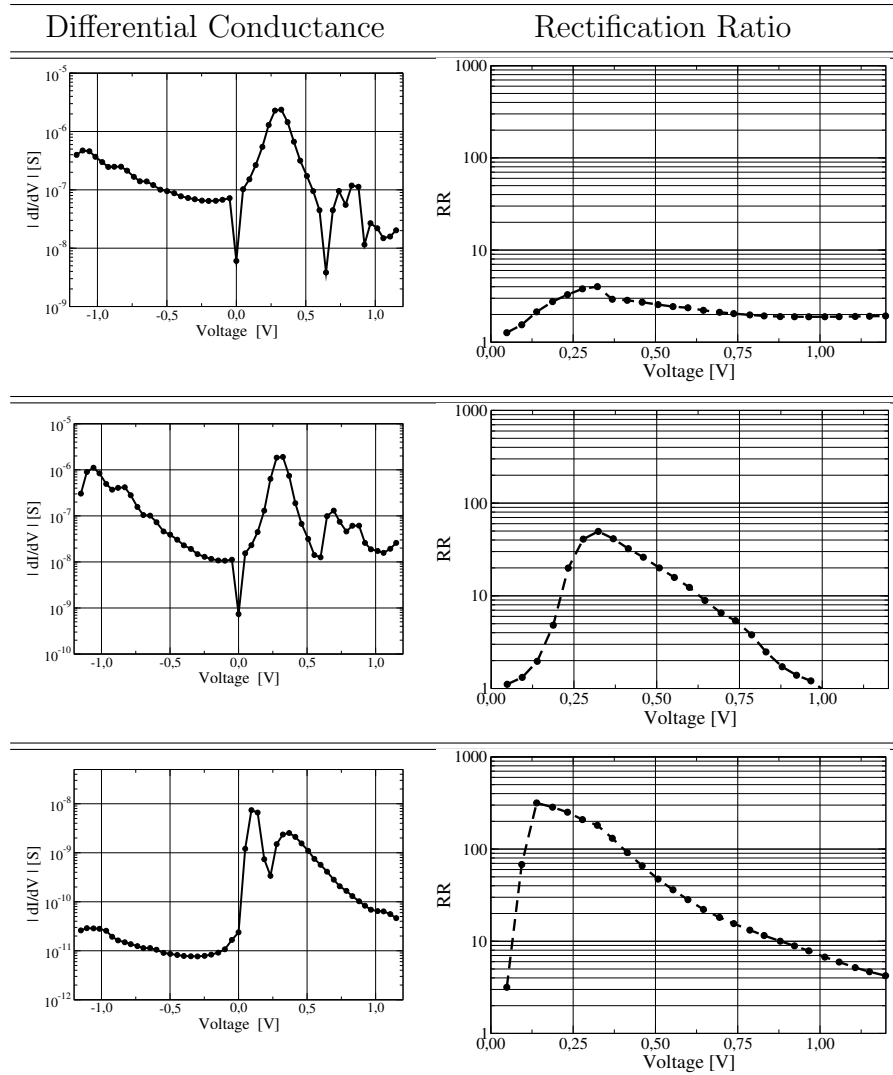


Table 5.4: Differential conductance (left panels) and rectification ratio, for the geometries listed in table 5.3. The differential conductance and voltage are given in Siemens and Volts respectively.

(see, for example, black curve in figure 5.18(a)). The highest energy state gives into the transmission, a broad resonance in a which is narrower in b geometry, while the lowest gives a small narrow resonance in a system, which is not present in b system. When a negative voltage is applied to the system, benzene states follow the left chemical potential and they move to lower energies and in turn the resonances which they produced. For the opposite voltage polarity, they go to higher energies, getting closer to the Fermi level. So, It is clear from the PDOS and transmission coefficients, that the behaviour of the resonances is very similar, and the only difference is the width of such resonances. This can be seen clearer in the figure 5.19, where the evolution of the energy as a function of applied voltage for both benzene states, as well as an estimation of $\Gamma_{1,2}$ for the highest energy benzene state is shown for both systems. As before, a model with Breit-Wigner resonances centered at two different energy positions has been used for Γ 's estimation. From that figure, is easy to see that, the benzene state moves with left chemical potential and it is going to enter, in both geometries, at roughly the same positive voltage ~ 0.25 V. However, as It can be seen in figures 5.19(b) and 5.19(d), even though the couplings for each geometry are approximately constant as a function of the applied voltage, there is a difference between them: in a geometry $\bar{\Gamma}_1 \sim 0.068$ eV , $\bar{\Gamma}_2 \sim 0.0019$ eV and in b geometry $\bar{\Gamma}_1 \sim 0.035$ eV , $\bar{\Gamma}_2 \sim 0.00079$ eV, which means that from a to b , the Γ 's have been divided by 2. This produces a narrowing of the resonance, which in turns enhances the rectification ratio (see right top and middle panel in table 5.4. Finally, It is worth noting how is the benzene state which plays the fundamental role in such behaviour. In figure 5.20 can be seen the local density of states calculated in a around -0.25 eV at zero voltage. It shows, indeed, that the state is localized in the phenyl ring, being an isolated state.

To finish this section, It is going to be discussed the current-voltage features for c geometry. In figure 5.21 PDOS and transmission coefficients for such system are shown. As It happened with the molecule MR(2,5)-asymmetric, in this situation, close to the break, the rectification mechanism is driven by the sulphur state as It can clearly seen from the figure. However, unlike the previous one, the molecule now is linked to the right electrode, and so is the state in the left thiol which plays the key role. It is worth saying, that due to the fact that MR(2,5)-symmetric has two stable positions near to the break as It was shown above (link to one or other electrode), the opposite situation has been studied too. It was found a similar current-voltage characteristics. The difference was the sulphur state giving resonance, which was the right sulphur state, and the current-voltage characteristics (and hence RR and differential conductance) which show the opposite behaviour.

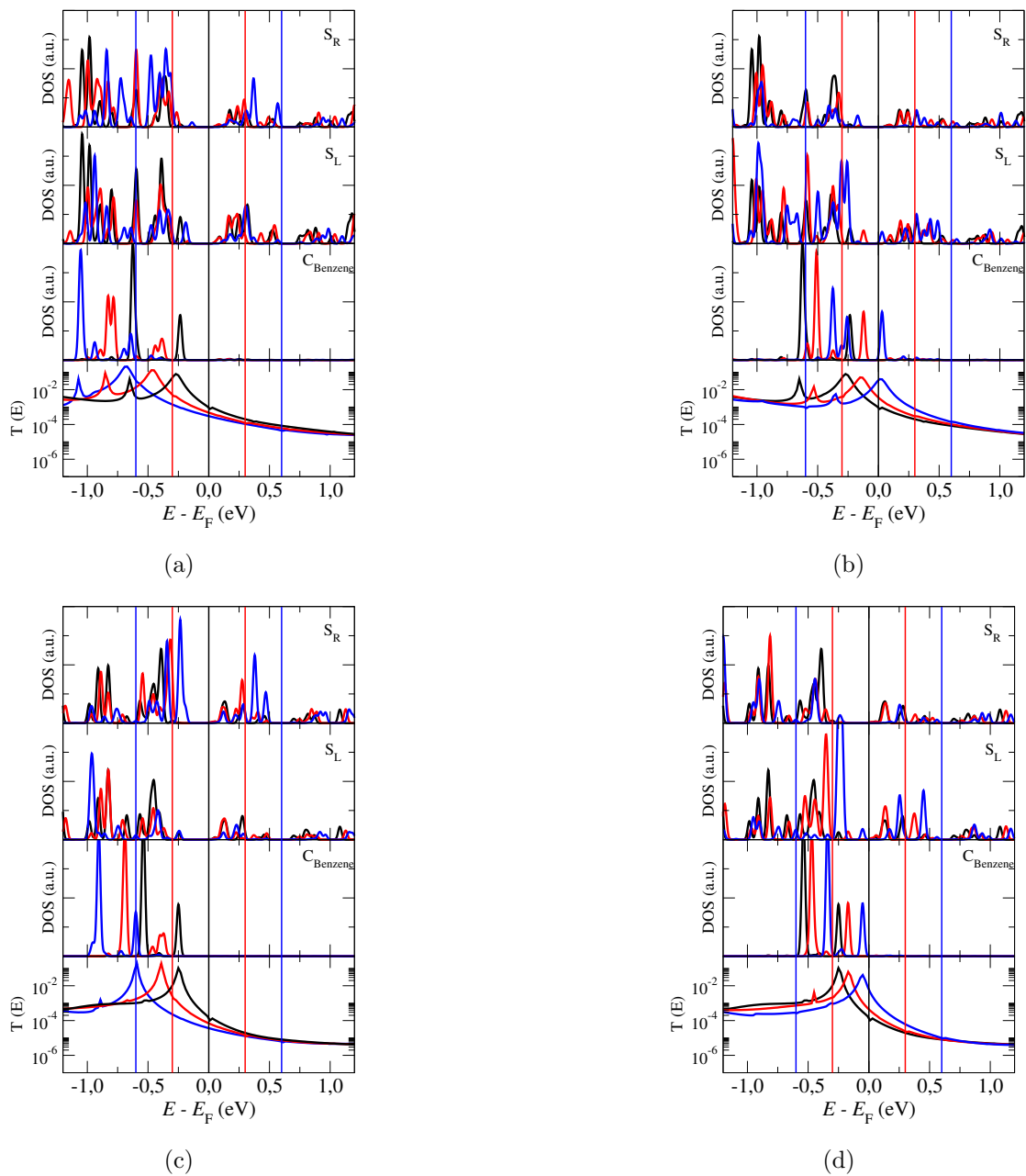


Figure 5.18: projected density of states onto sulphur in right (S_R) and left (S_L) thiol and in carbon atoms in benzene ring ($C_{Benzene}$) as well as the transmission coefficients for a geometry in (a) and (b), and for b geometry (c) and (d); panels represent PDOS and $T(E)$ for -1.2 V (blue) -0.6 (red) and 0.0 V (black); right panels represent 0.0 V (black), 0.6 V (red) and 1.2 V (blue). The zero of the energy is the Fermi level at zero voltage. Broken vertical lines represent the bias window when the voltage is -1.2 or 1.2 volts (blue), -0.6 or 0.6 (red) and at zero voltage (black).

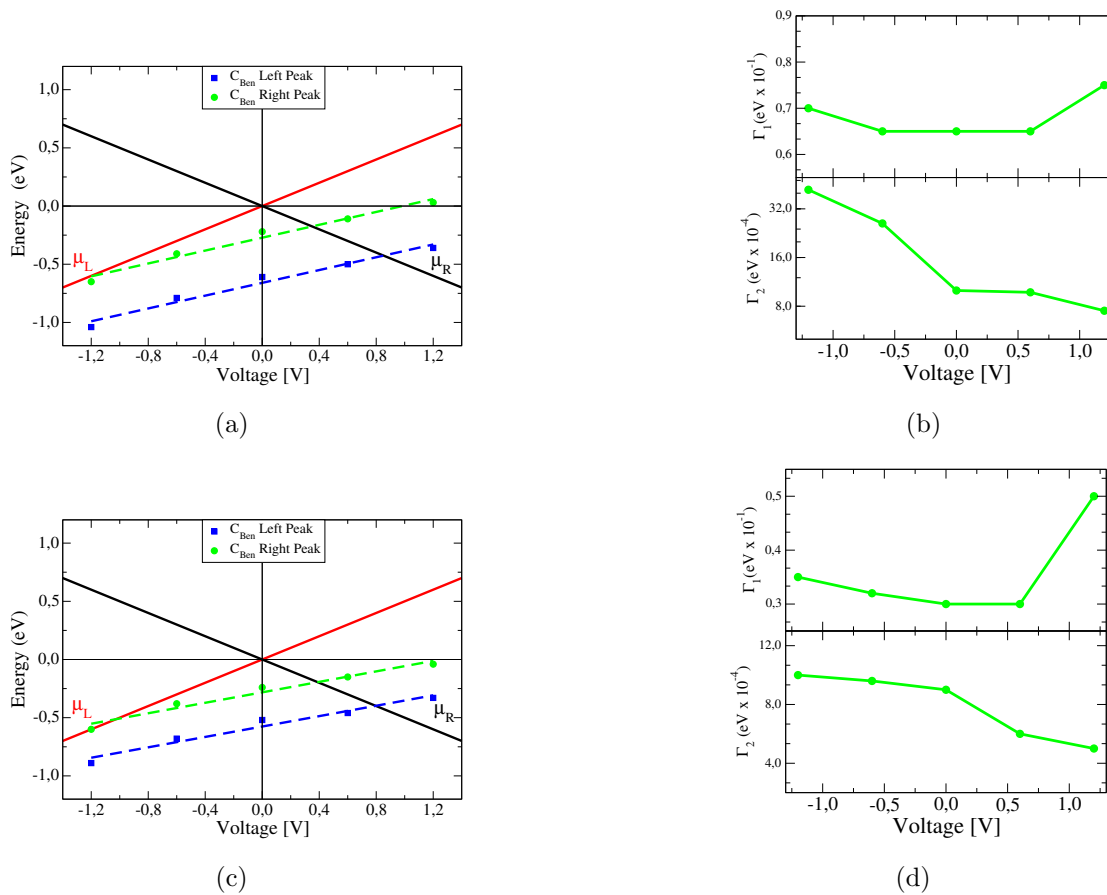


Figure 5.19: in left panels, evolution of the molecular states energy as a function of applied bias voltage for (a) *a* geometry and (c) *b* geometry. Right panels, an estimation of Γ_1 and Γ_2 calculated with Breit-Wigner model for (b) *a* geometry and (d) *b* geometry. In right panels, solid red and black lines represent the electrode chemical potentials, which are symmetrically shifted by the applied voltage $\mu_{R(L)} = E_F - (+)qV/2$. The colour code represents: highest energy benzene state in green (named C_{Ben} Right Peak) and lowest energy benzene state in blue (named C_{Ben} Left Peak).

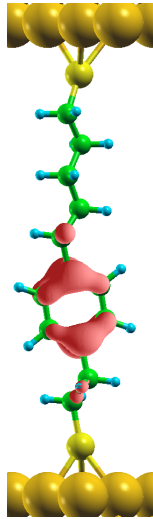


Figure 5.20: Local density of states calculated around -0.25 eV at zero voltage for system *b*.

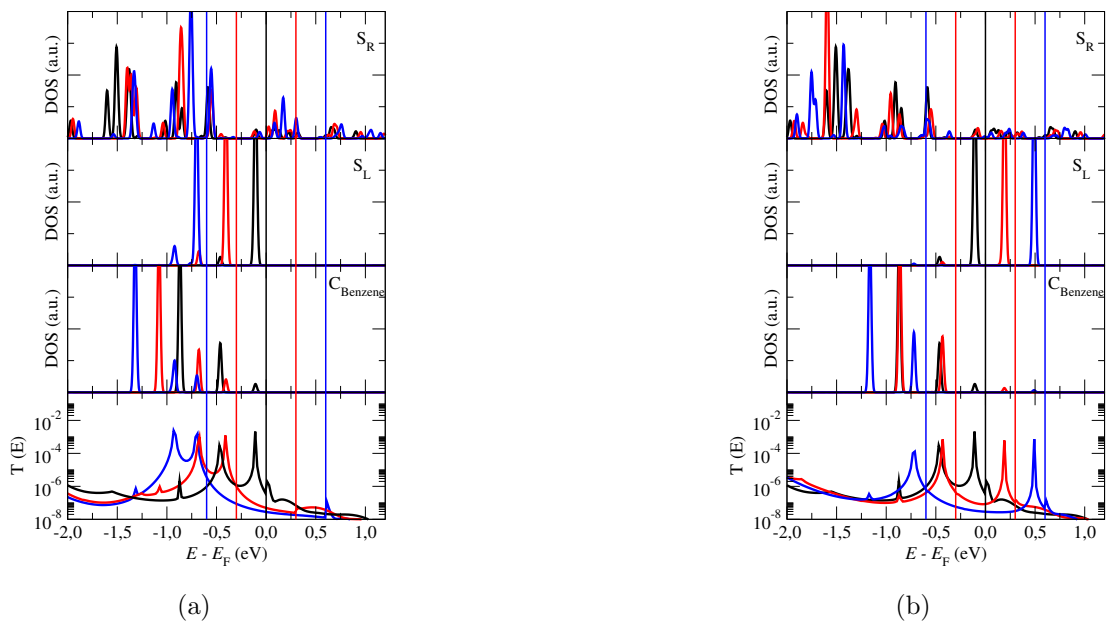


Figure 5.21: projected density of states onto sulphur in right (S_R) and left (S_L) thiol and in carbon atoms in benzene ring ($C_{Benzene}$) as well as the transmission coefficients for *c* geometry. Left panel represents PDOS and $T(E)$ for -1.2 V (blue) -0.6 (red) and 0.0 V (black); right panel represents 0.0 V (black), 0.6 V (red) and 1.2 V (blue). The zero of the energy is the Fermi level at zero voltage. Broken vertical lines represent the bias window when the voltage is -1.2 or 1.2 volts (blue), -0.6 or 0.6 (red) and at zero voltage (black).

5.4 Remarks

It has been proved that the asymmetric tunneling barriers rectification mechanism is achieved using molecules of the MR family. These molecules exhibit rectification ratios as big as 200 (molecules with asymmetric anchoring groups) and 50 (molecule with symmetric anchoring groups) when the molecule is linked to both leads. In this regime, the state which drives the rectifications, is one state localized on the benzene ring and with an energy below to the Fermi energy, so the conduction is through electron instead of holes. Both molecules show rectification ratios as big as 300 when the system is close to the break. In latest case, the rectification is driven by sulphur state closer to the Fermi level, but still below.

In the MR(2,5)-asymmetric, It has shown that the rectification is bigger in the studied situation when the distance between the leads was the smallest. In this situation, the couplings between the phenyl ring and the system were small, giving narrow resonances. When the distance between the leads gets bigger, the couplings gets larger too, and the RR becomes smaller. There are a lot of sulphur with an energy around the energy of the benzene states, making bigger the couplings. In the MR(2,5)-symmetric, It in the opposite way. The rectification gets bigger when the distance between the leads gets larger. This indicate that due to the different anchoring groups, the mechanism which links the molecule is different, and produce a change in the RR regime.

Also, It has been shown that the conductance in the geometry and voltage range where the molecules show the maximum RR is in the order of $10^{-2}G_0$, $10^{-3}G_0$ for both molecules, which could serve for future applications. However, in the case of MR(2,5)-asymmetric, the voltage where It shown the maximum RR is around 0.75 V, which is still too big for technological applications. Notwithstanding, the use of a voltage gate, which gets closer to the Fermi level the states which are involved in rectification mechanism may improve the system.

Summarize, It has been reported that the MR family of molecules, indeed could lead to future applications in molecular electronics technology. Nevertheless, some things must be clarified, as for example the rectifying behaviour of such molecules at room temperature, because the broadening of the resonances when the temperature is high, could destroy the rectification.

Exploring New Materials as Electrodes in Molecular Electronics

6.1 Introduction: Graphene as a possible electrode

Traditionally, the contacts in molecular electronics have been made by noble metal as for example gold, silver or platinum. However, as It was noted in a previous chapter (4), the few-particle nature of the contacts in single-molecule devices leads to a lack of mechanical robustness. It also leads to a large phase space of coupling configurations, each with a different conductance. The spread in experimental values of the transport response is overtaken by the use of a statistically averaged conductance histogram. Because of this reason, much effort has been concentrated on improving the robustness of the devices by searching and testing new generations of contact groups [156–158].

In this sense, graphene could replace noble metals as the material for the electrodes to help solve these key issues. The use of graphene may have several clear advantages. First, its lack of atomic diffusivity makes each gap geometry stable over time. Second, graphene's planar structure nature allows for the visualization of the junctions and possibly a better control over the actual molecule positioning. Third, compared to the more bulky metallic electrodes, the molec-

ular junction can be placed closer to a gate; graphene electrodes could lead to a reduced gate-field screening and therefore to an enhanced gate coupling. Furthermore, the conductance of few-layer graphene is largely gate independent so that features of the contacted molecules may not be masked by electrodes' response to the gate. Recently it was also proven experimentally that stable and gateable molecular junctions can be formed by depositing molecules on top of a graphene nanogap fabricated by electroburning, where the molecules' anchor groups were probably contacting the edges [159]. Accordingly, graphene is worthy of being studied as a possible material of choice for a single-molecule electrodes. Notwithstanding, graphene has its own series of problems which must be overcome. For example its complex edges morphology, passivation and oxidation states are not fully characterized yet. In addition, the ability to fabricate nanogaps where gap length and edge morphology are controlled with almost atomic accuracy is still to be developed.

In last times, several theoretical papers have proposed bridging graphene electrodes with molecules, whose anchor groups would be chemisorbed to the electrodes' edges [62, 160–162]. However, it was shown that the tribological nature of graphene edges leads to a large variability in the transport response of such devices. An alternative approach that avoids edge anchoring was also advanced [163, 164] where fullerene-based dumbbell wires were physisorbed onto graphene, or molecular wires were physisorbed onto carbon nanotubes. In addition, by contacting the molecules deep inside the sheets, trouble related to the size mismatch between the physical gap and the length of the molecule is avoided from the outset [163]. Notice that this strategy cannot be implemented with bulky noble-metal electrodes.

In this chapter, it is going to explore the electronic properties and the low-voltage electrical response of molecular wires physisorbed onto graphene leads. Physisorption is a gentler attachment to graphene than chemisorption. The distortion of the geometry and the electronic structure of both molecule's and graphene's contact area is expected to be only moderate and mostly related to screening effects. Specifically, charge transfer between molecule and electrodes is strongly suppressed so that the contact-induced dipoles are expected to be small. The molecular wires which are going to be analyzed have planar anchor groups which is expected to enhance the mechanical stability of the junctions and provide an effective conductance averaging. In next section will presented the system under study as well as the theoretical method. Then, the main theoretical results will be discusses to finish in last section with some remarks.

6.2 System Under Study and Theoretical Method

A schematic plot of the single-molecule junction discussed in this chapter can be seen in figure 6.1. The system is comprised by a trimer molecule made up of three phthalocyanin units linked by butadiynes, e.g., atomic chains made of four carbons. The molecule has been placed over two sheets of graphene that are terminated in armchair configuration passivated by hydrogen atoms in a 1-1-1 sequence, which is predicted to be the most stable reconstruction and passivation on this kind of edge [?]. The reference distance of the gap length d_0 has been chosen so that the central phthalocyanine covers the gap entirely. The height of the molecule above the sheets, has been chosen doing an energy minimization regard to the vertical distance. To do this, the vertical distance of the whole molecule has been varied in steps of 0.2 \AA , allowing coordinates relaxation (with the atoms in graphene fixed) in each distance and calculating the energy. It has been found that in the minimum energy position, the molecules is placed at roughly the same height above the sheets, being the distance $d_h \sim 3.5 \text{ \AA}$. So this was the starting geometry for the calculations.

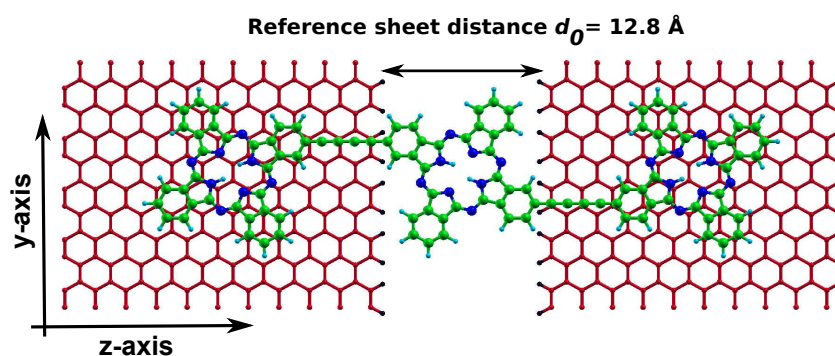


Figure 6.1: Plot of the single-molecule junction studied. Red, black, green, light-blue and blue represent carbon and hydrogen in graphene, and carbon, hydrogen and nitrogen in the molecule respectively.

The calculations has been performed using the DFT code SIESTA. In order to better described physisorption, the van der Waals functional of Dion *etal* has been use for the exchange and correlation potential. The Hamiltonian and overlap matrices, as well as the potential and density have been calculated employing a real-space grid with fineness defined with an energy cutoff of 200 Ry. In the coordinates relaxation, the atoms were relaxed until the forces were smaller than 0.05 eV/\AA . This coordinates relaxation was done utilizing different basis sets (SZ,

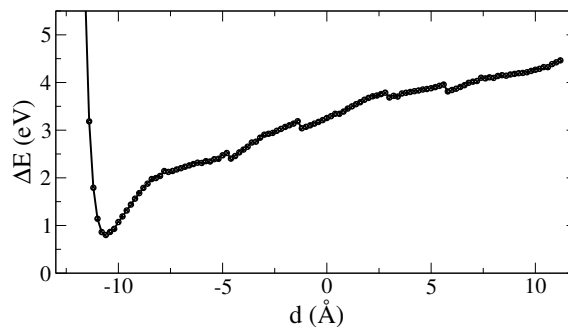
SZP and DZ) finding no significant differences in the final position, which means that the relaxation is roughly independent of the basis employed. Nevertheless, the electronic structure is very sensitive to the choice of the basis: it was found large differences in the transmission and the density of states when the basis set improved from SZ to SZP and DZ. There are not however many changes in moving from DZ to DZP, which implies that the electronic structure is well converged with DZ. In consequence, this basis (DZ) has been used to performed all electronic structure calculations. The junctions analyzed here are made periodic along the direction perpendicular (y) to electronic transport (z). Each electrode has ten principal layers, where each principal layer has two columns of carbon atoms. This is found enough to accommodate the phthalocyanine molecules on top of the sheets and ensure that electronic structure converges to the bulk electronic structure at the leftmost and rightmost layers.

The junction transport properties have been computed using the transport code GOLLUM. The calculations has been performed utilizing the Γ -point to start with, and then the convergence of the zero-voltage transmission coefficient $T(E)$ as a function of the number of transverse k points has been tested. The changes in transmission coefficients and in the conductance have been discussed when the molecule is displaced across the plane in directions parallel and perpendicular to the edges or when the graphene sheets are pulled away or pushed towards each other.

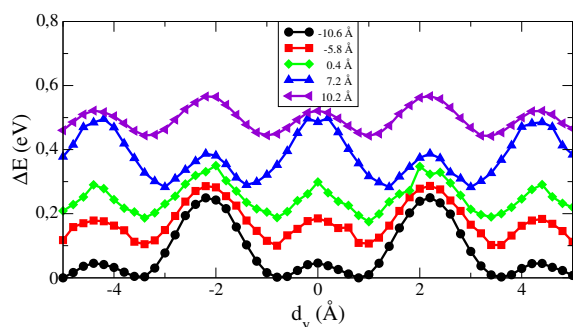
A Glimpse to the Energy of the Systems

It has been computed the physisorption energy for chemical detachment of this molecules and it was found energy barriers of the order of 2 eV. It has been also computed the energy of the system when the gap length is varied in the range $d \in (-11.8, 11.2)\text{\AA}$ in steps of 0.2\AA . A plot in figure 6.2(a) of the junction energy as a function of d (e.g., when the electrodes are pulled away or pushed) shows a minimum at about $d \sim -10.6\text{\AA}$. The existence and position of the minimum reflects a tradeoff between two opposing factors: hydrogen-passivated edge repulsion versus molecule-graphene bonding.

It had been computed previously the energy barriers for phthalocyanine monomers sliding on top of a infinite graphene sheet. It was found values $\sim 40meV$, which were consistent with a previous calculations [?]. It has been displaced sideways the trimer in figure 6.1 for fixed d , so that it drifts parallel to the physical gap. Due to the trimer has two phthalocyanine anchor groups bonded to the sheets as well as



(a)



(b)

Figure 6.2: Energy analysis of the junction as a function of (a) the gap length d and (b) as a function of the lateral displacement d_y for several d (in the chart). In the last figure, the energy curves have been displaced in energy to fit them in the same figure.

two polyne chains and a third anchor group interacting with the edges, it was expected energy barriers two or three times bigger than the result for the monomer. The junction energy, plotted in figure 6.2(b), shows a smooth and periodic variation of the energy, whose period reflects the underlying graphene lattice. The energy barriers are of about 0.1 to 0.2 eV, consistent with the previous analysis. From this energy barriers it can be made a rough estimate of the molecule's drift length along the gap, $r \sim \sqrt{4Dt}$, using an Arrhenius equation for the diffusion constant

$$D = D_0 e^{-E_B/k_B T} \quad (6.1)$$

where it is taken $D_0 \sim 10^{-4} \text{ cm}^2/\text{s}$ and $E_B = 0.2 \text{ eV}$. It is found that the trimer would stay fixed at its position for temperatures up to about 100 K, but it should drift at room temperature. This quick analysis indicates that the trimer junction would be stable if energy barriers of about 0.5 eV were achieved. Obtaining such high-energy barriers may be done by attaching suitable side groups, or better tailoring the anchor groups.

6.3 Main Transport Results

The Γ -point estimates of $T(E)$ for different gap lengths d are plotted in figure 6.3 at intervals of 1.0 \AA^{-1} . The figure shows that the position of the Breit-Wigner (BW) resonances remains almost constant (see for example, panel (c) at the energies around -0.9 eV and at energies around 0.1 eV -LUMO-). The same behaviour has been found for other junctions comprising similar molecules [?]: the energy position of the BW resonances for a given graphene-based junction does not depend on the molecule position relative to the physical gap, provided that the bonding mechanism is by physisorption. This universality could be anticipated: physisorption carries no charge transfer between the molecule and the sheets, nor associated dipole moments. This is so, because both sides of each contact are mostly made up of the same chemical species: carbon. Also, the $\pi - \pi$ hybridization between molecular orbitals and the electrode states is weaker than for the bonds present in most noble metal/single-atom contacts, and does not have a large impact on the nature of the molecular orbitals.

The position of the molecular levels of a molecule is not accurately given by DFT by a number of reason, some of them were pointed out in the section 2.3.4. As a consequence, the number and position of the true transmission resonances is expected to be different from those shown in figure 6.3. However, the nature and position of the true strongly correlated quasiparticle states of the molecule depend only on the hybridization, the net charge of the molecule, and the screening provided by graphene. It is noted that these do not change as the molecule is displaced, because of the physisorbed nature of the chemical bond. It is deduced that if it would be possible to compute the true transmission resonances accurately, then it would be seen that their energy position does not change with the molecule position. Hence, it can be concluded that the universality of the energy position of the transmission resonance is robust even if strong correlations are included.

Figure 6.3 shos that $T(E)$ computed at the Γ -point changes by orders of magnitude at energies placed between two given BW resonances. A closer inspection indicates that this is so because Fano-like resonances tend to appear at the gaps between two BW resonances. In contrast to the BW resonances, the energy position of the Fano-like resonances shifts as the length of the physical gap changes or if the molecule is moved around. Because this also happens at the highest occupied

¹Direct tunneling between electrodes ceases to exist for $d > -4.6 \text{ \AA}$ relative to d_0 for the chosen basis.

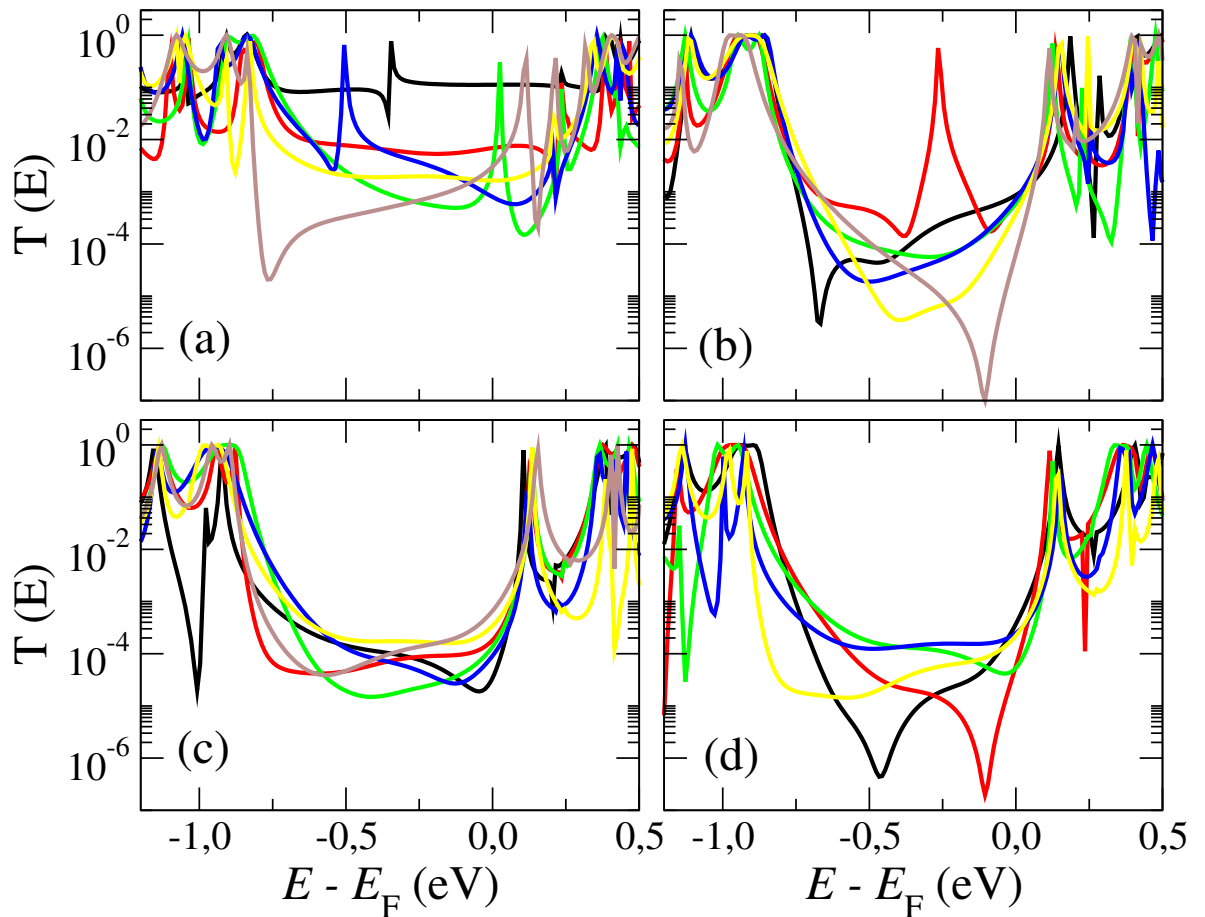


Figure 6.3: Evolution of the Γ -point transmission coefficient $T(E)$ with increasing gap length d , which varies between -11.8 \AA and 10.2 \AA relative to d_0 , in steps of 1.0 \AA . Panels (a)-(d) correspond to curves in the intervals $[-11.8 \text{ \AA}, -6.8 \text{ \AA}]$, $[-5.8 \text{ \AA}, -0.8 \text{ \AA}]$, $[0.2 \text{ \AA}, 5.2 \text{ \AA}]$ and $[6.2 \text{ \AA}, 10.2 \text{ \AA}]$, respectively. The colours of the lines in the order *black, red, green, blue, yellow, brown* correspond to increasing d .

molecular orbital (HOMO)/lowest unoccupied molecular orbital (LUMO) gap, it is expected that the Γ -point estimate of the low-voltage conductance $G = G_0 T(E_F)$ should show a wide spread. This is confirmed in figure 6.4 where G features strong oscillations as a function of the relative molecule/graphene position. Notice that these oscillations are not strictly periodic as a function of d (see figure 6.4(a)). In fact, they oscillations cease when the distance between the sheets are smaller than $d \sim -4.6\text{\AA}$. This is so, because tunneling between two sheet appears such distances. They are however periodic as a function of d_y , as shown figure 6.4(b), with the period of the graphene lattice along that direction ($\sim 4.26\text{\AA}$).

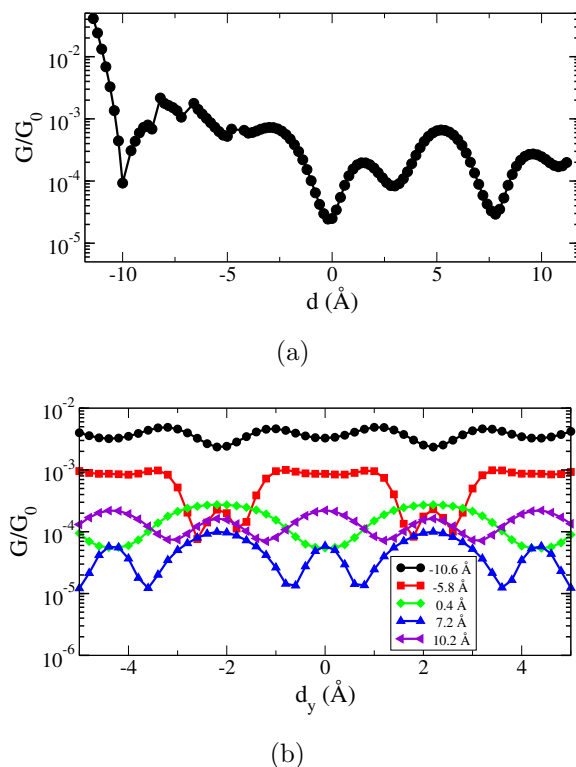


Figure 6.4: Low-voltage conductance G/G_0 as a function of changes in the junction. (a) G/G_0 as a function of the gap length d ; (b) G/G_0 as a function of the transverse coordinate d_y . G/G_0 is estimated as $T(E_F)$, using only the Γ -point in the k summation.

It has been devised a molecule long enough to bridge the physical electrode gap, and anchor deep inside the graphene sheets via the planar phthalocyanine groups. This length requirement puts stringent conditions on the conjugated nature of the trimer molecule, because the conductance of a molecule decreases exponentially with its length. Butadiyne chains are an excellent choice as linking groups because they enhance the molecule's conjugated nature leading to decay exponents close to zero [?]. Electrons, however, can be transferred between the graphene sheets via several paths. They may hope from the sheets to phthalocyanine units or

to the butadiyne molecules. The different paths lead to destructive interference effects and therefore to Fano-like resonances in $T(E)$. In order to check this assertion, the transmission of one test system has been performed. The system is shown in figure 6.5 and comprises two graphene sheets separated by a physical gap of $d \sim 9.6 \text{ \AA}$, which ensures that there is no tunneling between these sheets, a phthalocyanine monomer at vertical distance of $d_h \sim 3.5 \text{ \AA}$, and a third graphene sheet above the phthalocyanine unit separated by $d_h \sim 3.5 \text{ \AA}$ (which means that the distance between the bottom and the top graphene sheets is $d_{graph.} \sim 7.0 \text{ \AA}$). The graphene sheets have been devised as the previous case, which means that they are terminated in an armchair configuration passivated by hydrogen atoms in a 1-1-1 sequence. The same parameters to calculate the electronic structure as well as the transport properties have been used (means basis set, grid, etc.). Figure 6.5(b) shows the transmission coefficients when the above sheet is moved across the z-direction (parallel to transport) in steps of 0.2 \AA . It follows that, as before, the BW resonances are placed at the same energy position, namely, they are independent of the graphene movement. Notwithstanding, in this case the transmission between two BW resonances does not change too much. It is confirmed by plotting the conductance as a function of the displacement, which can be seen in figure 6.5(c). Notice that in this case, the conductance is in the same order of magnitude ($\sim 10^8 G_0$). Electrons can only be transferred between the graphene sheets via one path: through the phthalocyanine molecule.

Now, the impact of the k -points summation on $T(E)$ is going to be analyzed. Figure 6.6 shows the evolution of the $T(E)$ as the accuracy in the k -point summation is improved, for two given arrangements. Notice first that the energy position of the resonances remains the same, which supports the previous claim on the universality of the BW resonances. Second, the Fano-like dips (see for example in $d=7.2 \text{ \AA}$ at around -1.2 eV) are washed away. It is inferred that electron conduction through the new open channels does not suffer destructive interference effects. Third, clearly many resonances do disappear as more channels are added. However, the Fano-like resonance for $d = 7.2 \text{ \AA}$ near to the Fermi level does not disappear and remains almost unaffected even for a large number of k points. This indicates that only Fano-like resonances whose dip is very close to the Dirac point survive when the number of k points increases. Computing $T(E_F)$ and therefore the low-bias conductance is complicated by the fact that strictly speaking only the $k = 0$ channel exists asymptotically at E_F even for a large number of k points.

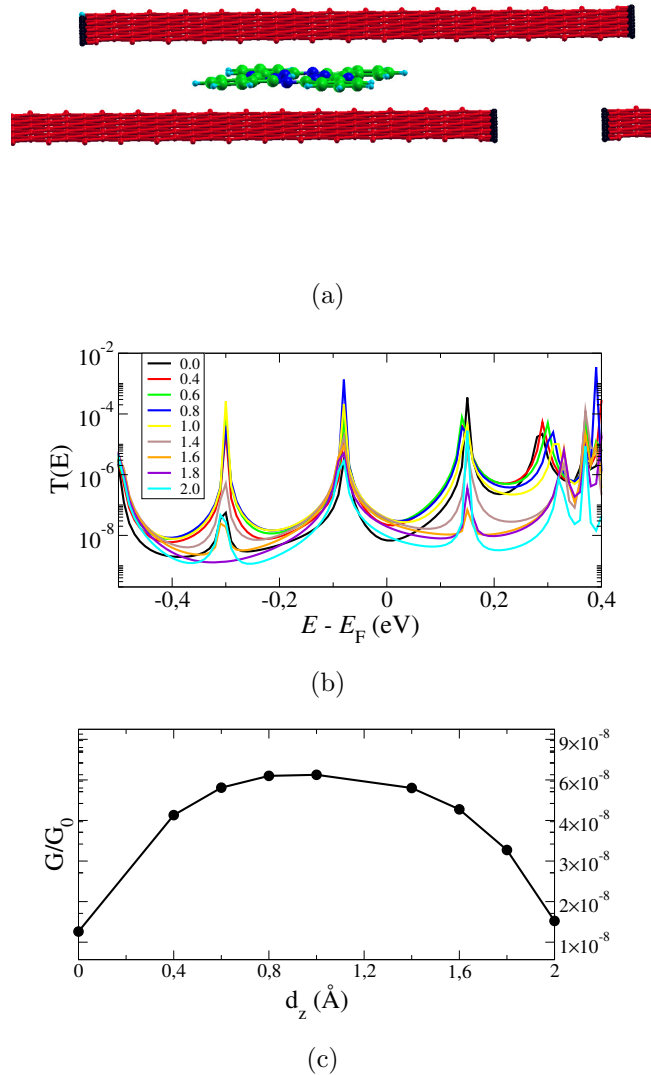


Figure 6.5: Plot of the test junction (a) where red, black, green, light-blue and blue represent carbon and hydrogen in graphene, and carbon, hydrogen and nitrogen in the molecule respectively; (b) Evolution of the Γ -point transmission coefficient $T(E)$ when the top graphene sheet is moved across z -direction in steps of 0.2 \AA and (c) Low-voltage conductance G/G_0 as a function of changes parallel coordinate d_z of the top graphene sheet.

6.4 Remarks

The main result is a remarkably universality in the energy position of the BW resonances. The energy position of such resonances appearing in the zero-bias transmission coefficient $T(E)$ does not shift when the molecules are displaced or when the graphene sheets are pulled away or pushed to vary the physical gap. However, it was found a large spread in the low-bias conductance $G = G_0 T(E_F)$ as a function of the molecules' and electrodes' relative position, which was at-

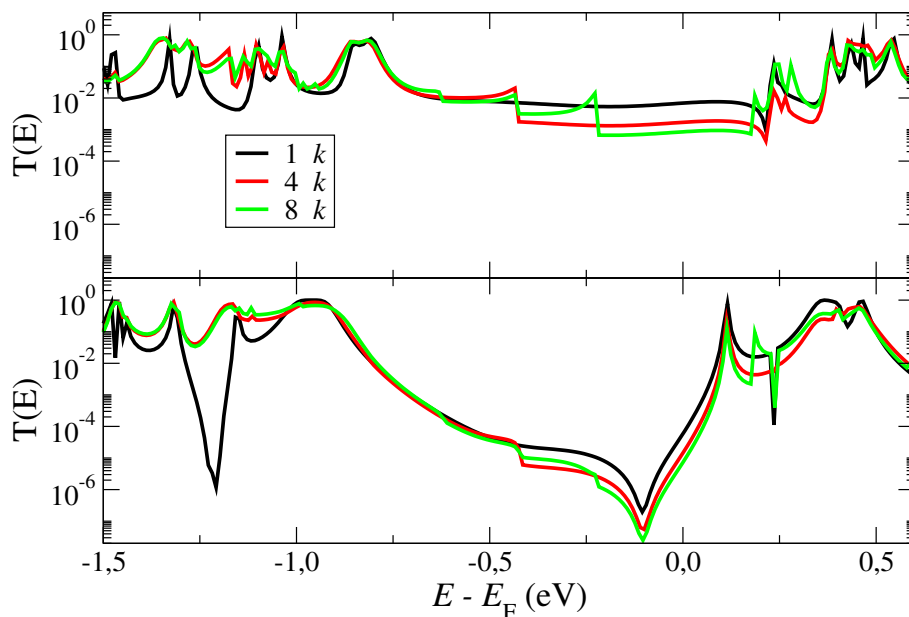


Figure 6.6: $T(E)$ for 1, 4 and 8 k -points for (a) $d = -10.8 \text{ \AA}$ and (b) $d = 7.2 \text{ \AA}$.

tributed to the energy shift of Fano-like resonances around Fermi level, driven by the molecule-graphene relative motion. This universality property is a consequence of the isochemical nature of the physisorbed species. It was used a van der Waals functional that is suited for the problem at hand. It was argued that even if the energy position of the molecular resonances is fully rearranged by strong correlations, the new spectra should follow the same universality behaviour. In this sense, it is suggested that the above property could be used to solve the conductance variability problem inherent to noble-metal based single-molecule junctions. This is so because the energy position of the transmission resonances may be suitable modified by the application of a gate voltage. The energy spectrum may also be tailored by synthetic chemistry methods. However, contrary to the case of noble-metal electrodes, a large number of k -points must be used to find accurate estimates of the low-voltage conductance, which renders theory predictions a delicate task.

It was found binding energies for molecule drift parallel to the physical gap of order 0.1-0.2 eV, which should be enough to provide mechanical stability to the junction at temperatures below 100 K. The desired room-temperature mechanical stability of this graphene junctions seems achievable by attaching side groups, or by increasing the surface area of the anchors. Furthermore, irregularities at the edges will act as anchoring points. Longer linker groups than those used in the present study could be synthesized to better avoid graphene's edges. It would be

relevant to design the linker groups so as to either tailor or avoid the Fano-like resonances.

Final Remarks

This thesis has addressed some of the most relevant issues in molecular electronics. These are the variability problem, the improvement of the molecular diode effect, the identification of new functionalities based on Quantum Interference (QI) phenomena and the search for new electrode materials that may improve the robustness of state-of-art single-molecule devices.

Chapter 3 shows an example of how QI effects can be identified, tuned and exploited in a single-molecule junction. The key element here is the emergence of a Fano resonance within the HOMO-LUMO gap. The resonance appears here because a 3d transition metal ion is inserted inside a planar organic molecule -a porphyrin-. It was shown how the resonance energy position can be shifted by swapping the ion across the 3d-row of the periodic table. It was found in particular how iron, cobal and copper spin-split the electronic transport giving rise spin-filtering behaviour.

Chapter 4 proposes a route to reduce variability that exploits the steric hindrance effect inherent to bulky anchor groups. As a result, the number of possible atomic arrangements at the electrode/molecule contact is drastically reduced. It was shown how this phase-space reduction leads to a lower number of conductance peaks, hence to a reduced conductance variability. This was part of a collaboration work done with the experimental group headed by Pilar Cea and Santiago Martín (Universidad de Zaragoza) and the experimentaal groupd headed by Si-

mon Higgins and Richard Nichols (University of Liverpool).

The diode effect became the paradigm of a molecular device functionality since its initial proposal by Aviram and Ratner. It is frustrating though that after so many years the best rectification ratios achieved have barely exceeded the tens. Chapter 5 picks a strategy proposed many years ago by Williams and co-workers, and shows how by exploiting carefully the molecular details, rectification ratios of order 200-400 can be achieved. This work is part of a collaboration with the experimental groups headed by Emanuel Loertscher (IBM) and Florian von Wrochem (SONY).

Chapter 6 describes an initial exploration on the use of graphene as an electrode. It was tried to identify whether graphene could alleviate the variability problem. To do so, It was used simple molecules with planar anchor groups, that seen best tailored to the 2d nature of graphene. It was found that the placement of the Breit-Wigner molecular resonance remains largely constant as molecules change position. However, It was also found that the transmission changes by orders of magnitude. This is possibly due to the appearance of Fano resonances due to multiple electron paths. It was concluded that these paths should be either eliminated or controlled, depending of the desired goal.

To sum up, the work done in this thesis clearly demonstrates that, even though the molecular electronics nowadays presents a series of problems, many strategies have been developed in recent years which show that it could be possible to reach a molecular nanotechnology.

Bibliography

- [1] M. Ratner and A. Aviram, *Chem. Phys. Lett.* **29**, 277 (1974)
- [2] R. S. Mulliken and C. A. Rieke, *Rep. Prog. Phys.* **8**, 231 (1941)
- [3] R. S. Mulliken, *Rev. Mod. Phys.* **14**, 265 (1942)
- [4] A. Szent-Gyorgyi, *Nature* **148**, 157 (1941)
- [5] D. D. Eley, *Nature* **162**, 819 (1948)
- [6] A. R. Von Hippel, *Molecular Science and Molecular Engineering*, (MIT Press, 1959)
- [7] G. Binning, H. Rohrer, Ch. Gerber and E. Weibel, *Phys. Rev. Lett.* **49**, 57 (1982)
- [8] G. Binning, C. F. Quate and Ch. Gerber, *Phys. Rev. Lett.* **56**, 930 (1986)
- [9] D. M. Eigler and E. K. Schweizer, *Nature* **344**, 524 (1990)
- [10] L. A. Bumm, J. J. Arnold, M. T. Cygan, T. D. Dunbar, T. P. Burgin, L. Jones II, D. L. Allara, J. M. Tour, P. S. Weiss *Science* **271**, 1705 (1996)
- [11] J. C. Cuevas and E. Scheer, *Molecular Electronics: An Introduction to Theory and Experiment*, (World Scientific Publishing Company, 2010)
- [12] M. Pomerantz, A. Aviram, R. A. McCorkle, L. Li and A. G. Schrott, *Science* **255**, 1115 (1992)
- [13] M. Dorogi, J. Gómez, R. Osifchin, R. P. Andres and R. Reifengerger, *Phys. Rev. B* **52**, 9071 (1995)

- [14] M. A. Reed, C. Zhou, C. J. Muller, T. P. Burgin and J. M. Tour, *Science* **278**, 252 (1997)
- [15] C. Kergueris, J. P. Bourgoin, S. Palacin, D. Esteve, C. Urbina, M. Magoga and C. Joachim, *Phys. Rev. B* **59**, 12505 (1999)
- [16] R. M. Metzger, B. Chen, U. Hopfner, M. V. Lakshmikantham, D. Vuillaume, T. Kawai, X. Wu, H. Tachibana, T. V. Hughes, H. Sakurai, J. W. Baldwin, C. Hosch, M. P. Cava, L. Brehmer and G. J. Ashwell, *J. Am. Chem. Soc.* **119**, 10455 (1997)
- [17] C. P. Collier, E. W. Wong, M. Belohradsky, F. M. Raymo, J. F. Stoddart, P. J. Kuekes, R. S. Williams and J. R. Heath, *Science* **285**, 391 (1999)
- [18] J. Chen, M. A. Reed, A. M. Rawlett and J. M. Tour, *Science* **286**, 1550 (1999)
- [19] C. Caroli, R. Combescot, P. Nozieres and D. Saint-James, *J. Phys. C: Solid St. Phys.* **4**, 916 (1971)
- [20] C. Caroli, R. Combescot, P. Nozieres and D. Saint-James, *J. Phys. C: Solid St. Phys.* **4**, 2598 (1971)
- [21] C. Caroli, R. Combescot, P. Nozieres and D. Saint-James, *J. Phys. C: Solid St. Phys.* **4**, 2611 (1971)
- [22] C. Caroli, R. Combescot, P. Nozieres and D. Saint-James, *J. Phys. C: Solid St. Phys.* **5**, 21 (1972)
- [23] Y. Meir and N. S. Wingreen, *Phys. Rev. Lett.* **68**, 2512 (1992)
- [24] N. S. Wingreen, A. P. Jauho and Y. Meir, *Phys. Rev. B* **48**, 8487 (1993)
- [25] A. P. Jauho, N. S. Wingreen and Y. Meir, *Phys. Rev. B* **50**, 5528 (1994)
- [26] R. Lake, G. Klimeck, R. Chris Bowen and D. Jovanovic, *J. Appl. Phys.* **81**, 7845 (1997)
- [27] M. Brandbyge, J. L. Mozos, P. Odejón, J. Taylor and K. Stokbro, *Phys. Rev. B* **65**, 165401 (2002)
- [28] A. R. Rocha, V. M. García-Suárez, S. Bailey, C. Lambert, J. Ferrer and S. Sanvito, *Phys. Rev. B* **73**, 085414 (2006)
- [29] A. Svizhenko, M. P. Anantram, T. R. Govindan, B. Biegel and R. Venugopal, *J. Appl. Phys.* **91**, 2343 (2002)

-
- [30] V. N. Do, P. Dolfus and V. L. Nguyen, *J. Appl. Phys.* **100**, 093705 (2006)
- [31] G. Rubio, N. Agraït and S. Vieira, *Phys. Rev. Lett.* **76**, 2302 (1996)
- [32] B. Xu, X. Xiao and N. J. Tao, *J. Am. Chem. Soc.* **125**, 16164 (2003)
- [33] S. V. Aradhya and L. Venkataraman, *Nature Nano.* **8**, 399 (2013)
- [34] N. Hauptmann, F. Mohn, L. Gross, G. Meyer, T. Frederiksen and R. Berndt
New J. Phys. **14**, 073032 (2012)
- [35] M. Frei, S. V. Aradhya, M. S. Hybertsen and L. Venkataraman, *J. Am. Chem. Soc.* **134**, 4003 (2012)
- [36] M. Frei, S. V. Aradhya, M. Koentopp, M. S. Hybertsen and L. Venkataraman, *Nano Lett.* **11**, 1518 (2011)
- [37] C. Wagner, N. Fournier, F. S. Tautz and R. Temirov, *Phys. Rev. Lett.* **109**, 076102 (2012)
- [38] D. R. Ward, N. J. Halas, J. W. Ciszek, J. M. Tour, Y. Wu, P. Nordlander and D. Natelson, *Nano Lett.* **8**, 919 (2008)
- [39] D. R. Ward, D. A. Corley, J. M. Tour and D. Natelson, *Nature Nano.* **6**, 3 (2011)
- [40] Z. Liu, S. Ding, Z. Chen, X. Wang, J. Tian, J. R. Anema, X. Zhou, D. Wu, B. Mao, X. Xu, B. Ren and Z. Tian, *Nature Commun.* **2**, 305 (2011)
- [41] S. Jan van der Molen and P. Liljeroth, *J. Phys. Cond. Matter* **22**, 133001 (2010)
- [42] S. Battacharyya, A. Kibel, G. Kodis, P. A. Liddell, M. Gervaldo, D. Gust and S. Lindsay, *Nano Lett.* **11**, 2709 (2011)
- [43] M. Paulsson and S. Datta, *Phys. Rev. B* **67**, 241403 (2003)
- [44] Y. Dubi and M. Di Ventra, *Rev. Mod. Phys.* **83**, 131 (2011)
- [45] B. Ludoph and J. M. van Ruitenbeek, *Phys. Rev. B* **59**, 12290 (1999)
- [46] P. Reddy, S. Yang, R. A. Segalman and A. Majumdar, *Science* **315**, 1568 (2007)
- [47] W. Liang, M. P. Shores, M. Bockrath, J. R. Long and H. Park, *Nature* **417**, 725 (2002)

- [48] J. Park, A. N. Pasupathy, J. I. Goldsmith, C. Chang, Y. Yaish, J. R. Petta, M. Rinkoski, J. P. Sethna, H. D. Abruña, P. L. McEuen and D. C. Ralph, *Nature* **417**, 722 (2002)
- [49] E. A. Osorio, K. M. Poulsen, H. S. J. van der Zant, J. Paaske, P. Hedegård, K. Flensberg, J. Bendix and T. Bjørnholm, *Nano Lett.* **10**, 105 (2010)
- [50] S. Schmaus, A. Bagrets, Y. Nahas, T. K. Yamada, A. Bork, B. Bowen, E. Beaurepaire, F. Evers and W. Wulfhekel, *Nature Nano.* **6**, 185 (2011)
- [51] C. Iacovita, M. V. Rastei, B. W. Heinrich, T. Brumme, J. Kortus, L. Limot and J. P. Bucher, *Phys. Rev. Lett.* **101**, 116602 (2008)
- [52] R. Vincent, S. Klyatskaya, M. Ruben, W. Wernsdorfer and F. Balestro, *Nature* **488**, 357 (2012)
- [53] G. C. Solomon, C. Herrmann, T. Hansen, V. Mujica and M. Ratner, *Nature Chem.* **2**, 223 (2010)
- [54] D. M. Cardamone, C. A. Stafford and S. Mazumdar, *Nano Lett.* **6**, 2422 (2006)
- [55] S. Ke, W. Yang and H. U. Baranger, *Nano Lett.* **8**, 3257 (2008)
- [56] T. Markussen, R. Stadler and S. Thygesen, *Nano Lett.* **10**, 4260 (2010)
- [57] R. Stadler, M. Forshaw and C. Joachim, *Nanotechnology* **14**, 138 (2003)
- [58] C. R. Arroyo, R. Frisenda, K. M. Poulsen, J. S. Seldenthuis, T. Bjørnholm and H. S. J. van der Zant *Nano. Res. Lett.* **8**, 234 (2013)
- [59] M. Strange, I. S. kristensen, K. S. Thygesen and K. W. Jacobsen *J. Chem. Phys.* **128**, 114714 (2008)
- [60] A. H. Castro-Neto, F. Guinea, N. M. R. Peres, K. S. Novoselov and A. K. Geim *Rev. Mod. Phys.* **81**, 109 (2009)
- [61] A. Candini, S. Klyatskaya, M. Ruben, W. Wernsdorfer and M. Affronte, *Nano Lett.* **11**, 2634 (2011)
- [62] K. K. Saha, B. K. Nikolić, V. Meunier, W. Lu and J. Bernholc, *Phys. Rev. Lett.* **105**, 236803 (2010)
- [63] S. Petersen, M. Glyvradal, P. Bøggild, W. Hu, R. Feidenhans'l and B. W. Laursen, *ACS Nano* **6**, 8022 (2012)

-
- [64] G. Wang, Y. Kim, M. Choe, T. W. Kim and T. Lee *Adv. Materials* **23**, 755 (2011)
- [65] R. M. Martin, *Electronic Structure: Basic theory and Practical Methods*, (Cambridge University Press,2004)
- [66] M. Born and J. R. Oppenheimer, *Ann. Phys.*, **84**, 457 (1927)
- [67] V. Fock, *Z. Phys.*, **61**, 126 (1930); **62**, 795 (1930)
- [68] J. A. Pople, *Rev. Mod. Phys.*, **71**, 1267 (1999)
- [69] P. Hohenberg and W. Kohn, *Phys. Rev.*, **136**, B864 (1964)
- [70] W. Kohn and L. J. Sham, *Phys. Rev.*, **140**, A1133 (1965)
- [71] C. Fiolhais, F. Nogueira and M. Marques *A Primer in Density Functional Theory*, (Springer,2000)
- [72] D. M. Ceperley and B. J. Alder, *Phys. Rev. Lett.*, **45**, 566 (1980)
- [73] J. P. Perdew and A. Zunger, *Phys. Rev. B*, **23**, 5048 (1981)
- [74] A. D. Becke, *J. Chem. Phys.*, **98**, 1372 (1993)
- [75] J. P. Perdew and K. Schmidt, *Density Functional Theory and Its Applications to Materials*, (AIP Press, Melville, New York, 2001)
- [76] V. I. Anisimov, J. Zaanen and O. K. Andersen, *Phys. Rev. B*, **44**, 943 (1991)
- [77] V. I. Anisimov, F. Aryasetiawan and A. I. Lichtenstein, *J. Phys. Cond. Matter*, **9**, 767 (1997)
- [78] I. V. Solovyev, P. H. Dederichs and V. I. Anisimov, *Phys. Rev. B* **50**, 16861 (1994)
- [79] S. L. Dudarev, G. A. Botton, S. Y. Savrasov, C. J. Humphreys and A. P. Sutton, *Phys. Rev. B*, **57**, 1505 (1998)
- [80] C. Tablero, *J. Phys. Cond. Matter*, **20**, 325205 (2008)
- [81] J. M. Soler, E. Artacho, J. D. Gale, A. García, J. Junquera, P. Ordejón and D. Sánchez-Portal, *J. Phys. Cond. Matter* **14**, 2745 (2002)
- [82] N. Troullier and J. L. Martin, *Phys. Rev. B* **43**, 1993 (1991)
- [83] L. Kleinman and D. M. Bylander, *Phys. Rev. Lett.* **48**, 1425 (1982)
-

- [84] L. Kleinman, *Phys. Rev. B* **21**, 2630 (1980)
- [85] G. B. Bachelet and M. Schlüter, *Phys. Rev. B* **25**, 2103 (1982)
- [86] S. G. Louie, S. Froyen and M. L. Cohen, *Phys. Rev. B* **26**, 1738 (1982)
- [87] O. F. Sankei and D. J. Niklewski, *Phys. Rev. B* **40**, 3979 (1989)
- [88] D. Sánchez-Portal, J. M. Soler and E. Artacho, *J. Phys. Cond. Matter* **8**, 3859 (1996)
- [89] E. Anglada, J. M. Soler, J. Junquera and E. Artacho, *Phys. Rev. B* **66**, 205101 (2002)
- [90] S. Huzinaga *et al Gaussian Basis Sets for Molecular Calculations*, (Elsevier, 1984)
- [91] E. Artacho, D. Sánchez-Portal, P. Ordejón, A. García and J. M. Soler, *Phys. Status Solidi B* **215**, 809 (1999)
- [92] S. Datta, *Electronic Transport in Mesoscopic Systems*, (Cambridge University Press, 1995)
- [93] M. Büttiker, Y. Imry, R. Landauer and S. Pinhas, *Phys. Rev. B* **31**, 6207 (1985)
- [94] D. Wotmann, *AbInitio Description of Electronic Transport*, (Computational Nanoscience, John von Neumann Institute for Computing, Jülich, 2006)
- [95] J. Ferrer, C. J. Lambert, V. M. García-Suárez, D. Zs. Manrique, D. Visontai, L. Oroszlany, R. Ferradás, I. Grace, S. W. D. Bailey, K. Guillemot, H. Sadeghi and L. A. Algharagholy, *New J. Phys.* **16**, 093029 (2014)
- [96] V. M. Garccía-Suárez and J. Ferrer, *Phys. Rev. B* **86**, 125446 (2012)
- [97] V. V. Maslyuk, S. Achilles and I. Merting, *Solid State Commun.* **150**, 505 (2010)
- [98] C. Rovira, K. Kunc, J. Hutter, P. Ballone and M. Parrinello, *J. Phys. Chem. A* **101**, 8914 (1997)
- [99] J. B. Neaton, M. S. Hybertsen and S. G. Louie, *Phys. Rev. Lett.* **97**, 216405 (2006)
- [100] D. J. Mowbray, G. Jones and K. S. Thygesen, *J. Chem. Phys.* **128**, 111103 (2008)

-
- [101] A. Cehovin, H. Mera, J. H. Jensen, K. Stokbro and T. B. Pedersen, *Phys. Rev. B* **77**, 195432 (2008)
- [102] V. M. García-Suárez and C. J. Lambert *New J. Phys.* **13**, 053026 (2011)
- [103] A. R. Rocha, V. M. García-Suárez, S. W. Bailey, C. J. Lambert, J. Ferrer and S. Sanvito, *Nature Materials* **4**, 335 (2005)
- [104] A. R. Rocha, V. M. García-Suárez, S. W. Bailey, C. J. Lambert, J. Ferrer and S. Sanvito, *Phys. Rev. B* **73**, 085414 (2006)
- [105] J. Ferrer, A. Martín-Rodero and F. Flores, *Phys. Rev. B* **38**, R10113 (1988)
- [106] L. P. Kadanoff and G. Baym, *Quantum Statistical Mechanics*, (Benjamin, Menlo Park, CA, 1962)
- [107] L. V. Keldysh, *Sov. Phys. JETP* **20**, 1018 (1965)
- [108] R. E. Sparks, V. M. García-Suárez, D. Zs. Manrique and C. J. Lambert, *Phys. Rev. B* **83**, 075437 (2011)
- [109] C. M. Cuédon, H. Valkenier, T. Markussen, K. S. Thygesen, J. C. Hummelen and S. Jan van der Molen, *Nature Nano.* **7**, 305 (2012)
- [110] N. Wang, H. Liu, J. Zhao, Y. Cui, Z. Xu, Y. Ye, M. Kiguchi and K. Murakoshi, *J. Phys. Chem. C* **113**, 7416 (2009)
- [111] D. L. Drabkin, *The Porphyrins (Selected Landmarks in the History of Porphyrins and Their Biologically Functional Derivatives)*, vol. 1 (ed. D. Dolphin, New York: Academic 1978)
- [112] D. Dorough, J. R. Miller and F. M. Huennekens, *J. Am. Chem. Soc.* **73**, 4315 (1951)
- [113] D. Gust and J. D. Roberts, *J. Am. Chem. Soc.* **99**, 3637 (1977)
- [114] H. Goff, G. N. La Mar and C. A. Reed, *J. Am. Chem. Soc.* **99**, 3641 (1977)
- [115] F. D'Souza, P. Boulas, A. M. Aukauloo, R. Guillard, M. Kisters. E. Vogel and K. M. Kadish, *J. Phys. Chem.* **98**, 11885 (1994)
- [116] M. S. Liao and S. Scheiner, *J. Chem. Phys.* **117**, 205 (2002)
- [117] M. Palummo, C. Hogan, F. Sottile, P. Bagalá and A. Rubio, *J. Chem. Phys.* **131**, 084102 (2009)

- [118] J. Otsuki, *Coord. Chem. Rev.* **254**, 2311 (2010)
- [119] G. Sedghi, V. M. Garcıa-Suarez, L. J. Esdaile, H. L. Anderson, C. J. Lambert, S. Martın, D. Bethell, S. J. Higgins, M. Elliot, N. Bennett, J. M. Macdonald and R. J. Nichols, *Nature Nano.* **6**, 517 (2011)
- [120] I. Beletskaya, V.S. Tyurin, A. Y. Tsivadze, R. Guilard and C. Stern, *Chem. Rev.* **109**, 1659 (2009)
- [121] W. Jentzen, I. Turowska-Tyrk, W. R. Scheidt and J. A. Shelnutt, *Inorg. Chem.* **35**, 3559 (1996)
- [122] M. P. Suh, P. N. Swepston and J. A. Ibers, *J. Am. Chem. Soc.* **106**, 5164 (1984)
- [123] J. P. Perdew, K. Burke and M. Ernzerhof, *Phys. Rev. Lett.* **77**, 3865 (1996)
- [124] N. Troullier and J. L. Martins, *Phys. Rev. B* **43**, 1993 (1991)
- [125] L. Kleinman and D. M. Bylander, *Phys. Rev. Lett.* **48**, 1425 (1982)
- [126] F. Parmigiani and L. Sangaletti, *Journal of Electron Spectroscopy and Related Phenomena* **98**, 287 (1999)
- [127] M. Cococcioni and S. Gironcoli, *Phys. Rev. B* **71**, 035105 (2005)
- [128] P. M. Panchmatia, B. Snayal and P. M. Oppeneer, *Chem. Phys.* **343**, 47 (2008)
- [129] S. Martın, D. Zs. Manrique, V. M. Garcıa-Suarez, W. Haiss, S. J. Higgins, C. J. Lambert and R. J. Nichols, *Nanotechnology* **20**, 125203 (2009)
- [130] V. M. Garcıa-Suarez and J. Ferrer, *Phys. Rev. B* **86**, 125446 (2012)
- [131] G. Fagas, A. G. Kozorezov, C. J. Lambert, J. K. Wigmore, A. Peacock, A. Poelaert and R. den Hartog, *Phys. Rev. B* **60**, 6459 (1999)
- [132] A. Kambili, G. Fagas, V. I. Fal'ko, and C. J. Lambert, *Phys. Rev. B* **60**, 15593 (1999)
- [133] Y. Dubi and M. Di Ventra, *Rev. Mod. Phys.* **83**, 131 (2011)
- [134] C. Li, I. Pobelov, T. Wandlowski, A. Bagrets, A. Arnold and F. Evers, *J. Am. Chem. Soc.* **130**, 318 (2008)
- [135] W. Haiss, S. Martın, E. Leary, H. van Zalinge, S. J. Higgins, L. Bouffier and R. J. Nichols, *J. Phys. Chem. C* **113**, 5823 (2009)

-
- [136] M. Kamenetska, S. Y. Quek, A. C. Whalley, M. L. Steigerwald, H. J. Choi, S. G. Louie, C. Nuckolls, M. S. Hybertsen, J. B. Neaton and L. Venkataraman, *J. Am. Chem. Soc.* **132**, 6817 (2010)
- [137] S. Y. Quek, M. Kamenetska, M. L. Steigerwald, H. J. Choi, S. G. Louie, M. S. Hybertsen, J. B. Neaton and L. Venkataraman, *Nature Nano.* **4**, 230 (2009)
- [138] A. Marchenko, N. Katsonis, D. Fichou, C. Aubert and M. Malacria, *J. Am. Chem. Soc.* **124**, 9998 (2009)
- [139] S. Marqués-González, D. S. Yufit, J. A. K. Howard, S. Martín, H. M. Osorio, V. M. García-Suárez, R. J. Nichols, S. J. Higgins, P. Cea and P. J. Low, *Dalton Transactions* **42**, 338 (2013)
- [140] R. Ferradás, S. Marqués-González, H. M. Osorio, J. Ferrer, P. Cea, S. J. Higgins, R. J. Nichols, P. J. Low, V. M. García-Suárez and S. Martín, *J. Am. Chem. Soc.* **?**, **?** (2015)
- [141] B. Q. Xu and N. J. J. Tao, *Science* **301**, 1221 (2003)
- [142] W. Haiss, H. van Zalinge, S. J. Higgins, D. Bethell, H. Höbenreich, D. J. Schiffrin and R. J. Nichols, *J. Am. Chem. Soc.* **125**, 15294 (2003)
- [143] E. G. Petrov, A. Marchenko, O. L. Kapitanchuk, N. Katsonis and D. Fichou, *Mol. Cryst. Liq. Cryst.* **589**, 3 (2014)
- [144] D. W. Stephan, *Org. Biomol. Chem.* **6**, 1535 (2008)
- [145] J. Pan, Z. Zhang, K. Ding, X. Deng and C. Guo, *Appl. Phys. Lett.* **98**, 092102 (2011)
- [146] G. M. Morales, P. Jiang, S. Yuan, Y. Lee, A. Sánchez, W. You and L. Yu, *J. Am. Chem. Soc.* **127**, 10456 (2005)
- [147] S. K. Yee, J. Sun, P. Darancet, T. D. Tilley, A. Majumdar, J. B. Neaton and R. A. Segalman, *ACS Nano* **5**, 9256 (2011)
- [148] R. M. Metzger, *Accounts of Chemical Research* **32**, 950 (1999)
- [149] S. Yuan, S. Wang, Q. Mei, Q. Ling, L. Wang and W. Huang, *J. Phys. Chem. A* **115**, 9033 (2011)
- [150] J. C. Ellenbongen and J. C. Love, *Proc. IEEE* **88**, 386 (2000)
-

- [151] C. Krzeminski, C. Delerue, G. Allan, D. Vuillaume and R. M. Metzger, *Phys. Rev. B* **64**, 085405 (2001)
- [152] P. E. Kornilovitch, A. M. Bratkovsky and R. Stanley Williams, *Phys. Rev. B* **66**, 165436 (2002)
- [153] F. Zahid, A. W. Ghosh, M. Paulsson, E. Polizzi and S. Datta *Phys. Rev. B* **70**, 245317 (2004)
- [154] B. Capozzi, J. Xia, O. Adak, E. J. Dell, Z. F. Liu, J. C. Taylor, J. B. Neaton, L. M. Campos and L. Venkataraman, *Nature Nano.* **10**, 522 (2015)
- [155] B. Larade and A. M. Bratkovsky, *Phys. Rev. B* **68**, 235305 (2003)
- [156] M. Kamenetska, M. Koentopp, A. C. Whalley, Y. S. Park, M. L. Steigerwald, C. Nuckolls, M. S. Hybertsen and L. Venkataraman, *Phys. Rev. Lett.* **102**, 126803 (2009)
- [157] Z. L. Cheng, R. Skouta, H. Vázquez, J. R. Widawaky, S. Schneebeili, W. Chen, M. S. Hybertsen, R. Breslow and L. Venkataraman, *Nature Nano.* **6**, 353 (2011)
- [158] L. Venkataraman, J. E. Klare, I. W. Tam, C. Nuckolls, M. S. Hybertsen and M. L. Steigerwald, *Nano. Lett.* **6**, 458 (2006)
- [159] F. Prins, A. Barreiro, J. W. Ruitenber, J. S. Seldenthuis, N. Aliaga-Alcalde, L. M. K. Vandersypen and H. S. J. van der Zant, *Nano. Lett.* **11**, 4607 (2011)
- [160] M. Koleini, M. Paulsson and M. Brandbyge, *Phys. Rev. Lett.* **98**, 197202 (2007)
- [161] H. Cheraghchi and K. Esfarjani, *Phys. Rev. B* **78**, 085123 (2008)
- [162] K. K. Saha, T. Markussen, K. S. Thygesen and B. K. Nikolić, *Phys. Rev. B* **84**, 041412(R) (2011)
- [163] A. Bergvall, K. Berland, P. Hyldgaard, S. Kubatkin and T. Löfwander, *Phys. Rev. B* **84**, 155451 (2011)
- [164] C. G. Péterfalvi and C. J. Lambert, *Phys. Rev. B* **86**, 085443 (2012)